

**HIGH PERFORMANCE MULTIVARIABLE CONTROL OF THE
"SUPERMANEUVERABLE " F18/HARV FIGHTER AIRCRAFT**

BY

PETROS VOULGARIS

Diploma in Mechanical Engineering, National Technical University of Athens

(1986)

Submitted to

the Department of Aeronautics and Astronautics

in Partial Fulfilment of the Requirements for

the Degree of

MASTER OF SCIENCE

IN AERONAUTICS AND ASTRONAUTICS

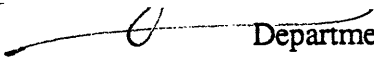
at the

MASSACHUSETTS INSTITUTE OF TECHNOLOGY


May, 1988

© Massachusetts Institute of Technology, 1988

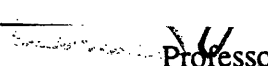
Signature of Author _____


Department of Aeronautics and Astronautics
May, 1988

Certified by _____


Professor Lena Valavani
Thesis Supervisor

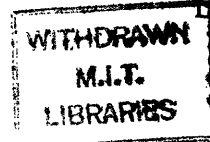
Accepted by _____


Professor Harold Y. Wachman, Chairman
Departmental Graduate Committee

Aero
MASSACHUSETTS INSTITUTE
OF TECHNOLOGY

JUN 01 1988

LIBRARIES



**HIGH PERFORMANCE MULTIVARIABLE CONTROL OF THE
"SUPERMANEUVERABLE" F18/HARV FIGHTER AIRCRAFT**

by

PETROS VOULGARIS

Submitted to the Department of Aeronautics and Astronautics
on May 6, 1988 in partial fulfillment of the requirements for the degree of
Master of Science in Aeronautics and Astronautics

ABSTRACT

Current efforts by NASA Langley have focussed on expanding the flight envelope of the F/A-18 aircraft. Of particular concern has been the low speed - high angle of attack regime over which the conventional aerodynamic controls of the F/A-18 lose their effectiveness.

In order to address this problem the F18/HARV was developed. The F18/HARV is essentially a modified F/A-18 which possesses thrust vectoring capabilities and hence increases maneuverability in this above flight regime.

In this thesis the LQG/LTR and H_{∞} design methodologies will be used to design high performance MIMO controllers for the F18/HARV at operating points within the expanded envelope. In addition, the thesis shows how the control redundancy of the F18/HARV can be used to maintain nominal performance, as well as nominal stability, in situations where failures occur.

Thesis Supervisor : Lena Valavani
Title : Boeing Associate Professor

ACKNOWLEDGEMENTS

First and foremost, I would like to express my deepest appreciation to Professor Lena Valavani. Her infinite support, and steadfast guidance have been very much appreciated. I feel extremely fortunate to have had her as my thesis supervisor.

Secondly, I would like to thank Professor Michael Athans for providing me with the model used in this thesis and for providing guidance through his lectures.

This acknowledgements would be far from complete without thanking my colleagues at M.I.T. Specifically, I would like to thank Alex Gioulekas, Dr. Petros Kapsouris, Ioannis Kyrtzoglou, Dragan Obradovic, Tony Rodriguez, Brett Ridgely, Dr. Jeff Shamma.

I would like to thank Fifi Monseratte for helping me type this document. Her patience was very much appreciated.

Finally, I would like to thank the members of my family for their encouragement and the strong support they gave me.

This research was supported by the AFOSR- Eglin A.F.B. under grant F08635-87- K-0031, by the NASA Ames and Langley Research Centers under grant NASA/NAG -2-297 and by a gift from the Boeing Corporation.

TABLE OF CONTENTS

	page
ABSTRACT	i
ACKNOWLEDGEMENTS	ii
TABLE OF CONTENTS	iii
LIST OF FIGURES	vi
LIST OF TABLES	xi
CHAPTER 1: INTRODUCTION AND SUMMARY	
1.1 Motivation	1
1.2 Contribution of Thesis	2
1.3 Outline of Thesis	3
CHAPTER 2: SYSTEM DESCRIPTION AND MODEL FORMULATION	
2.1 Introduction	4
2.2 Description of the F18/HARV Aircraft	4
2.3 The F18/HARV Model	11
2.3.1 Introduction	11
2.3.2 Development of Linear Models	11
2.4 Summary	20
CHAPTER 3: ANALYSIS OF LINEAR MODELS	

3.1 Introduction	21
3.2 Natural Modes of the F18/HARV	21
3.3 Selection of Outputs to be Controlled	23
3.4 Scaling of Linear Model	24
3.5 Control Redundancy of the F18/HARV	28
3.5.1 Introduction	28
3.5.2 Procedure for Selection of Pseudocontrols	29
3.6 Frequency Domain Characteristics of the Pseudosystem	34
3.7 Summary	37

CHAPTER 4: COMPENSATOR DESIGN

4.1 Introduction	38
4.2 Design Specifications	38
4.3 Design of the LQG/LTR Compensator	44
4.3.1 Introduction	44
4.3.2 Summary of the LQG/LTR Methodology	45
4.3.3 Application of the LQG/LTR Design Methodology to the F18/HARV	49
4.3.3.1 Dynamic Augmentation and the Target Loop Design	49
4.3.3.2 Resulting Feedback Loop Design	56
4.3.3.3 Time Domain Simulations	60
4.3.3.4 Design Tradeoffs	67
4.3.3.5 Operating Points 2 and 3	72
4.4 Design of the H_{∞} Compensator	76
4.4.1 Introduction	76

4.4.2 Highlights of the H_{∞} Methodology	76
4.4.3 Application of the H_{∞} Design Methodology to the F18/HARV	83
4.4.3.1 Selection of Weights	83
4.4.3.2 Resulting Feedback Loop Design	87
4.4.3.3 Time Domain Simulations and Design Tradeoffs	90
4.5 Comparison of the LQG/LTR Compensator Designs	95
4.6 Summary	96
CHAPTER 5: HANDLING OF FAILURES	
5.1 Introduction	98
5.2 Pseudocontrol Distribution in the Presence of Failures	98
5.3 Time Simulations	100
5.4 Summary	105
CHAPTER 6: SUMMARY AND DIRECTIONS FOR FUTURE RESEARCH	
6.1 Summary	106
6.2 Directions for Further Research	107
APPENDIX A1	108
APPENDIX A2	112
REFERENCES	119

LIST OF FIGURES

CHAPTER 2

- Figure 2.1 : The F/A-18 Navy "Hornet" aircraft
- Figure 2.2 : Aerodynamic control surfaces
- Figure 2.3 : F18/HARV thrust vectoring vane system
- Figure 2.4 : Thrust vectoring control moments
- Figure 2.5 : F/A-18 flight control configuration
- Figure 2.6 : Longitudinal precision control modes

CHAPTER 3

- Figure 3.1 : Longitudinal natural modes
- Figure 3.2 : Pseudosystem
- Figure 3.3 : Singular values of pseudosystem at point 1
- Figure 3.4 : Singular values of pseudosystem at point 2
- Figure 3.5 : Singular values of pseudosystem at point 3

CHAPTER 4

- Figure 4.1 : Control system configuration for the actual system $G_O(s)$
- Figure 4.2 : Control system configuration for pseudosystem
- Figure 4.3 : Perturbed system
- Figure 4.4 : LQG/LTR compensator with the model of the system in a closed loop configuration
- Figure 4.5 : Target feedback loop
- Figure 4.6 : Augmentation with integrators

Figure 4.7 : Singular values of the augmented system $G_a(s)=I/sG_v(s)$

Figure 4.8 : Singular values of the shaping transfer function $C_a(sI-A_a)^{-1}L$

Figure 4.9 : Singular values of the target loop $G_T(s)$

Figure 4.10 : Singular values of the target loop sensitivity $(I+G_T(s))^{-1}$

Figure 4.11 : Singular values of the loop $G_a(s)K_{LQG/LTR}(s)$

Figure 4.12 : Singular values of the sensitivity $(I+G_a(s)K_{LQG/LTR}(s))^{-1}$

Figure 4.13 : Singular values of $K_{LQG/LTR}(s)$

Figure 4.14 : Singular values of $K_v(s)S(s)$

Figure 4.15 : Output response to r_1

Figure 4.16 : Output response to r_2

Figure 4.17 : Output response to r_3

Figure 4.18 : Output response to r_4

Figure 4.19 : Pseudocontrol response to r_1

Figure 4.20 : Pseudocontrol response to r_2

Figure 4.21 : Pseudocontrol response to r_3

Figure 4.22 : Pseudocontrol response to r_4

Figure 4.23.: Control response to r_1

Figure 4.24 : Control response to r_2

Figure 4.25 : Control response to r_3

Figure 4.26 : Control response to r_4

Figure 4.27 : Control system with prefilter in the reference command channel

Figure 4.28 : Singular values of the target loop tfm

Figure 4.29 : Singular values of the loop tfm

Figure 4.30 : Singular values of the sensitivity tfm

Figure 4.31 : Singular values of the LQG/LTR compensator

Figure 4.32 : Singular values of the r to v tfm

Figure 4.33 : Outputs response to r_1

Figure 4.34 : Control response to r_1

Figure 4.35 : Singular values of the loop tfm at point 2

Figure 4.36 : Singular values of the sensitivity tfm at point 2

Figure 4.37 : Singular values of the loop tfm at point 3

Figure 4.38 : Singular values of the sensitivity tfm at point 3

Figure 4.39 : Output response to r_1 at point 2

Figure 4.40 : Control response to r_1 at point 2

Figure 4.41 : Output response to r_2 at point 2

Figure 4.42 : Control response to r_2 at point 2

Figure 4.43 : Output response to r_1 at point 3

Figure 4.44 : Control response to r_1 at point 3

Figure 4.45 : Output response to r_2 at point 3

Figure 4.46 : Output response to r_2 at point 3

Figure 4.47 : General framework

Figure 4.48 : Standard feedback loop transformed to the general framework

Figure 4.49 : The H_∞ compensator structure

Figure 4.50 : Framework for the H_∞ compensator design for the pseudosystem

Figure 4.51 : Singular values of the weighting $W_S(s)$

Figure 4.52 : Singular values of the weighting $W_{KS}(s)$

Figure 4.53 : Singular values of the loop $G_V(s)K_V(s)$

Figure 4.54 : Singular values of the sensitivity $(I+G_V(s)K_V(s))^{-1}$

Figure 4.55 : Singular values of the compensator $K_V(s)$

Figure 4.56 : Singular values of the $K_V(s)(I+G_V(s)K_V(s))^{-1}$

Figure 4.57 : Output response to r_1

Figure 4.58 : Output response to r_2

Figure 4.59 : Output response to r_3

Figure 4.60 : Output response to r_4

Figure 4.61 : Control response to r_1

Figure 4.62 : Control response to r_2

Figure 4.63 : Control response to r_3

Figure 4.64 : Control response to r_4

Figure 4.65 : Singular values of the loop tfm

Figure 4.66 : Singular values of the sensitivity tfm

Figure 4.67 : Output response to r_1

Figure 4.68 : Control response to r_1

CHAPTER 5

Figure 5.1 : Control response to r_1 in case (i)

Figure 5.2 : Control response to r_1 in case (ii)

Figure 5.3 : Control response to r_1 in case (iii)

Figure 5.4 : Control response to r_1 in case (iv)

Figure 5.5 : Control response to r_1 in case (v)

Figure 5.6 : Control response to r_2 in case (i)

Figure 5.7 : Control response to r_2 in case (ii)

Figure 5.8 : Control response to r_2 in case (iii)

Figure 5.9 : Control response to r_2 in case (iv)

Figure 5.10 : Control response to r_2 in case (v)

LIST OF TABLES

CHAPTER 2

Table 2.1: Definitions ,Notation and Units

Table 2.2: Selected Operating Points

CHAPTER 3

Table 3.1: Open Loop poles at operatingpoints 1,2,and 3

Table 3.2: Saturation Limits

Table 3.3: Scaling Factors

CHAPTER 4

Table 4.1: Poles and zeros of the target loop $G_T(s)$ and target closed loop $C_T(s)$

Table 4.2: Poles and zeros of the augmented system, LQG/LTR compensator and closed loop system

Table 4.3: Scaled Rate Limits for Operating Point 1

Table 4.4: Poles and zeros of the compensator $K_v(s)$ and closed loop system $C(s)$

CHAPTER 1 INTRODUCTION AND SUMMARY

1. Motivation

During the past few years research efforts at NASA Langley have been directed toward enhancing the agility of military aircraft over an expanded flight envelope. This expanded envelope includes the low speed-high angle of attack regime over which dynamic pressure is low and conventional aerodynamic controls lose their effectiveness.

Current efforts have focussed on a modified version of the navy's F/A-18 fighter aircraft referred to as the "super maneuverable" F18/HARV (high alpha research vehicle). This vehicle is referred to as "supermaneuverable" because, in addition to possessing the conventional aerodynamic controls of the F/A-18, it possesses thrust vectoring vanes which allow moments to be generated effectively even under low speed-high angle of attack combat scenarios.

As discussed above the F18/HARV possesses many control inputs which can be used to maneuver the aircraft. The coordination of these controls in time, in order to achieve prescribed maneuvers, as expected, is a challenging highly multivariable control problem. It becomes especially challenging at very low speed-high angle of attack operating points where the aircraft becomes unstable. Because of this, controlling the vehicle over the expanded envelope is a nontrivial task.

In addressing the above highly multivariable control problem single-input single-output (SISO) classical ideas become difficult, if not impossible, to use. Consequently, direct

multivariable procedures are more suitable.

The LQG/LTR methodology as developed by Athans [1, 2], Doyle and Stein [7], has proven itself as an extensively used tool for control engineers developing multivariable controllers. The H_∞ design methodology, especially after recent results by Glover and Doyle [12], has also demonstrated great potential as a multivariable design tool. However, unlike the LQG/LTR design methodology not many mult examples of H_∞ designs have appeared in the literature.

Consequently, this thesis will use the LQG/LTR and H_∞ design methodologies to design high performance multi-input multi-output (MIMO) controllers for the F18/HARV at operating points within the expanded flight envelope. In addition, the thesis looks at how the control redundancy of the F18/HARV can be used to maintain nominal performance, as well as nominal stability, in situations where failures occur.

1.2 Contribution of Thesis

One major contribution of the thesis is that it provides a systematic procedure for designing controllers for dynamical systems with redundancy in the controls. The fact that no inputs are eliminated a priori to make the system square, provides a great amount of flexibility in situations that actuator failures or damages are present. In particular, the thesis shows how performance can be maintained even in the presence of control failures.

Another contribution of the thesis is that it provides a "realistic" design example to which the H_∞ and LQG/LTR methodologies are applied and compared.

Finally, this thesis points out fundamental tradeoffs when saturation magnitude and especially rate limits are posed.

1.3 Outline of Thesis

Chapter 2 describes the F18/HARV and discusses some modeling and longitudinal maneuvering issues.

Chapter 3 analyzes the linear models and issues as output selection and scaling are discussed. Also, a systematic way of generating pseudocontrols, taking full advantage of the redundancy, is given.

Chapter 4 describes the multivariable linear control system designs and their evaluation. Also a comparison between the LQG/LTR and H_∞ design methodologies is provided.

Chapter 5 demonstrates the flexibility offered by the pseudocontrol formulation by considering cases of failures in certain control surfaces.

Chapter 6 contains a summary, conclusions and suggestions for future research necessary to improve the design techniques.

CHAPTER 2

SYSTEM DESCRIPTION AND MODEL FORMULATION

2.1 Introduction

This chapter contains a short description of the aircraft configuration with special focusing on the control system. In addition modeling and maneuvering aspects are briefly discussed. For readers unfamiliar with aircraft and related terminology, reference [13] provides a good background. Finally, information about the trim points under consideration is provided .

2.2 Description of the F18 HARV Aircraft

The F18 High Alpha Research Vehicle is a modified version of the McDonnell Douglas F/A-18 Navy "Hornet" fighter-attack aircraft. The F18 HARV incorporates a thrust vectoring control system (TVCS) into the already powerful F/A-18 aircraft. The TVCS, currently under investigation, is expected to provide additional maneuverability even at high angle of attack ("alpha") and low speed where the other aerodynamic controls become less effective.

The F/A-18 configuration details shown in Figure 2.1 include a low sweep, trapezoidal wing platform with 400 ft² area, short coupled twin vertical tails, two GE F404

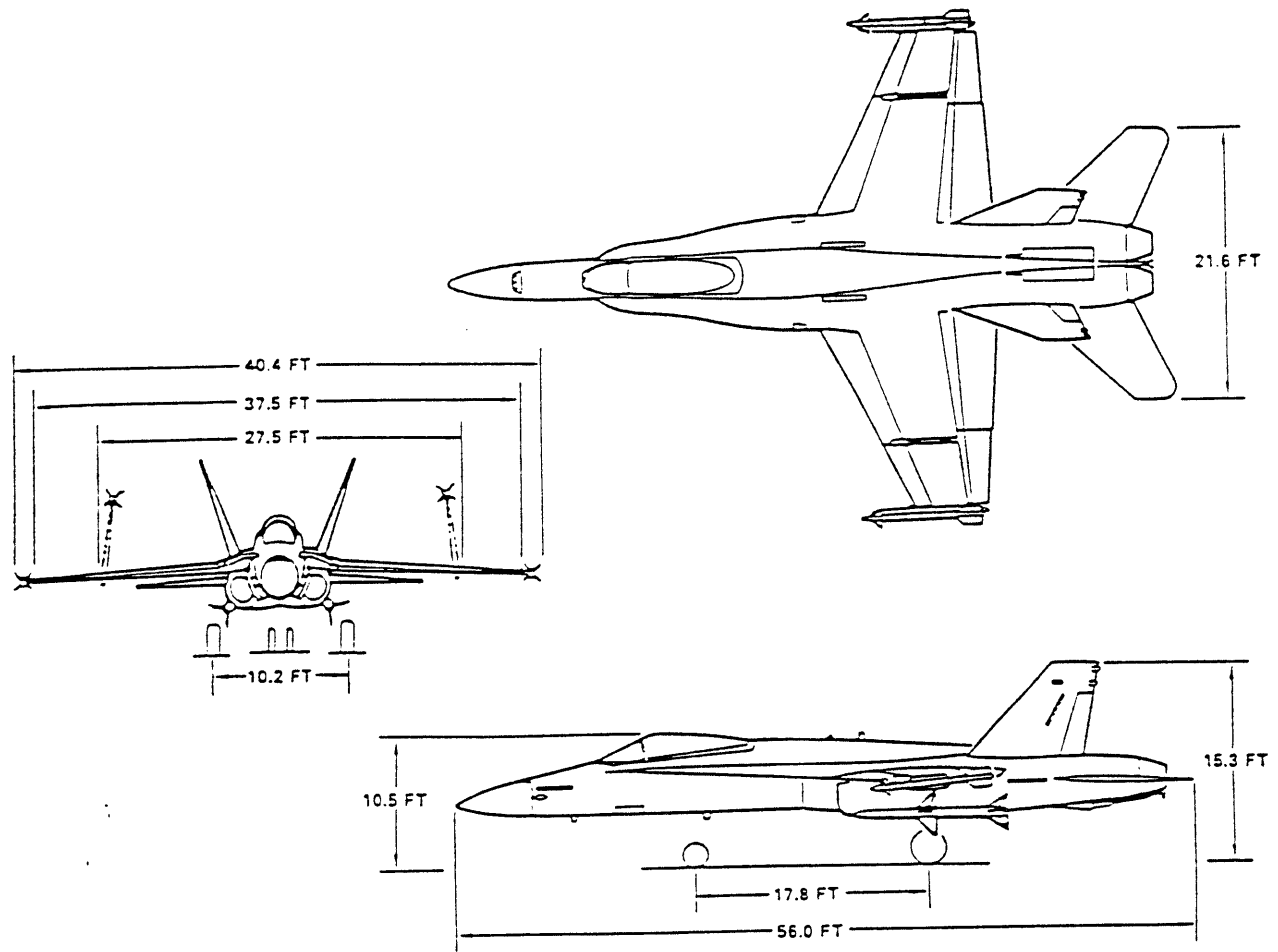


Figure 2.1 : The F/A-18 Navy "Hornet" aircraft

turbojets each with 16,000 pounds sea level static, maximum power thrust, and a large leading edge extension (LEX).

The aerodynamic control surfaces illustrated in figure 2.2 are:

(i) A large span, single slotted trailing edge flap capable of 45° deflection in the landing configuration but doubling as a differential flaperon with $\pm 8^\circ$ deflection in the up-and-away maneuvering configuration. In addition, these flaps are scheduled with angle of attack and

Mach number for optimization of drag and stability.

(ii) Single slotted, drooped ailerons for takeoff and landing, with $\pm 25^\circ$ deflection for up-and-away

conditions.

(iii) Leading edge flaps which are scheduled with angle of attack and Mach number to a maximum

of 34° down. In addition, they are used differentially $\pm 3^\circ$ for roll augmentation.

(iv) Twin rudders which are used for the normal purposes of directional control and roll coordination

but which are used also for enhancement of longitudinal stability and control in the takeoff and

landing configurations.

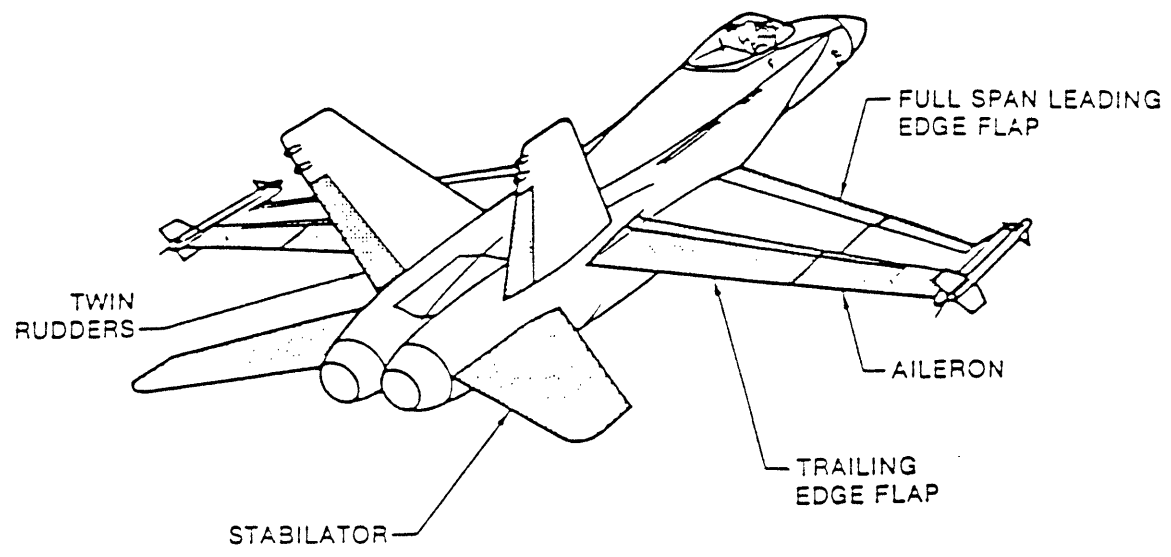


Figure 2.2 : Aerodynamic control surfaces

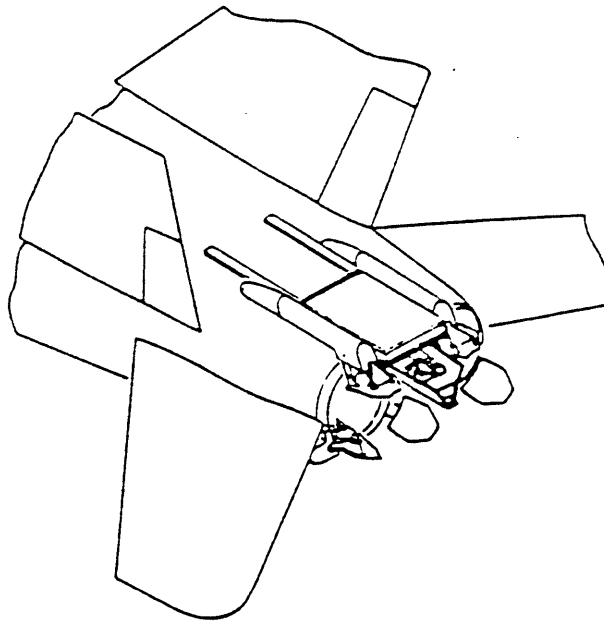


Figure 2.3 : F18/HARV thrust vectoring vane system

(v) And last, an all-moveable stabilator with differential deflection for roll.

Apart from the aerodynamic control surfaces, the vehicle includes the following propulsive control elements:

(v) Throttle position which regulates the thrust delivered by the engine.

(vi) Thrust vectoring vane system (figure 2.3) which regulates the angle at which the thrust is applied on the aircraft. This control capability, as stated previously, is the special feature of the F18/HARV.

Thrust-vectoring engine nozzles raise new possibilities for controlling future generations of jet airplanes. Aerodynamic control surfaces are conventionally used to generate the moments required to pitch, roll, and yaw airplanes. These moments become weak during low-speed flight because of low dynamic pressure. At high angles of attack, aerodynamic controls are corrupted by cross-axis coupling terms, which further complicate the design of the flight control system. Thrust-vectoring controls, on the other hand, are especially effective when the dynamic pressure is relatively low. The moments generated by thrust vectoring controls (figure 2.4) remain aligned with the axes of the airplane regardless of the angle of attack. Pitch moments are generated by simultaneously vectoring the engine nozzles in pitch plane of the airplane. Yawing moments are generated by simultaneously vectoring the nozzles laterally. Rolling moments are generated by differentially vectoring the nozzles in the pitch plane. This thrust vectoring capability permits controlled flight at high angles of attack and low airspeeds, at which the aerodynamic controls are ineffective.

The incorporation of thrust-vectoring controls into jet airplane designs promises to extend the low-speed region of the flight envelope and may influence inflight maneuver capabilities and airfield operations. In addition, thrust-vectoring controls provide redundancy for the aerodynamic controls, which is a significant advantage in the event of actuator failures.

In practice the control signals will be generated by an on-board computer which processes the information from the sensors. A description of the on-board sensor/computer/actuator system of the F18/HARV is shown in figure 2.5.

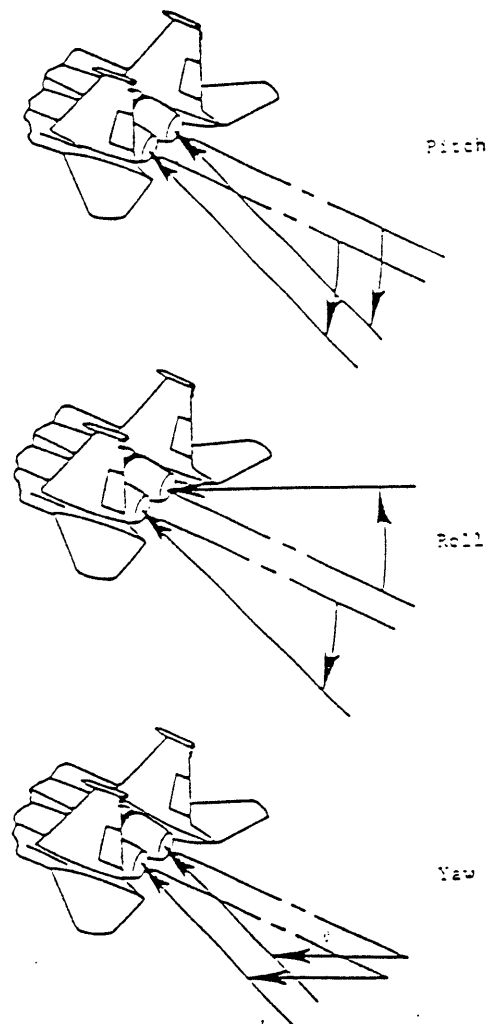


Figure 2.4 : Thrust vectoring control moments

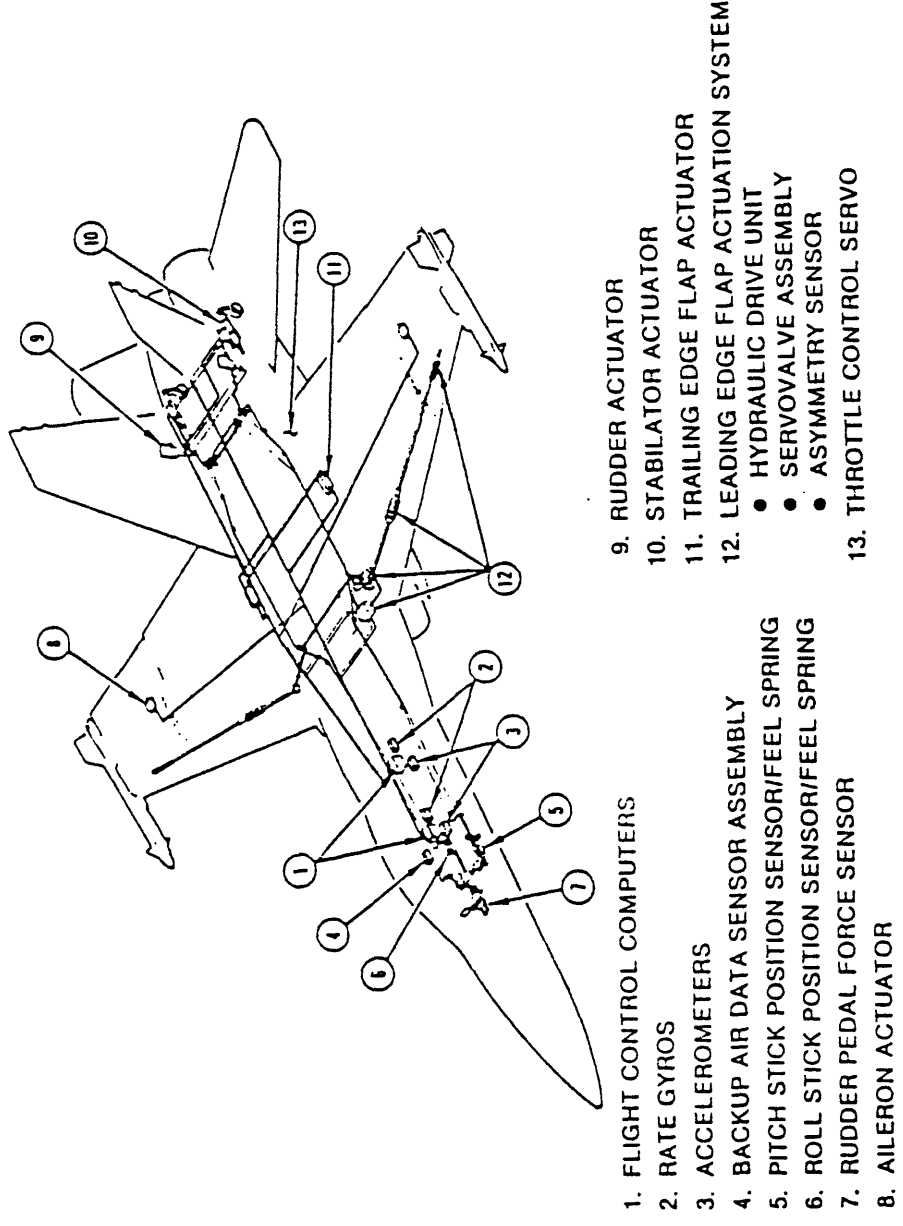


Figure 2.5 : F/A-18 flight control configuration

2.3 The F18/HARV Model

2.3.1 Introduction

The equations describing the motion of an aircraft subject to aerodynamic propulsive, and gravitational forces are highly nonlinear functions of many variables [13]. However, linearization of these complicated equations around an operating point provides excellent representation of the motion of the aircraft about that specific trim point. It is these linear equations that control engineers use to obtain linear time invariant (LTI) controller designs at each operating point. The linearization technique is briefly explained in the following section.

2.3.2 Development of Linear Models

The nonlinear equations arising from the balance of forces and moments acting on the aircraft can be described in general as

$$\dot{\mathbf{x}}(t) = \mathbf{f}(\mathbf{x}(t), \mathbf{u}(t)) \quad (2.3.1)$$

where $\mathbf{x}(t)$ is the state vector and $\mathbf{u}(t)$ is the control input vector. If $\mathbf{x}_0, \mathbf{u}_0$ represents a particular operating point (i.e. an equilibrium point of the state vector $\mathbf{x}(t)$ with specific

values of the control input vector $\mathbf{u}(t)$, then

$$\mathbf{f}(\mathbf{x}_0, \mathbf{u}_0) = \mathbf{0} \quad (2.3.2)$$

Assuming small state and control perturbations $\delta\mathbf{x}(t)$, $\delta\mathbf{u}(t)$, around this equilibrium point, taking into account (2.3.2), and using Taylor's expansion formula, equation (2.3.1) becomes:

$$\delta\dot{\mathbf{x}}(t) = \left. \frac{\partial \mathbf{f}(\mathbf{x}(t), \mathbf{u}(t))}{\partial \mathbf{x}(t)} \right|_{\mathbf{x}_0, \mathbf{u}_0} \delta\mathbf{x}(t) + \left. \frac{\partial \mathbf{f}(\mathbf{x}(t), \mathbf{u}(t))}{\partial \mathbf{u}(t)} \right|_{\mathbf{x}_0, \mathbf{u}_0} \delta\mathbf{u}(t) + \text{higher order terms}$$

Neglecting the higher order terms the linear model about the equilibrium point $\mathbf{x}_0, \mathbf{u}_0$ can be represented as:

$$\delta\dot{\mathbf{x}}(t) = \mathbf{A}\delta\mathbf{x}(t) + \mathbf{B}\delta\mathbf{u}(t) \quad (2.3.3)$$

where

$$\mathbf{A} = \left. \frac{\partial \mathbf{f}(\mathbf{x}(t), \mathbf{u}(t))}{\partial \mathbf{x}(t)} \right|_{\mathbf{x}_0, \mathbf{u}_0}, \quad \mathbf{B} = \left. \frac{\partial \mathbf{f}(\mathbf{x}(t), \mathbf{u}(t))}{\partial \mathbf{u}(t)} \right|_{\mathbf{x}_0, \mathbf{u}_0}$$

Linear models for the F18/HARV at various trim points were provided by NASA Langley. The local behavior of the aircraft at a particular operating point is described by 10 states $\mathbf{x}(t)$ and 13 control inputs $\mathbf{u}(t)$ in the form

$$\dot{\mathbf{x}}(t) = \mathbf{A}\mathbf{x}(t) + \mathbf{B}\mathbf{u}(t), \quad \mathbf{A} \in \mathbf{R}^{10 \times 10}, \quad \mathbf{B} \in \mathbf{R}^{10 \times 13}$$

where $\mathbf{x}(t) = [V_T \quad \alpha \quad \beta \quad p \quad q \quad r \quad \phi \quad \theta \quad \psi \quad h]^T$

and

$$\mathbf{u}(t) = [\delta_{TVL} \delta_{TVR} \delta_{RL} \delta_{RR} \delta_{AL} \delta_{AR} \delta_{SL} \delta_{SR} \delta_{LEL} \delta_{LER} \delta_{TEL} \delta_{TER} \delta_T]^T$$

with the relevant definitions , notations and units given in table 2.1

Table 2.1: Definitions, Notation and Units

States:	V_T : perturbation in true airspeed	ft/s
	α : perturbation in angle of attack	rad
	β : perturbation in sideslip angle	rad
	p : perturbation in roll rate	rad/sec
	q : perturbation in pitch rate	rad/sec
	r : perturbation in yaw rate	rad/sec
	ϕ : perturbation in roll angle	rad
	θ : perturbation in pitch angle	rad
	ψ : perturbation in yaw angle	rad
	h : perturbation in altitude	ft.
Controls:	δ_{TVL} : perturbation in left thrust vectoring vane deflection	deg
	δ_{TVR} : perturbation in right thrust vectoring vane deflection	deg
	δ_{RL} : perturbation in left rudder deflection	deg
	δ_{RR} : perturbation in right rudder deflection	deg
	δ_{AL} : perturbation in left aileron deflection	deg
	δ_{AR} : perturbation in right aileron deflection	deg
	δ_{SL} : perturbation in left stabilator deflection	deg
	δ_{SR} : perturbation in right stabilator deflection	deg
	δ_{LEL} : perturbation in left leading edge flap deflection	deg
	δ_{LER} : perturbation in right leading edge flap deflection	deg
	δ_{TEL} : perturbation in left trailing edge flap deflection	deg
	δ_{TER} : perturbation in right trailing edge flap deflection	deg
	δ_T : perturbation in throttle position.	deg

An advantage of the linearized model is that the longitudinal and lateral-directional dynamics can be practically decoupled. To do this, one has to form a new set of control inputs each consisting of a symmetric and a differential part. We now explain how this is done.

A symmetric input is the sum of the left (L) and right (R) components of a particular control element. A differential input is the difference between the left and right components of a control element. Thus, if x represents any of the control elements: thrust vectoring (TV), aileron (A), stabilator(S), leading edge flap (LE), trailing edge flap (TE), rudder (R), the symmetric and differential inputs are as follows:

$$\delta_{XS} = \delta_{XL} + \delta_{XR} \quad (2.3.4)$$

$$\delta_{XD} = \delta_{XL} - \delta_{XR} \quad (2.3.5)$$

where S stands for symmetric, D for differential.

By doing so, the dynamics of the aircraft can be described in a practically decoupled form as follows:

$$\frac{d}{dt} \begin{bmatrix} \mathbf{x}_{long} \\ \mathbf{x}_{lat} \end{bmatrix} = \begin{bmatrix} \mathbf{A}_{long} & \mathbf{0}_{5 \times 5} \\ \mathbf{0}_{5 \times 5} & \mathbf{A}_{lat} \end{bmatrix} \begin{bmatrix} \mathbf{x}_{long} \\ \mathbf{x}_{lat} \end{bmatrix} + \begin{bmatrix} \mathbf{B}_{long} & \mathbf{0}_{5 \times 7} \\ \mathbf{0}_{5 \times 6} & \mathbf{B}_{lat} \end{bmatrix} \begin{bmatrix} \mathbf{u}_{long} \\ \mathbf{u}_{lat} \end{bmatrix} \quad (2.5.6)$$

with $\mathbf{A}_{long}, \mathbf{A}_{lat} \in \mathbb{R}^{5 \times 5}$, $\mathbf{B}_{long} \in \mathbb{R}^{5 \times 6}$, $\mathbf{B}_{lat} \in \mathbb{R}^{5 \times 7}$,

$$\mathbf{x}_{long} = [V_T \ \alpha \ q \ \theta \ h]^T,$$

$$\mathbf{u}_{long} = [\delta_{TVS} \ \delta_{AS} \ \delta_{SS} \ \delta_{LES} \ \delta_{TES} \ \delta_T]^T,$$

$$\mathbf{x}_{lat} = [\beta \ p \ r \ q \ \psi]^T \quad \text{and}$$

$$\mathbf{u}_{lat} = [\delta_{TVD} \ \delta_{AD} \ \delta_{SD} \ \delta_{LED} \ \delta_{TED} \ \delta_{RD} \ \delta_{RS}]^T$$

Further on, the states h (perturbation in altitude) and ψ (perturbation in yaw angle) can be eliminated from the state space equation as redundant since they do not affect (at least to good approximation) the rest of the states; in addition, and also they cannot be affected by the controls.

In this thesis only the longitudinal behavior of the aircraft was studied, therefore the linear model describing the longitudinal dynamics of the F18/HARV consists of four states and six controls inputs and is of the form

$$\dot{\mathbf{x}}(t) = \mathbf{A}\mathbf{x}(t) + \mathbf{B}\mathbf{u}(t) \quad \mathbf{A} \in \mathbb{R}^{4 \times 4} \quad \mathbf{B} \in \mathbb{R}^{4 \times 6} \quad (2.3.7)$$

where

$$\mathbf{x}(t) = [V_T \quad \alpha \quad q \quad \theta]^T$$

$$\mathbf{u}(t) = [\delta_{TVS} \quad \delta_{AS} \quad \delta_{SS} \quad \delta_{LES} \quad \delta_{TES} \quad \delta_T]^T$$

For fighter aircraft three longitudinal precision control modes are of major importance [18].

These control modes are illustrated schematically in figure 2.8 and listed below:

1. Vertical translation
2. Pitch pointing
3. Direct lift

In the vertical translation mode the flight path angle $\gamma(=\theta-\alpha)$ is changed, while the pitch angle θ is maintained constant. Equivalently, this means that the vertical component of velocity ($V_T \tan \gamma$) changes without altering the pitch angle θ .

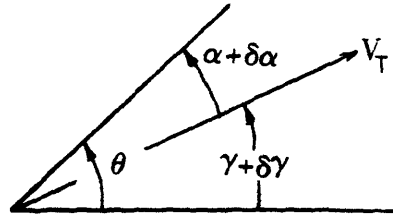
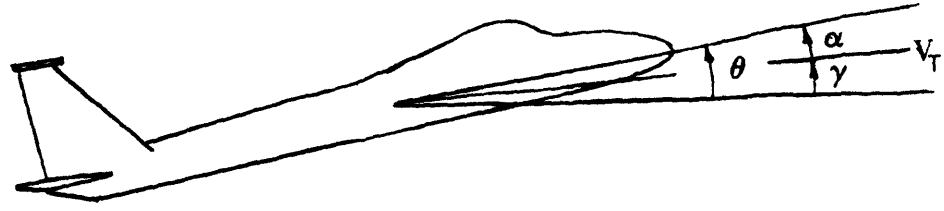
The pitch pointing mode consists of a change in pitch angle θ while the flight path angle γ is kept constant. For example, the pilot may wish to point the fuselage at another aircraft in space, so as to deliver ordinance, without disrupting his aircraft trajectory.

Finally, in the direct lift mode, both the flight path angle γ and pitch angle θ change in such a way that the angle of attack α is maintained constant.

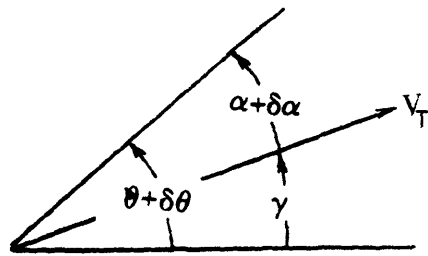
In this thesis we address three operating points. They are depicted in table 2.2. Each of them represents horizontal flight at an altitude of 15,000 ft. Each point, however, has a different Mach number. The first one is a "hard" trim point at a high angle of attack ($\alpha=25$ deg) and at low speed. In situations like this, as stated before in this chapter, the role of the thrust vectoring control is expected to be important. Also, the fact that the above trim point is unstable (see chapter 3) makes it a challenging case. The remaining two operating points are more conventional cases where the role of thrust vectoring capability is not expected to be significant. The numerical values for the A and B matrices in equation (2.3.7), for all three operating conditions, are given in the Appendix A2.

These operating points were selected in order to get an idea of the capabilities of the aircraft and how these capabilities are affected by changing trim points at the 15,000 ft altitude level.

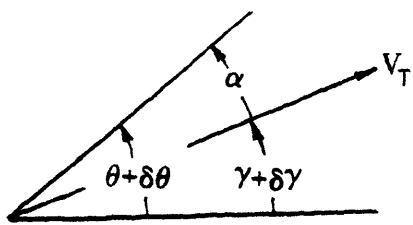
Intuitively, one should expect that at operating points 2 and 3 maneuvering can be easier (i.e. faster response time with less control effort) accommodated than at operating point 1.



a) Vertical Acceleration ($\theta = \text{constant}$)



b) Pitch Pointing ($\gamma = \text{constant}$)



c) Direct Lift ($\alpha = \text{constant}$)

Figure 2.6: Longitudinal Precision Control Modes

Table 2.2

Selected operating points

Altitude (h) ₀ [ft]	15000	15000	15000
Mach Number (M)	0.24	0.46	0.6
Airspeed (V _T) ₀ [ft/sec]	238.7	487.3	634.3
Angle of Attack (α) ₀ [deg]	25	5	2.95
Pitch Rate (q) ₀ [deg/sec]	0	0	0
Pitch Angle (θ) ₀ [deg]	25	5	2.95
Path Angle (γ) ₀ [deg]	0	0	0
Sym. Thrust Vectoring Vane Deflection (δ _{TVS}) ₀ = = (δ _{TVL}) ₀ - (δ _{TVR}) ₀ [deg]	0+0	0+0	0+0
Sym. Aileron Deflection (δ _{AS}) ₀ = (δ _{AL}) ₀ + (δ _{AR}) ₀ [deg]	0+0	0+0	0+0
Sym. Stabilator Deflection (δ _{SS}) ₀ = (δ _{SL}) ₀ + (δ _{SR}) ₀ [deg]	(-6.4)+(-6.4) 0.15)	(-0.65)+(-0.65)	(-0.15)+(-
Sym. Leading Edge Flap Deflection (δ _{LES}) ₀ = =(δ _{LEL}) ₀ + (δ _{LER}) ₀ [deg]	0.33+0.33	6.64+6.64	3.9+3.9
Sym. Trailing Edge Flap Deflection (δ _{TES}) ₀ = =(δ _{TEL}) ₀ + (δ _{TER}) ₀ [deg]	0.8+0.8	7+7	4.1+4.1
Throttle Position (δ _T) ₀ [deg]	100.5	70.3	72.4

2.4 Summary

This chapter provides some essential information so that the reader develops an idea of the physical system to be controlled. The linearization around an operating is highlighted in this chapter. The linear models available are proven to be very convenient, because by splitting the control inputs into symmetric and differential part one can practically decouple the longitudinal and the lateral -directional dynamics. The resulting subsystem describing the longitudinal dynamics consists of 4 states and 6 controls. It is this system that we will be dealing with in the following chapters.

CHAPTER 3 ANALYSIS OF LINEAR MODELS

3.1 Introduction

The linear models describing the longitudinal dynamics at each of the 3 operating conditions of the F18/HARV were presented in chapter 2. In this chapter these models are analyzed. The natural modes will be identified and discussed. Also, the outputs to be controlled will be selected and the issue of scaling of the variables will be addressed. Finally, a method which exploits the control redundancy of the F18/HARV will be presented.

3.2 Natural Modes of the F18/HARV

The linear model describing the longitudinal dynamics of the aircraft has, as mentioned in chapter 2, four state variables. These are the true airspeed V_T , the angle of attack α , the pitch rate q and the pitch angle θ . The open loop poles for the three operating points selected are shown in table 3.1. As it can be noticed the open loop poles consist of two complex conjugate pairs; one pair being relatively fast and the other pair relatively slow. These two pairs of complex conjugate poles together with the corresponding eigenvectors are identified respectively as the short period mode and the plugoid mode.

The short period mode represents a motion of constant (undisturbed) velocity with small deviation of flight path and a rapid rotation of the aircraft in pitch and consequently fast changes in angle of attack. It is due to the "arrow stability" of the aircraft and it is in general well damped.

The phugoid mode represents an interchange of potential and kinetic energy with a practically undisturbed angle of attack. It is a very slightly damped mode. For operating point 1 this mode is unstable. Figure 3.1 [13] illustrates the implied motion of each mode for a conventional aircraft.

Table 3.1
Open Loop poles at operating points 1, 2, and 3

Operating Point	Open Loop Poles	Damping Ratio ζ	Natural Frequency
1	$+ 0.0188 \pm 0.1280j$	- 0.14	0.13
	$- 0.2481 \pm 0.3585j$	0.57	0.44
2	$-0.0021 \pm 0.0697j$	0.03	0.07
	$-0.5480 \pm 1.3445j$	0.38	1.45
3	$-0.0049 \pm 0.0665j$	0.07	0.07
	$-0.7481 \pm 2.2758j$	0.31	2.40

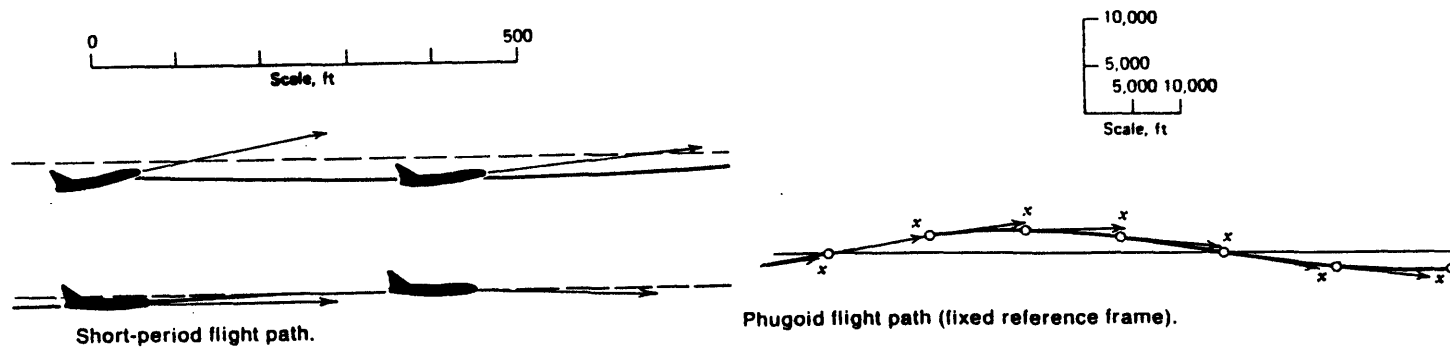


Figure 3.1: Longitudinal natural modes

3.3 Selection of Outputs to be Controlled

By the linearization process discussed in chapter 2, the outputs to be controlled can be expressed as linear combinations of the state vector $x(t)$ and the control input $u(t)$ in the form

$$y(t) = Cx(t) + Du(t) \quad (3.3.1)$$

We assume that the outputs in $y(t)$ are measurable. These output are measured on-line and compared with "desired" outputs (ie. reference commands inputs) by forming an error signal and using this error signal to generate the appropriate control inputs to the actuator servos.

In order to select output variables a control engineer must first ascertain the degree to which the control inputs can be used to independently control outputs. This can be done by examining the **B** matrix.

Examining the structure of the linear model, as shown in Appendix (A2) one can see that the input matrix **B** has rank three. This implies that, in principle, the maximum number of variables that can be controlled independently is three. Furthermore, in order for the pilot to execute successfully the longitudinal maneuvers discussed in chapter 2, he should be able at least, to control independently the flight path angle γ as well as the pitch angle θ . Also, independent and simultaneous control of the airspeed V_T would offer the pilot a great deal of flexibility. For these reasons the outputs to be controlled were chosen as follows:

$$y = \begin{bmatrix} \text{true airspeed } V_T \\ \text{flight path angle } \gamma \\ \text{pitch angle } \theta \end{bmatrix} \quad (3.3.2)$$

It should be noted that, in general, these variables may not be explicitly monitored. Usually accelerations and rates rather than positions are readily measured. Therefore, feeding back the variables of (3.3.2) may be impossible. In this thesis however, it was assumed that the variables in (3.3.2) are measurable and can be used to generate control signals.

3.4 Scaling of Linear Model

Scaling of the variables plays a very important role in multivariable control design [1]. By scaling, the physical units can be eliminated and their interactions are easier to compare and understand. For example, comparing 1 ft/sec deviation from trim airspeed with 1 radian deviation from trim angle of attack does not make a lot of sense from a practical point of view. In fact, one might argue that these deviations are "not comparable".

What does make sense, however, is to compare deviations normalized by scale factors such that 1 unit deviation from trim airspeed would be of "equal importance" as 1 unit deviation from trim angle of attack. Having a knowledge of the system (sizes, physical quantities involved, trim conditions etc.) is helpful, since one can establish a relative

importance type of scaling. Once the outputs to be controlled and the scaling factors have been decided, it is easy to obtain the scaled system state representation using simple linear algebra as follows:

We assume that the state space representation of the unscaled linear model of the aircraft is given by

$$\dot{\mathbf{x}}(t) = \mathbf{A}\mathbf{x}(t) + \mathbf{B}\mathbf{u}(t) \quad (3.3.1a)$$

and

$$\mathbf{y}(t) = \mathbf{C}\mathbf{x}(t) \quad (3.3.1b)$$

The scaled states, controls, and outputs $\mathbf{x}_s(t)$, $\mathbf{u}_s(t)$, and $\mathbf{y}_s(t)$ are then given by:

$$\mathbf{x}_s(t) = \mathbf{S}_x \mathbf{x}(t)$$

$$\mathbf{u}(t) = \mathbf{S}_u \mathbf{u}_s(t) \quad (3.3.2)$$

$$\mathbf{y}_s(t) = \mathbf{S}_y \mathbf{y}(t)$$

Substituting (3.3.2) into (3.3.1a,b) gives us the scaled linear model:

$$\dot{\mathbf{x}}_s(t) = \mathbf{S}_x^{-1} \mathbf{A} \mathbf{S}_x \mathbf{x}_s(t) + \mathbf{S}_x \mathbf{B} \mathbf{S}_u^{-1} \mathbf{u}_s(t) \quad (3.3.3a)$$

and

$$\mathbf{y}_s(t) = \mathbf{S}_y \mathbf{C} \mathbf{S}_x^{-1} \mathbf{x}_s(t) \quad (3.3.3b)$$

As a first step, scaling was performed in order to convert radians to degrees. Then, a relative importance scaling was established. In particular, it was assumed that one degree deviation from trim of path angle γ was equally important with one degree deviation from trim of pitch angle θ , for every operating point considered. The scaling of the airspeed deviation from trim depended on the operating point, since the trim airspeed is much different from point to point.

The scaling of the controls was done using the saturation levels. In particular, with the exception¹ of the symmetric trailing edge flap at operating point 1, the saturation limits were taken to be smallest angle (in absolute sense) between the trim and the two limits in the up or down direction (table 3.2). Obviously, up and down direction does not make a lot of sense for the throttle position. In this case up was considered to be the smallest value whereas down the maximum value.

The scaling factors of inputs and outputs for the three operating points are shown in table (3.3). The state space representation of the scaled linear models are given in the Appendix (A2).

¹ For the commanded maneuvers (chapter 4) the trailing edge flap is expected to move primarily downwards. Taking also into account that operating condition 1 represents a hard trim, it was judged to be quite conservative to scale this effective control input with the least margin (in the upwards direction) of $14=(7+7)$ deg

Table 3.2
Saturation Limits

Control	δ_{TV}	δ_A	δ_S	δ_{LE}	δ_{TE}	δ_T
up direction limit (deg)	-25	-25	-24	-3	-8	54
down direction limit (deg)	25	45	10.5	34	45	127

Table 3.3
Scaling Factors

Variables	Op. Point 1	Op. Point 2	Op. Point 3
V_T	1/8 ft/sec	1/30 ft/sec	1/20 ft/sec
γ	1/1 deg	1/1 deg	1/1 deg
θ	1/1 deg	1/1 deg	1/1 deg
δ_{TVS}	1/(25+25)deg	1/(25+25)deg	1/(25+25)deg
δ_{AS}	1/(25+25)deg	1/(25+25)deg	1/(25+25)deg
δ_{SS}	1/(17+17)deg	1/(11+11)deg	1/(10.5+10.5)deg
δ_{LES}	1/(1+1)deg	1/(10+10)deg	1/(7+7)deg
δ_{TES}	1/(30+30)deg	1/(15+15)deg	1/(12+12)deg
δ_T	1/27 deg	1/16 deg	1/20 deg

3.5: Control Redundancy of the F18/HARV

3.5.1: Introduction

As stated in section 3.3.1 the rank of the input matrix **B** is equal to three. Therefore, the question to be answered is how to select among the six available control inputs three of them or three independent combinations of them that will be used to design the compensator.

One approach would be to select the three that would be expected to perform the best to the demands of the specifications, based on the physical intuition and knowledge of the system. For example, if the specifications on the controller asked primarily for pitch pointing capability, then the choice of thrust vectoring, stabilator and, possibly, of the trailing edge flap as the control inputs to use while discarding the rest, would have made sense.

Another way would be to use steady state (DC) analysis to decide which controls affect the most the outputs at steady state. In particular, the use of singular value decomposition at DC can be used as a tool to successfully do so.

One more option is the so called "relative control effectiveness technique" [17]. By this method a set of pseudocontrols is formed in such a way that each pseudocontrol strongly affects selected fundamental modes of the system while only weakly affecting the remaining modes.

All of the above methods however, lack flexibility since the freedom offered by the redundancy of the controls is not utilized. To be more clear, in the methods above, the combinations of the controls are prespecified. If, however, for some reason a certain

control cannot operate (e.g. actuator failure), then the need for redesign of the compensator is essential.

The approach used in this thesis overcomes the shortcomings of the above methods by taking advantage of the redundancy in control inputs. The following section describes how the input signals were selected.

3.5.2 Procedure for Selection of Pseudocontrols

From this point on matrices A, B, C refer to the scaled model. Since $\text{rank}(B)=3$, it is evident that in the state space description of the linear model the term

$$Bu(t)$$

with $B \in \mathbb{R}^{4 \times 6}$, $u(t) \in \mathbb{R}^{6 \times 1}$ can be equivalently replaced by:

$$B_v v(t)$$

with B_v any matrix $\in \mathbb{R}^{4 \times 3}$ such that the space spanned by the columns of B_v is identical to the space spanned by the columns of B and $v(t)$ any vector $\in \mathbb{R}^{3 \times 1}$. The input $v(t)$ is a fictitious one and, therefore, is called pseudocontrol. Taking into account the specific structure of B since

$$\mathbf{B} = \begin{bmatrix} \mathbf{B}_1 \\ \leftarrow \mathbf{0}_{1 \times 6} \rightarrow \end{bmatrix} \quad (3.4.1)$$

with $\text{rank}(\mathbf{B}_1)=3$,

it is easy to see that a legitimate \mathbf{B}_v is the following:

$$\mathbf{B}_v = \begin{bmatrix} \mathbf{I}_{3 \times 3} \\ \mathbf{0}_{1 \times 3} \end{bmatrix} \quad (3.4.2)$$

Thus, the state space description of the "pseudo system" when the fictitious input vector $\mathbf{v}(t)$ is used in

$$\dot{\mathbf{x}}(t) = \mathbf{A}\mathbf{x}(t) + \mathbf{B}_v\mathbf{v}(t) \quad (3.4.3a)$$

$$\mathbf{y}(t) = \mathbf{C}\mathbf{x}(t) \quad (3.4.3b)$$

with \mathbf{B}_v given by (3.4.2).

Clearly, the system above is a square system (#inputs = #outputs) and a square compensator based on the pseudocontrols $\mathbf{v}(t)$ can be designed.

What still remains to be answered, is how the pseudocontrol $\mathbf{v}(t)$ is going to be distributed to the actual control input $\mathbf{u}(t)$. Namely, the problem to be solved is the following:

Given a controller design based on the pseudocontrol $v(t)$ (i.e., given $v(t)$), find $u(t)$ subject to $Bu(t) = B_v v(t)$ which, in view of (3.4.1) and (3.4.2) can be replaced as:

$$B_1 u(t) = v(t) \quad (3.4.4)$$

Clearly, there will be infinite many $u(t)$ to satisfy (3.4.4) given $v(t)$. This is because the nullspace of B is nonempty. What needs to be found, is an optimal way of finding $u(t)$. An optimal way implies an optimality criterion and there are many of these. The optimization problem posed in this thesis is:

$$\begin{aligned} \text{minimize } J &= (u^T(t)W(t)u(t)) & (3.4.5) \\ u(t) &\in R^{6 \times 1} \end{aligned}$$

subject to $B_1 u(t) = v(t)$

with $W(t) = W^T(t)$ positive definite weighting matrix.

Thus, the pseudocontrol $v(t)$ is distributed in such a way that the weighted "energy" of the actual control input $u(t)$ is minimized.

The above optimization problem has an explicit solution which can be found using several techniques. One technique uses the Lagrange multipliers as follows:

The optimal $u(t)$ has to satisfy:

$$\frac{\partial}{\partial u(t)} F(u(t), \lambda(t)) = 0 \quad (3.4.6)$$

$$\frac{\partial}{\partial \lambda(t)} F(\mathbf{u}(t), \lambda(t)) = 0 \quad (3.4.7)$$

with

$$F(\mathbf{u}(t), \lambda(t)) = \mathbf{u}^T(t) \mathbf{W} \mathbf{u}(t) - \lambda^T(t) (\mathbf{B}_1 \mathbf{u}(t) - \mathbf{v}(t)) \quad (3.4.8)$$

and $\lambda(t)$ any vector in $\mathbb{R}^{3 \times 1}$.

From (3.4.6) one gets

$$2 \mathbf{u}^T(t) \mathbf{W}(t) = 0$$

or

$$\mathbf{u}(t) = \frac{1}{2} \mathbf{W}^{-1}(t) \mathbf{B}_1^T \lambda(t) \quad (3.4.9)$$

Substituting (3.4.9) into (3.4.7) $\lambda(t)$ can be obtained as follows:

$$\lambda(t) = 2(\mathbf{B}_1 \mathbf{W}^{-1}(t) \mathbf{B}_1^T) \mathbf{v}(t) \quad (3.4.10)$$

Relations (3.4.9), (3.4.10) yield the optimal $\mathbf{u}(t)$

$$\mathbf{u}(t) = \mathbf{T}(t) \mathbf{v}(t) \quad (3.4.11)$$

with

$$\mathbf{T}(t) = \left[\mathbf{W}^{-1}(t) \mathbf{B}_1^T (\mathbf{B}_1 \mathbf{W}^{-1}(t) \mathbf{B}_1^T) \right] \quad (3.4.12)$$

The transformation $\mathbf{T}(t)$ is simply a right inverse of \mathbf{B}_1 . The benefits using the method described so far in this section come from the fact that there is a lot of freedom to distribute the pseudocontrols to the actual ones, once the design based on the pseudosystem is completed. For example, if for some reason certain controls cannot be fully used and the performance in terms of response to commands is desired to be maintained the same, then one simply has to change the distribution matrix \mathbf{T} by weighting heavily these controls. The great amount of flexibility this method offers is illustrated in chapter 5 where failures of control surfaces are considered.

A point to notice here is that the weighting matrix $\mathbf{W}(t)$ can be a continuous function of time, which allows continuous adjustments of the weights on each control input.

Another way of distributing the pseudocontrols is implied by the following optimization problem:

$$\min_{\mathbf{u}(t) \in \mathbb{R}^{6 \times 1}} \{ \max(|u_1|, |u_2|, \dots, |u_6|) \}$$

or equivalently expressed in terms of the ∞ norm

$$\min_{\mathbf{u}(t) \in \mathbb{R}^{6 \times 1}} \|\mathbf{u}(t)\|_{\infty}$$

subject to

$$\mathbf{B}_1 \mathbf{u}(t) = \mathbf{v}(t).$$

This problem is a purely linear programming problem and its solution cannot be given with a simple explicit formula as in the previous case. However, the solution can be obtained easily using standard linear programming algorithms (e.g. Simplex method). In this optimization problem the magnitude of the controls is minimized and thus saturation is avoided to the extent possible.

3.6 Frequency Domain Characteristics of the Pseudosystem

For reasons discussed in the previous section, the controller design will be based on the so called pseudosystem in which the term $Bu(t)$ is replaced by $B_v v(t) = [I_{3 \times 3} \ 0_{3 \times 1}]^T v(t)$ where $v(t)$ is the pseudocontrol input. The block diagram representation of the pseudosystem is shown in figure 3.2.

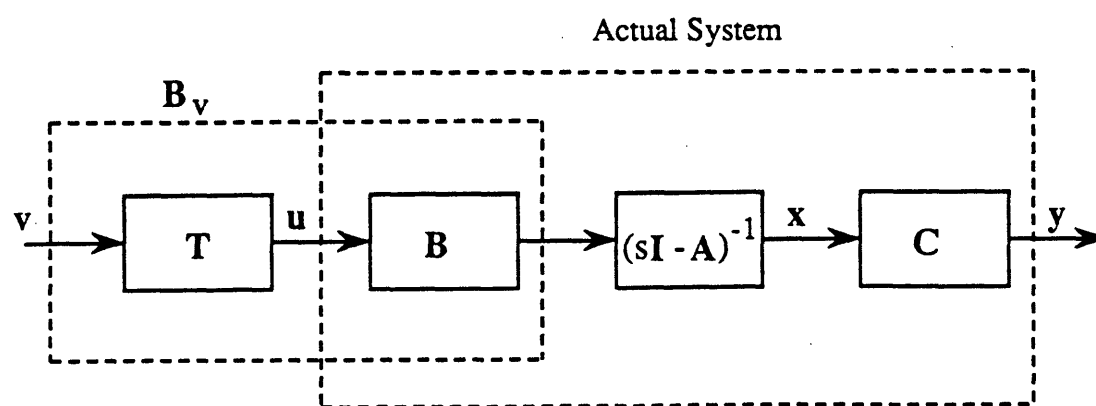


Figure 3.2 : Pseudosystem

The transfer function matrix from v to y is

$$\mathbf{G}_v(s) = \mathbf{C}(s\mathbf{I}-\mathbf{A})^{-1} \mathbf{B}_v \quad (3.5.1)$$

The singular value plots of $\mathbf{G}(j\omega)$ for the frequency range .001 to 100 rad/sec for the three operating points are shown respectively in figures 3.3, 3.4, 3.5. The resonant peak at the maximum singular value plot is due to the plungoid mode which is lightly damped. The short period mode does not exhibit such high resonance due to the fact that it is more damped.

The pseudosystem has no transmission zeros, a fact that guarantees recovery of the target loop in the LQG/LTR methodology. (see chapter 5).

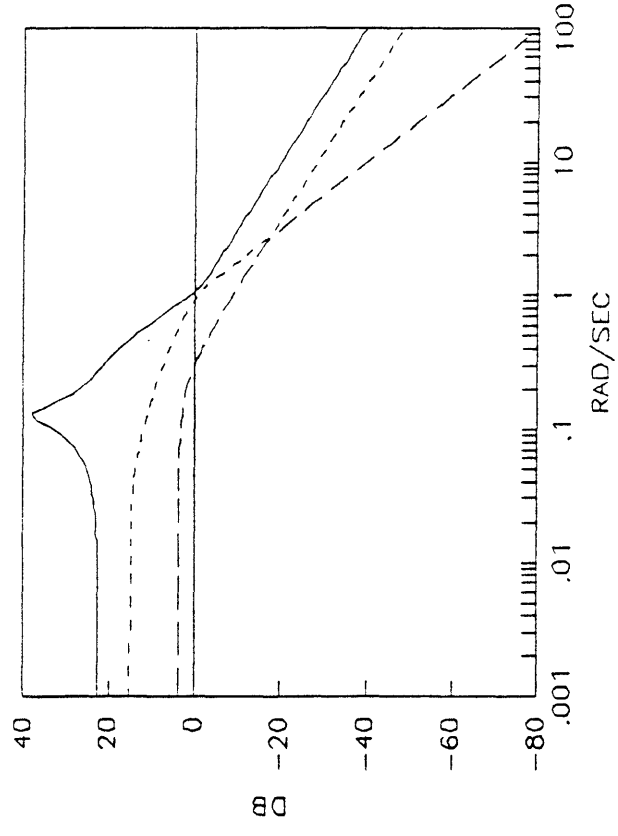


Figure 3.3 : Singular values of pseudosystem at point 1

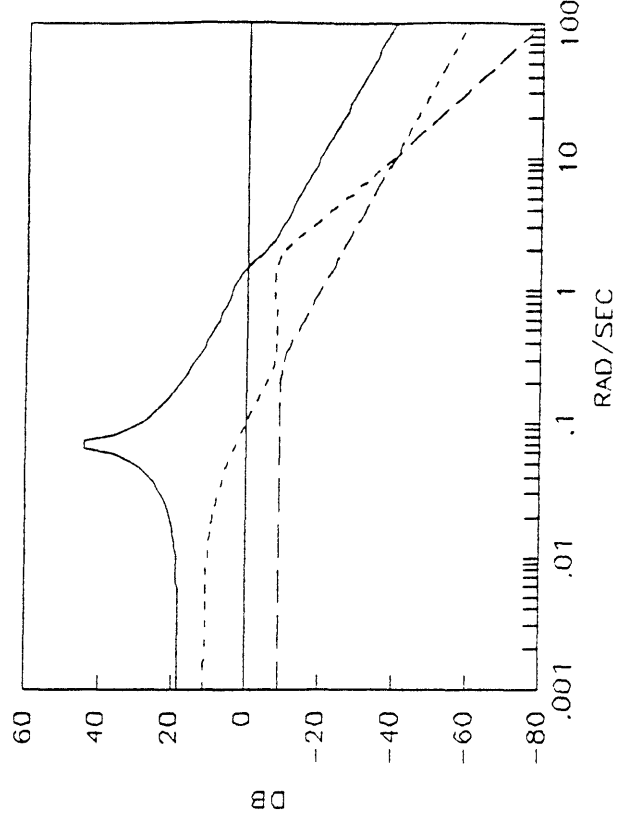


Figure 3.4 : Singular values of pseudosystem at point 2

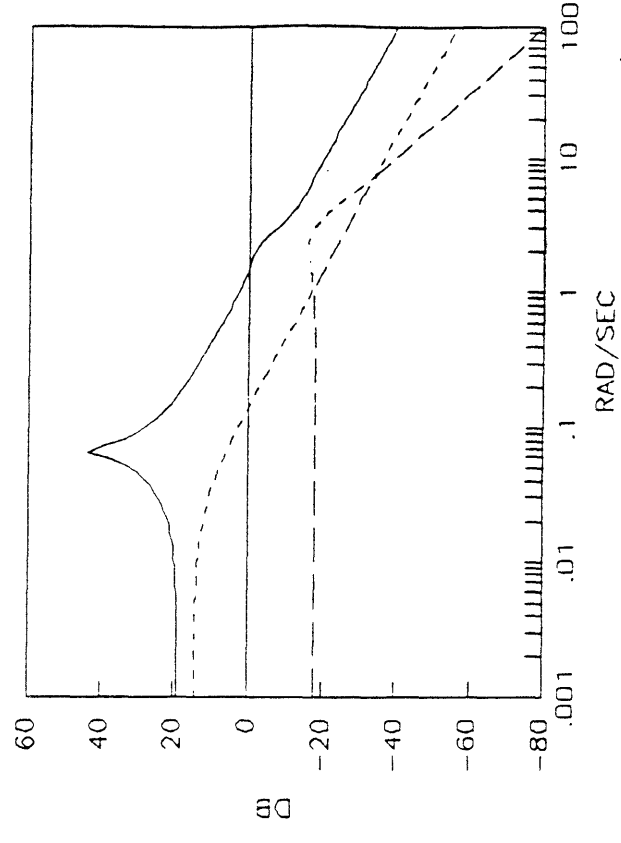


Figure 3.5 : Singular values of pseudosystem at point 3

3.7 Summary

In this chapter of the linear models were analyzed and scaled. The analysis showed that the traditional longitudinal modes of conventional aircrafts appear in fighter aircraft as well and their interpretation is more or less the same.

The analysis also showed that the maximum number of outputs that can be independently controlled is three. The airspeed, the flight path angle and the pitch angle were selected as outputs. The inputs, states and outputs of our three linear models were scaled so that the units reflect quantities which can be "justly compared".

The use of pseudocontrols takes full advantage of the redundancy of the control inputs and offers great amount of flexibility as it will be illustrated in chapter 5. One can use different optimality criteria to distribute the pseudocontrols to the actual ones. A convenient way to do this is by a quadratic criterion since an explicit formula for the solution is available.

CHAPTER 4

COMPENSATOR DESIGN

4.1 Introduction

This chapter applies the LQG/LTR design methodology to the three scaled linear models studied in chapter 3. The H_∞ design methodology is then applied to the scaled linear model associated with the first operating point.

Finally, comparisons are made and fundamental tradeoffs are described.

4.2 Design Specifications

The standard control system configuration is depicted in figure 4.1. We have to design a controller $K_O(s)$ for the linear model of the aircraft $G_O(s)$ at each of the selected operating points, that will perform certain tasks discussed in the sequel. As mentioned in chapter 3, the design will be based on the pseudosystem $G_v(s)$, meaning that a compensator $K_v(s)$ generating the pseudosignal $v(t)$ will be found (figure 4.2). Then, the "logic" T for distributing the pseudocontrol $v(t)$ to the actual control input $u(t)$ will be incorporated to the compensator structure.

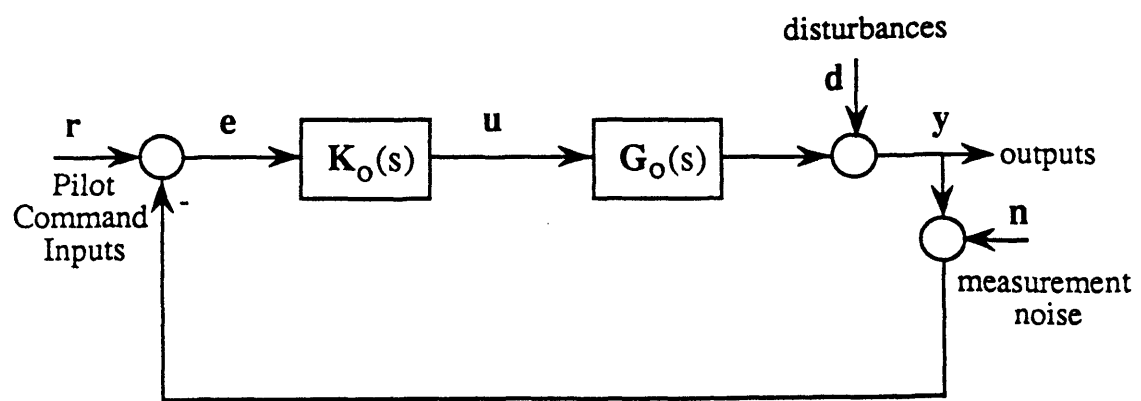


Figure 4.1: Control System Configuration for Actual System $G_O(s)$

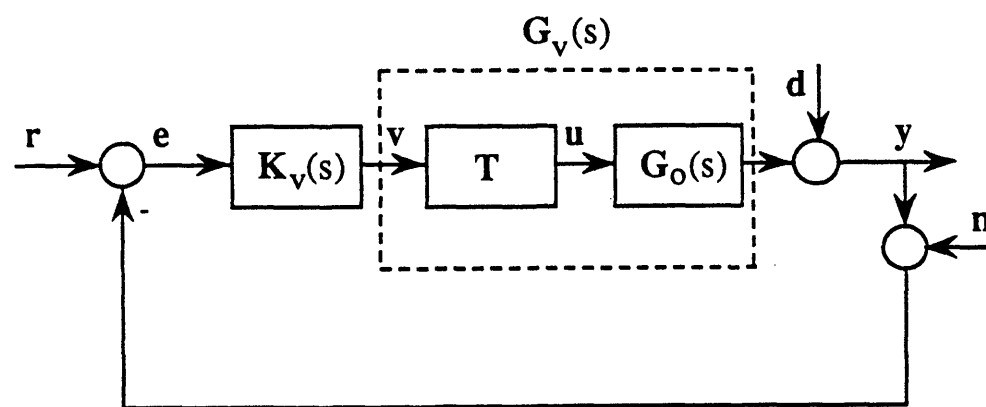


Figure 4.2: Control System Configuration for Pseudosystem

The requirements on the compensator are the following:

- a) Nominal Stability

The first thing one should ask from any feedback system is nominal stability. This means that the poles of the system in figure 4.2 (i.e. the closed loop poles) should have negative real parts (i.e. lie on the open left half of the complex plane).

b) Performance

The steady state error e to low frequency ($\omega < 0.1$ rad/sec) sinusoidal commands r or disturbances d should be "small". In particular,

(b1) $\|e\|_2 \leq .1$ for $\omega < .1$ rad/sec whenever $\|r\|_2 \leq 1$. or $\|d\|_2 \leq 1$.

(b2) Zero steady state error to constant commands or disturbances in all directions.

The system should be fast but excessive control action must be avoided. In particular, the system should

(b3) track the following step commands:

vertical translation $r_1 = [0 \ 1 \ 0]^T$

pitch pointing $r_2 = [0 \ 0 \ 1]^T$

direct lift $r_3 = [0 \ 1 \ 1]^T$

respecting the magnitude limits (see chapter 3, Table 3.2) as well as the following rate limits:

Thrust vectoring	60 deg/sec
Aileron	100 deg/sec
Stabilator	60 deg/sec
Leading edge flap	20 deg/sec
Trailing edge flap	60 deg/sec

Throttle 30 deg/sec

The system should be able to reject high frequency measurement noise n . In particular,

$$(b4) \|e\|_2 \leq .1 \text{ for } \omega > 20 \text{ rad/sec whenever } \|n\|_2 \leq 1$$

c) Stability robustness

The system should remain stable in the presence of low frequency uncertainty and high frequency unmodeled dynamics. In particular, the following should be fulfilled:

$$(c1) \text{ Multivariable downward gain margin at the plant output } GM\downarrow \leq 0.62 = -4.1\text{db}$$

$$\text{Multivariable upward gain margin at the plant output } GM\uparrow \geq 2.52 = 8.0\text{db}$$

$$\text{Multivariable phase margin at the plant output } |PM| \geq 35\text{deg.}$$

$$(c2) \text{ Stability in the presence of multiplicative error } \Delta(s) \text{ reflected at the plant output} \\ \text{that is bounded by } \delta(\omega) = 0.1 \omega \text{ for all } \omega .$$

The requirements posed previously can be reinterpreted as follows:

Specifications (b1), (b2) simply impose constraints on the sensitivity transfer function

$$S(s) = (I+G(s)K(s))^{-1}. \text{ Namely,}$$

$$\sigma_{\max}(S(j\omega)) \leq -20\text{db for } \omega \leq 0.1 \text{ rad/sec}$$

and

$$\sigma_{\max}(S(j\omega)) \rightarrow 0 \text{ as } \omega \rightarrow 0$$

Or translating, into the loop transfer function $G(s)K(s)$ shapes, since usually, for small ω

$$\sigma_{\min}(G(j\omega)K(j\omega)) \approx [\sigma_{\max}(S(j\omega))]^{-1},$$

$$\sigma_{\min}(G(j\omega)K(j\omega)) \geq 20 \text{ db for } \omega \leq 0.1 \text{ rad/sec}$$

and

$$\sigma_{\min}(G(j\omega)K(j\omega)) \rightarrow \infty \text{ as } \omega \rightarrow 0$$

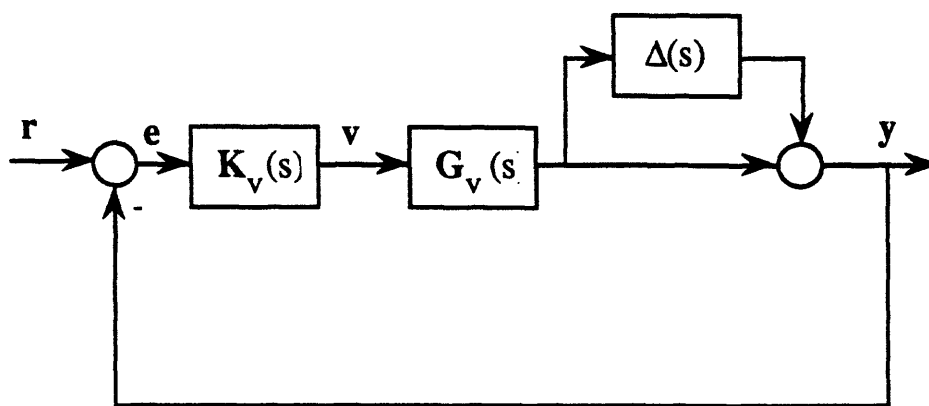


Figure 4.3: Perturbed System

Requirement (b3) constrains the bandwidth of the system and together with requirement (c1) establishes (as it will be explained in section 4.3) a tradeoff between speed of response, phase and gain margins, and saturation magnitude and rate limits. Specifically, requirement (c1) is met if the following condition on

$$\|S(s)\|_{\infty} = \max_{\omega} \left[\sigma_{\max}(S(j\omega)) \right] \text{ is true:}$$

$$\|S(s)\|_{\infty} \leq 1.66 \approx 4.4\text{db}$$

This sufficient condition results from the well known facts [6, 8]:

$$\text{GM}\downarrow \leq \frac{k}{k+1}$$

$$\text{GM}\uparrow \geq \frac{k}{k-1}$$

$$|\text{PM}| \geq 2 \sin^{-1} (1/2k)$$

where

$$k = \|S(s)\|_{\infty}$$

Clearly, by minimizing k we obtain good gain and phase margin properties

Finally, specifications (b4),(c2) also impose constraints on the bandwidth of the system and on the roll off at high frequencies. Specifically, (b4) requires that

$$\sigma_{\max}(C(j\omega)) \leq -20 \text{ db for } \omega > 20 \text{ rad/sec}$$

where $C(s) = (I+G(s)K(s))^{-1} G(s)K(s)$ is the closed loop transfer function. For (c2) it is sufficient, resulting from well known facts on the issue of stability robustness [5, 6], that

$$\sigma_{\max}[C(j\omega)] \delta(\omega) < 1 \quad \text{for all } \omega$$

which yields

$$\sigma_{\max} [C(j\omega)] < \frac{10}{\omega} \quad \text{for all } \omega$$

or, since $\sigma_{\max}[G(j\omega)K(j\omega)] \approx \sigma_{\max}[C(j\omega)]$ for large enough ω , the previous constraint can be restated as:

$$\sigma_{\max} [G(j\omega)K(j\omega)] < \frac{10}{\omega}$$

4.3 Design of the LQG/LTR Compensator

4.3.1 Introduction

The LQG/LTR design methodology is briefly summarized in the following subsection . A detailed treatment of this method is given in [1, 2] where the design philosophy and the underlying ideas are fully analyzed.

4.3.2 Summary of the LQG/LTR Methodology

Let the design plant model be given by:

$$\mathbf{x}(t) = \mathbf{A}\mathbf{x}(t) + \mathbf{B}\mathbf{u}(t) \quad (4.3.1a)$$

$$\mathbf{y}(t) = \mathbf{C}\mathbf{x}(t) \quad (4.3.1b)$$

with $\mathbf{A} \in \mathbb{R}^{n \times n}$, $\mathbf{B} \in \mathbb{R}^{m \times m}$, $\mathbf{C} \in \mathbb{R}^{m \times n}$.

The LQG/LTR compensator is given by:

$$\mathbf{K}(s) = \mathbf{G}(s\mathbf{I} - \mathbf{A} + \mathbf{B}\mathbf{G} + \mathbf{H}\mathbf{C})^{-1} \mathbf{H} \quad (4.3.2)$$

where \mathbf{G} , \mathbf{H} are $(m \times n)$ and $(n \times m)$ gain matrices given by

$$\mathbf{G} = \frac{1}{\rho} \mathbf{B}^T \mathbf{K} \quad (4.3.3)$$

$$\mathbf{H} = \frac{1}{\mu} \Sigma \mathbf{C}^T \quad (4.3.4)$$

where \mathbf{K} , Σ solutions of the following Riccati equations.

Control Algebraic Riccati Equation (CARE):

$$\mathbf{A}^T \mathbf{K} + \mathbf{K} \mathbf{A} + \mathbf{C}^T \mathbf{C} - \frac{1}{\rho} \mathbf{K} \mathbf{B} \mathbf{B}^T \mathbf{K} = \mathbf{0} \quad (4.3.5)$$

and

Filter Algebraic Riccati Equation (FARE):

$$\mathbf{A} \boldsymbol{\Sigma} + \boldsymbol{\Sigma} \mathbf{A}^T + \mathbf{L} \mathbf{L}^T - \frac{1}{\mu} \boldsymbol{\Sigma} \mathbf{C}^T \mathbf{C} \boldsymbol{\Sigma} = \mathbf{0} \quad (4.3.6)$$

with $\mathbf{L} \in \mathbb{R}^{n \times m}$, $\mu > 0$, $\rho > 0$ appropriately chosen design parameters so that the closed loop system (figure. 4.4) meets the design specifications. The selection of the design parameters is performed as follows:

Step 1: Choose \mathbf{L} , μ so that the target feedback loop (TFL) depicted in figure (4.5) meets (in terms of loop shapes and locations of closed loop poles) the specifications posed on the design (section 4.2). The relationship between the design parameters \mathbf{L} , μ and the target loop shapes resulting by specifying \mathbf{H} via (4.3.6) and (4.3.4), can be seen in the so-called Kalman Frequency Domain Equality (KFDE)

$$\sigma_i(\mathbf{I} + \mathbf{C} \boldsymbol{\Phi}(j\omega) \mathbf{H}) = \sqrt{1 + \frac{1}{\mu} \sigma_i^2(\mathbf{C} \boldsymbol{\Phi}(j\omega) \mathbf{L})} \quad (4.3.7)$$

where $\Phi(s) = (sI - A)^{-1}$

The KFDE allows the designer to shape the loop transfer function $C\Phi(s)H$ by choosing L and μ .

Step 2: Once L, μ are chosen in Step 1 then, by selecting ρ small enough and specifying G via (4.3.5) and (4.3.3), the target loop transfer function $C\Phi(s)H$ is recovered by $G(s)K(s)$, provided that $G(s)$ does not have any nonminimum phase zeros.

i.e. if $\det(G(s)) \neq 0$ for every s in RHP then

$$G(s)K(s) \rightarrow C\Phi(s)H \text{ as } \rho \rightarrow 0 \quad (4.3.8)$$

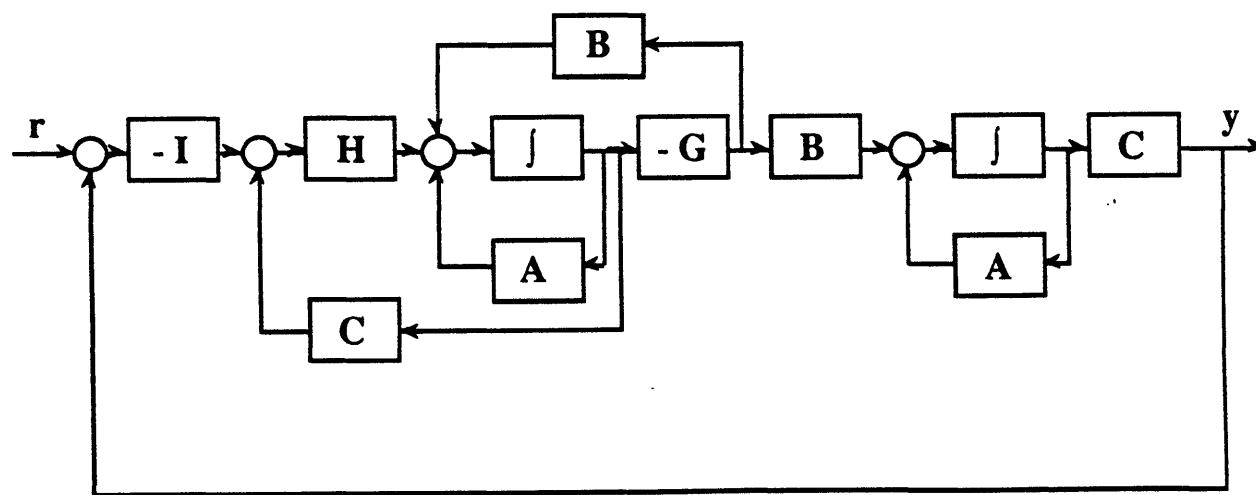


Figure 4.4: LQG/LTR Compensator with the Model of the System in a Closed Loop Configuration

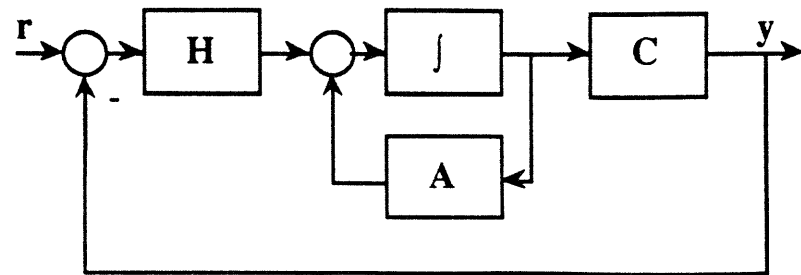


Figure 4.5: Target Feedback Loop

The two-step procedure highlighted so far results in a closed loop system the eigenvalues of which are the eigenvalues of $[A-BG]$ and $[A-HC]$. These, by construction, are all stable. Thus, nominal stability is automatically guaranteed. Also, the loop shapes of the actual feedback loop in figure 4.4, depending on how small ρ is, will be almost the same with the corresponding ones in the TFL (figure 4.5). Furthermore, the stability margins will be almost identical as $\rho \rightarrow 0$. In fact, since the TFL is a Kalman filter loop it has guaranteed $[1/2, \infty)$ gain and ± 60 deg phase margins at the plant output. Hence, as $\rho \rightarrow 0$ the actual loop would enjoy the same margins.

However, when doing step 1 no information on the size of the required control u is available. Therefore, the designer has to make sure that after the recovery (step2), the resulting system would not require excessive control action. If the system asks for unrealistic control inputs, then the designer has to redesign the TFL (step 1) by sufficiently reducing its bandwidth, so that the new design (step 2) respects the constraints on the control inputs.

4.3.3 Application of the LQG/LTR Design Methodology to the F18/HARV

As stated in the beginning of section 4.2, the compensator design will be based on the pseudosystem $G_v(s) = C(sI-A)^{-1} B_v$. In this section, the design sequence for an LQG/LTR compensator for the operating point 1 is illustrated and discussed. For operating points 2 and 3 the designs are very briefly presented since the key points remain essentially the same.

4.3.3.1: Dynamic Augmentation and the Target Loop Design

Since the specifications (b2) ask for zero steady state error to constant commands or disturbances and $G_v(s)$ does not possess any poles at the origin, an integrator is needed for each channel without any feedback around it. The augmentation procedure with integrators [1] is accomplished as follows:

Step 1: Augment plant $G_v(s)$ by adding integrators in each input channel (figure 4.6(a)).

Step 2: Design LQG/LTR compensator using the augmented plant (design plant) $G_a(s) = G_v(s)I/s$ that meets the specifications.

Step 3: Absorb the integrators in the LQG/LTR compensator found in Step 2 (Fig. 4.6.(b)).

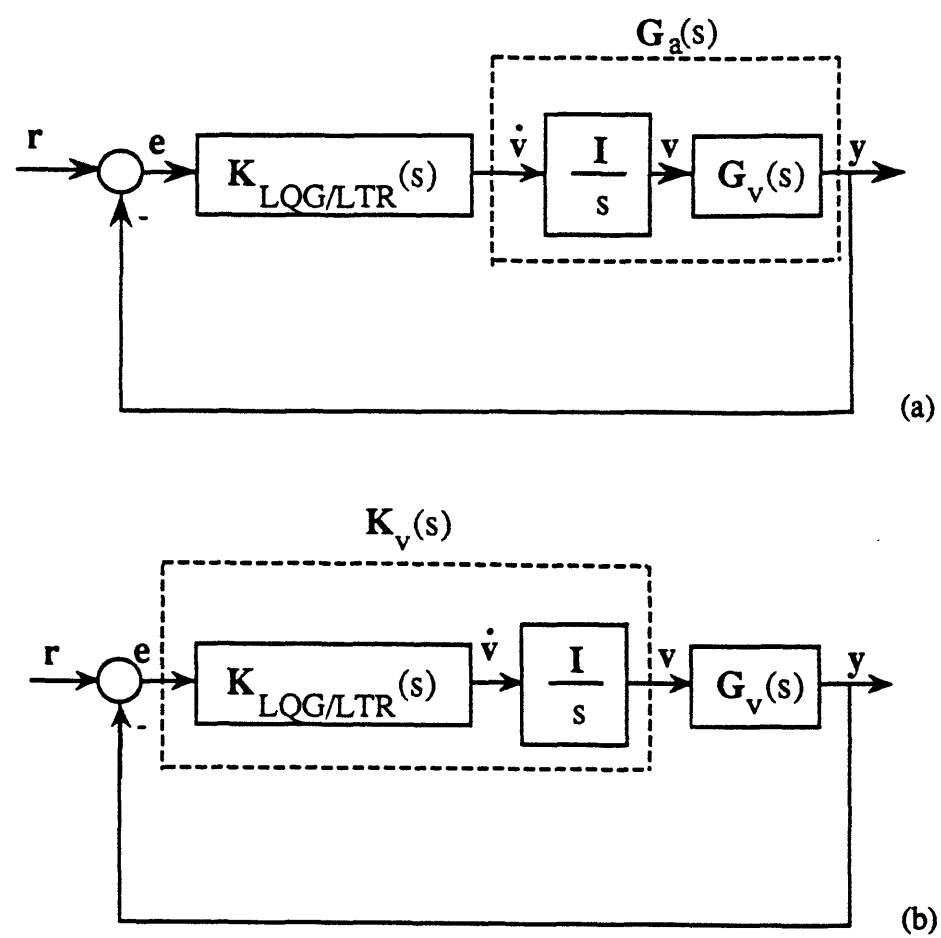


Figure 4.6: Augmentation with Integrators

Augmentation with integrators at the plant input offers extra freedom to the designer to do loop shaping and also contributes to the high frequency roll-off which is desirable for noise attenuation and robust stability in the presence of high frequency modeling errors.

This extra freedom can be used to match the loop singular values at low and/or high frequencies as well as at all frequencies [1]. To view this, one has to consider the

augmented system (figure 4.6.a) the state space description of which is given by:

$$\dot{\mathbf{x}}_a(t) = \mathbf{A}_a \mathbf{x}_a(t) + \mathbf{B}_a \mathbf{u}_a(t) \quad (4.3.9a)$$

$$\mathbf{y}_a(t) = \mathbf{C}_a \mathbf{x}_a(t) \quad (4.3.9b)$$

with

$$\mathbf{A}_a = \begin{bmatrix} \mathbf{0} & \mathbf{0} \\ \mathbf{B}_v & \mathbf{A} \end{bmatrix}, \quad \mathbf{B}_a = \begin{bmatrix} \mathbf{I} \\ \mathbf{0} \end{bmatrix}, \quad \mathbf{C}_a = [\mathbf{0} \quad \mathbf{C}]$$

$$\mathbf{x}_a(t) = \begin{bmatrix} \mathbf{v}(t) \\ \mathbf{x}(t) \end{bmatrix}, \quad \mathbf{u}_a(t) = \mathbf{v}(t), \quad \mathbf{y}_a(t) = \mathbf{y}(t)$$

Partitioning the design parameter matrix \mathbf{L} as:

$$\mathbf{L} = \begin{bmatrix} \mathbf{L}_1 \\ \mathbf{L}_h \end{bmatrix} \quad (4.3.10)$$

and selecting:

$$\mathbf{L}_1 = \mathbf{C}(-\mathbf{A})^{-1} \mathbf{B}_v \quad (4.3.11)$$

$$\mathbf{L}_h = (-\mathbf{A})^{-1} \mathbf{B}_v \mathbf{L}_1 \quad (4.3.12)$$

it can be easily verified that:

$$C_a \Phi_a(s) L = \frac{I}{s} \quad (4.3.13)$$

with

$$\Phi_a(s) = (sI - A_a)^{-1} \quad (4.3.14)$$

As it can be noticed in (4.3.13), with the choice of L as above, the shaping transfer function $C\Phi_a(s)L$ is like an integrator. This implies that $\sigma_1(C\Phi_a(j\omega)L)=1$ for all ω

The Kalman frequency domain equality (4.3.6) yields:

$$\sigma_1(I + C_a \Phi_a(j\omega)H) = \sqrt{1 + \frac{1}{\mu} \frac{1}{\omega^2}}$$

which for sufficiently small μ , yields

$$\sigma_1(I + C_a \Phi_a(j\omega)H) \approx \frac{1}{\omega\sqrt{\mu}}, \quad \text{for all } \omega \quad (4.3.15)$$

Sufficiently small μ is problem dependent. For μ not sufficiently small, still perfect matching at low and high frequencies is obtained but not necessarily at the medium frequency range.

The procedure of matching singular values in the whole frequency gives rise to some interesting discussion concerning its applicability to unstable plants, since with this particular choice of L the stabilizability assumption on the Kalman Filtering problem implied by (4.3.6) is violated. As it is concluded in the Appendix (A1) the procedure is

still applicable with no generic additional constraints. This is also verified from the design at operating point 1 where the aircraft is unstable.

Integrators do not add any zeros in the augmented system and thus since $G_v(s)$ does not have any RHP zeros, recovery is guaranteed. The augmented system's singular values are shown in figure 4.7.

The technique of matching singular values in the whole frequency range was employed. Figure 4.8 shows the singular values $\sigma_i[C_a\Phi_a(j\omega)L]$ of the shaping transfer function $C_a\Phi_a(s)L$. The parameter μ , which controls the bandwidth of the target loop, was chosen $\mu=1/3^2 = .111$ (thus asking for a target loop crossover at ≈ 3 rad/sec.).

Figure 4.9 shows the resulting singular values $\sigma_i[C_a(j\omega I - A_a)^{-1}H]$ of the target loop. As expected, the singular values are matched for all frequencies. Figure 4.10 shows the singular values of the target loop sensitivity transfer function which verifies the $(1/2, \infty)$ and ± 60 deg gain and phase margin properties of the target loop.

Clearly, the target loop meets all the frequency domain specifications with the exception of the noise attenuation specification. The violation of this specification (at 20 rad/sec) is seen to be harmless because after recovery we will roll-off before the noise barrier.

The target loop $G_T(s)$ as well as the target closed loop $C_T(s)$ poles and zeros are shown in Table 4.1. It is interesting to note that, with the specific selection of L , the zeros of the target loop are on top of the stable poles of $G_v(s)$ and on top of the stable mirror image of the unstable poles of $G_v(s)$. This is expected since the target loop singular values look like an integrator. The slow complex poles of the target loop are approximately cancelled by the target closed loop zeros (which of course are the same with the zeros of $G_T(s)$). Hence, these slow poles are not going to appear in the output response.

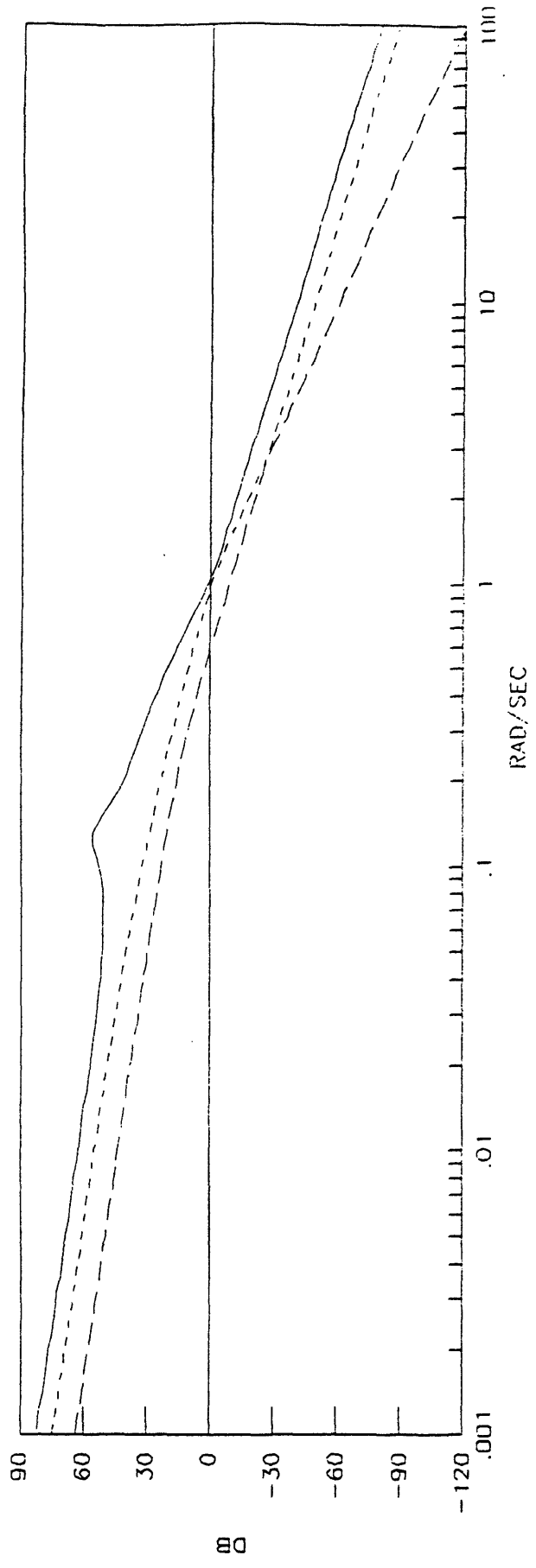


Figure 4.7 : Singular values of the augmented system $G_a(s) = I/sG_v(s)$

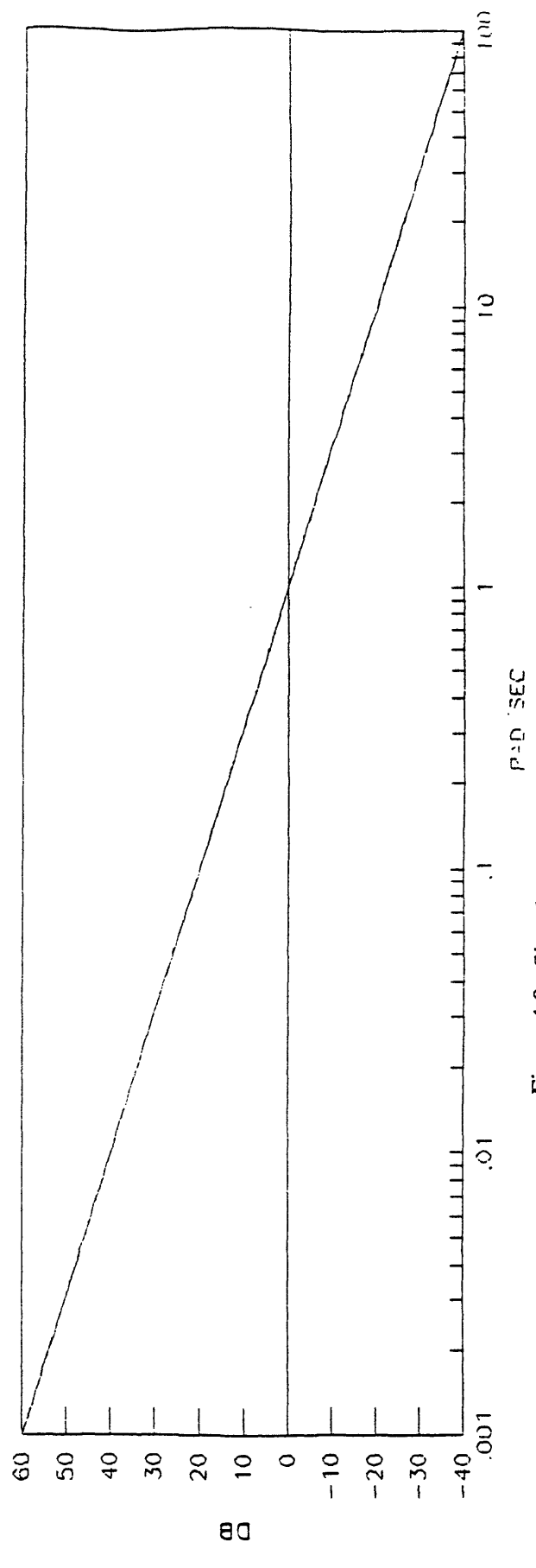


Figure 4.8 : Singular values of the shaping transfer function $C_a(sI-A_a)^{-1}L$

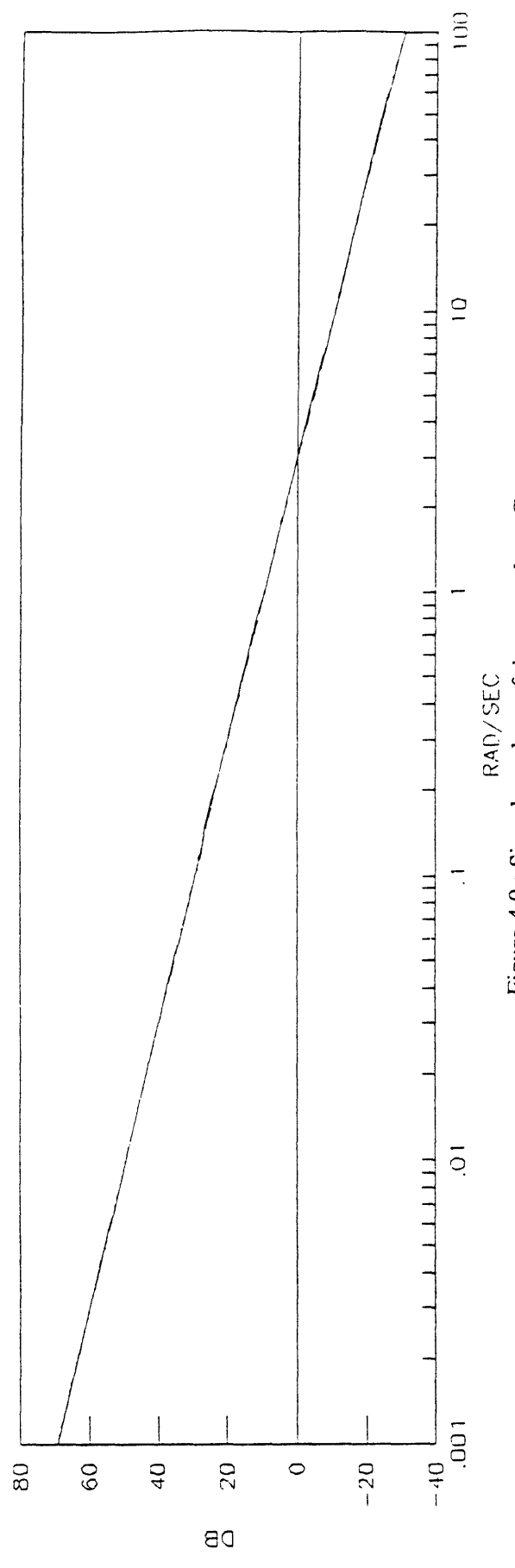


Figure 4.9 : Singular values of the target loop $G_T(s)$

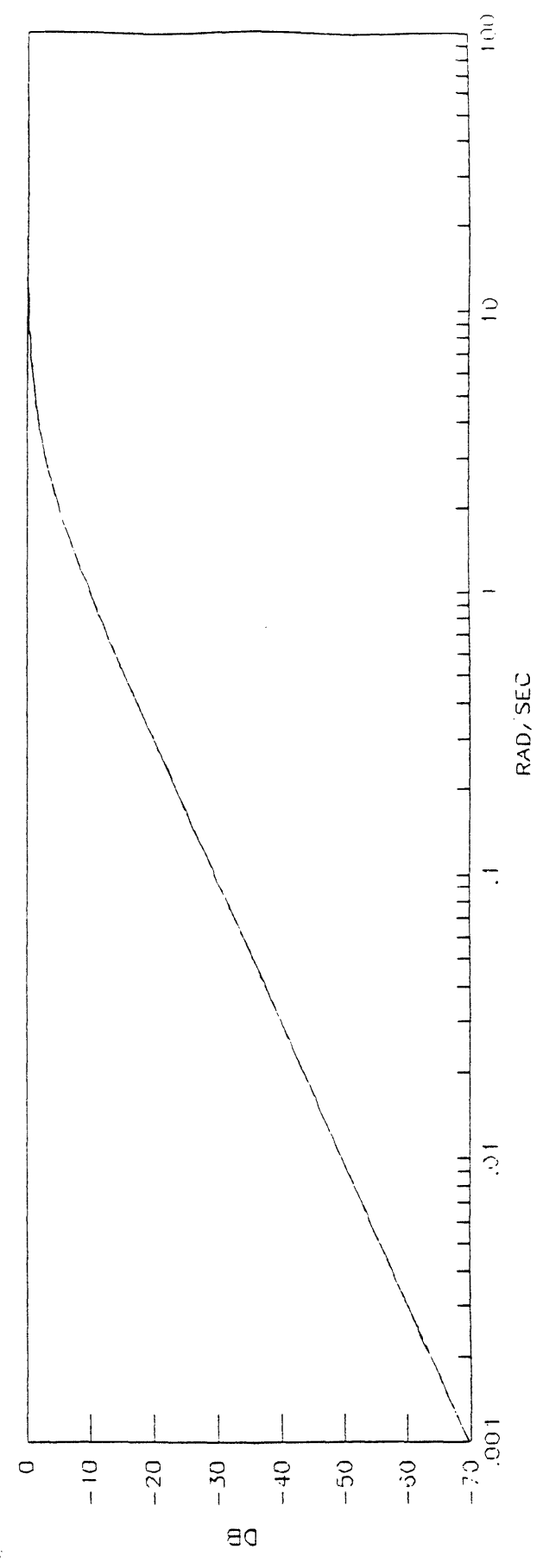


Figure 4.10 : Singular values of the target loop sensitivity $(1+G_T(s))^{-1}$

Table 4.1
Poles and zeros of the target loop $G_T(s)$ and target closed loop $C_T(s)$

$G_T(s)$		$C_T(s)$	
Poles	Zeros	Poles	Zeros
$.0188 \pm .1280j$	$-.0188 \pm .1280j$	$-.0188 \pm .1280j$	$-.0188 \pm .1280j$
$-.2481 \pm .3585j$	$-.2481 \pm .3585j$	$-.2481 \pm .3585j$	$-.2481 \pm .3585j$
0		-3	
0		-3	
0		-3	

4.3.3.2: Resulting Feedback Loop Design

The target loop was sufficiently recovered by the transfer function $G_a(s)K_{LQG}/LTR(s)$ so that the specifications are met. In particular, the value of the recovery parameter ρ used, was $\rho=0.001$. The resulting singular values $\sigma_i[G_a(j\omega)K_{LQG}/LTR(j\omega)]$ and $\sigma_i[(I+G_a(j\omega)K_{LQG}/LTR(j\omega))^{-1}]$ of the loop and of the sensitivity transfer function are shown in figures 4.11, 4.12 respectively.

As it can be verified from these plots, all of the specifications in the frequency domain are met. The loop crossover is approximately at 2 rad/sec and 1 rad/sec for the maximum and minimum singular value respectively, which implies that the settling times should range from approximately $3(1/2)=1.5$ sec upto $3(1/1)=3$ sec.

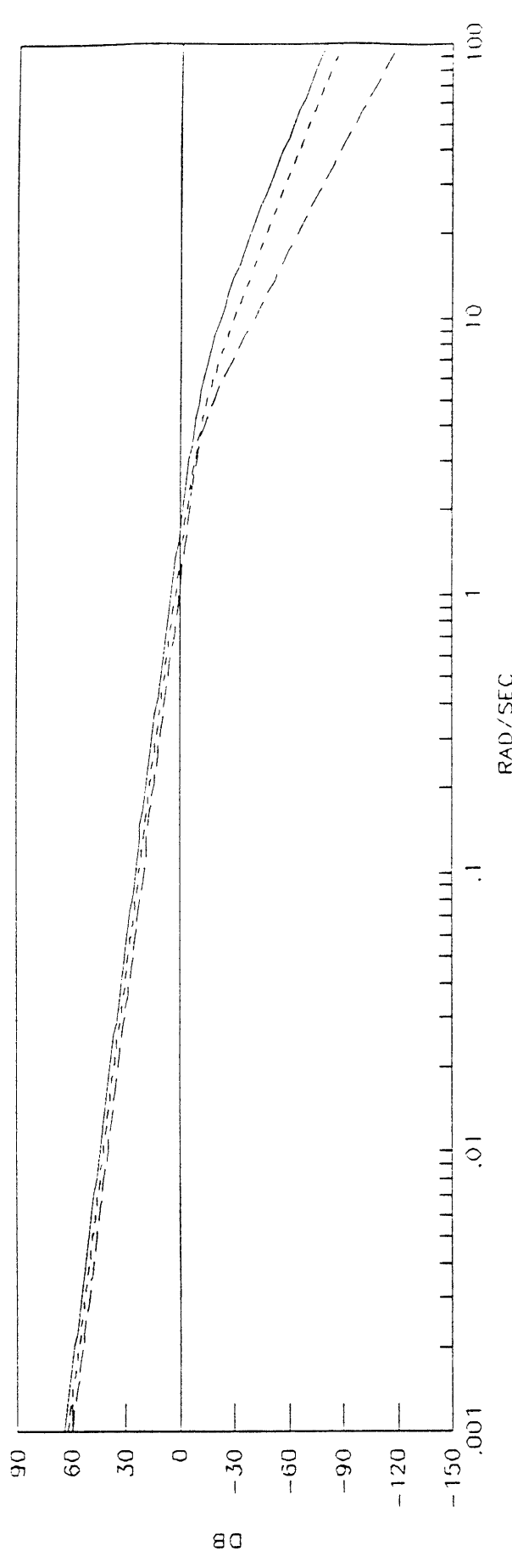


Figure 4.11 : Singular values of the loop $G_a(s)KLQG/LTR(s)$

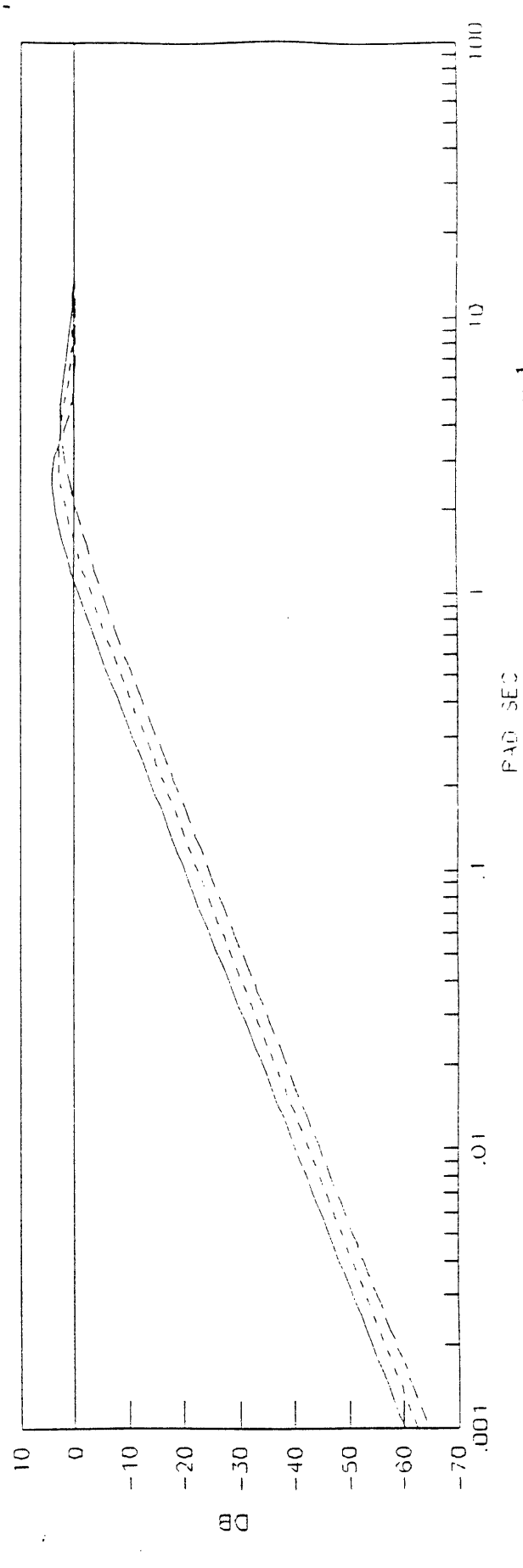


Figure 4.12 : Singular values of the sensitivity $(I+G_a(s)KLQG/LTR(s))^{-1}$

The stability margins can be inferred from the sensitivity singular values by evaluating $\|S(s)\|_{\infty}$.

By inspection $\|S(s)\|_{\infty} = 4 \text{ db}$, which implies

$$\downarrow \text{GM} \leq .61 = -4.29 \text{ db}$$

$$\uparrow \text{GM} \geq 2.7 = 8.66 \text{ db}$$

$$|\text{PM}| \geq 36.8 \text{ deg}$$

Also the -60db/dec roll off of $\sigma_{\max}[G_a(j\omega)K_{\text{LQG/LTR}}(j\omega)]$ guarantees that the system will remain stable for more severe high frequency modeling errors than what the specifications ask.

In particular, stability is guaranteed even for high frequency modeling errors bounded by

$$\delta(\omega) = .001\omega^3 \text{ for } \omega > 1 \text{ rad/sec.}$$

Figure 4.13 shows the singular values $\sigma_i[K_{\text{LQG/LTR}}(j\omega)]$ whereas Figure 4.14 shows the singular values $\sigma_i[(I+K_v(j\omega)G_v(j\omega))^{-1}K_v(j\omega)]$ of the transfer function from reference command r to pseudocontrol v .

The poles and zeros of the augmented system $G_a(s)$, LQG/LTR compensator $K_{\text{LQG/LTR}}(s)$ and closed loop system $C(s)$ are shown in table 4.2. The effect of the slow closed loop poles of the plant output is expected to be small due to the zeros on top of them.

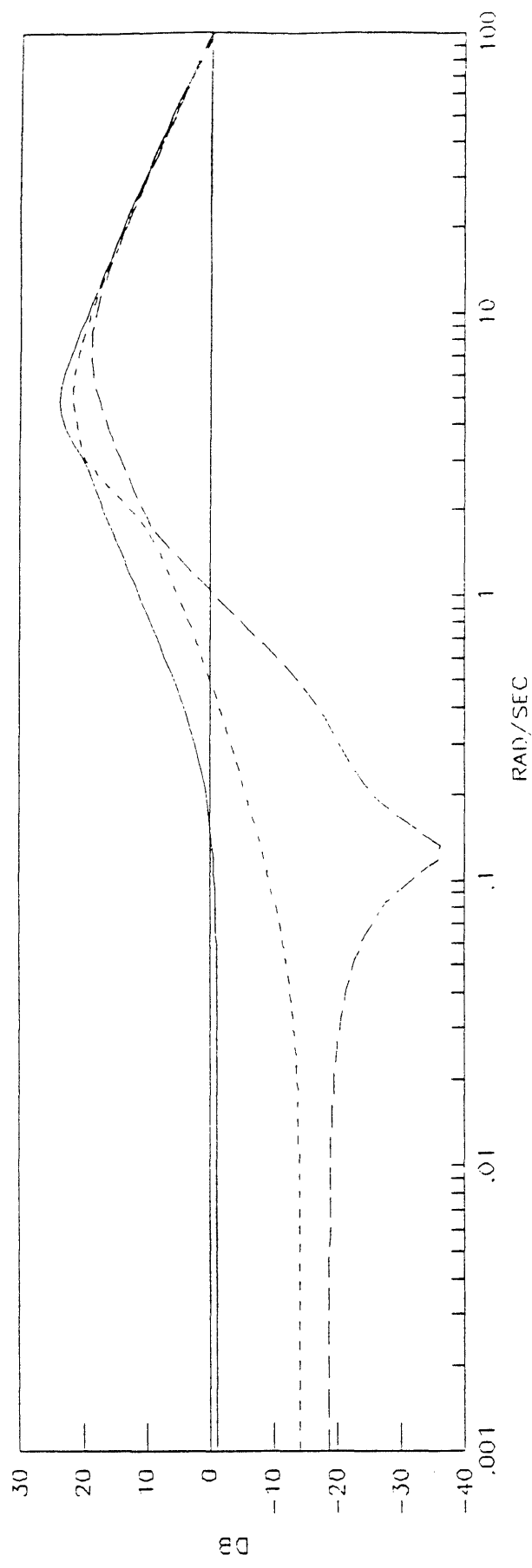


Figure 4.13 : Singular values of $KLQG/LTR(s)$

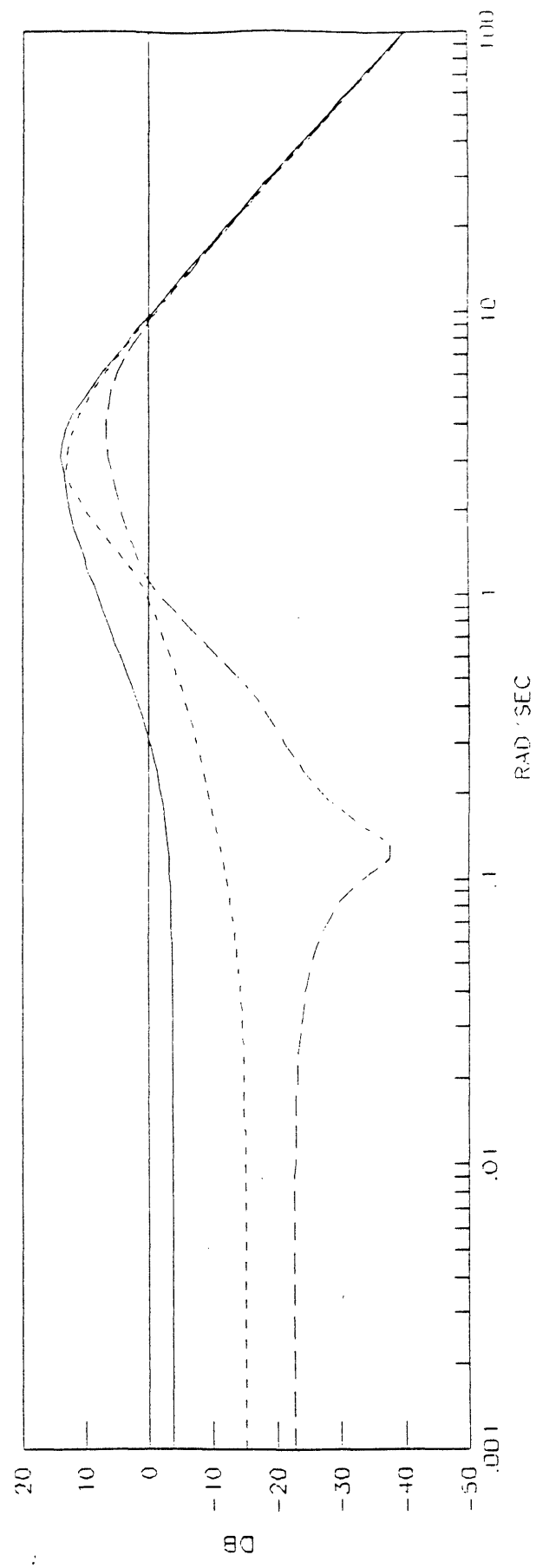


Figure 4.14 : Singular values of $K_y(s)S(s)$

Table 4.2

Poles and zeros of the augmented system, LQG/LTR compensator and closed loop system

$G_a(s)$		$K_{LQG/LTR}(s)$		$C(s)$	
Poles	Zeros	Poles	Zeros	Poles	Zeros
$-.2481 \pm 3585j$	none	$-3.9413 \pm 3.3193j$	$-.2481 \pm 3585j$	$-3.9782 \pm 3.974j$	$-.2481 \pm .3585j$
$.0188 \pm .1280j$		$-5.4949 \pm 5.0654j$	$-.0178 \pm .1244j$	$-2.4364 \pm 2.433j$	$-.0178 \pm .1244j$
0		$-.20471 \pm 3.6789j$		$-1.5752 \pm 2.750j$	
0		-5.2361		$-.2481 \pm .3585j$	
0				$-.0188 \pm .1280j$	
				-3.1481	
				-3.0	
				-3.0	
				-3.0	

4.3.3.3. Time Domain Simulations

The distribution matrix T (chapter 3) was chosen so that the following cost functional is minimized:

$$J = \mathbf{u}^T \mathbf{W} \mathbf{u}$$

with $\mathbf{W} = \text{diag}(1, 1, 1, 1, 5.2, 1)$.

The trailing edge flap was penalized heavier than the rest. This was done because its scaled rate limit is the least (table 4.3). The resulting distribution matrix T is given in Appendix (A2). The overall compensator transfer function is $K_O(s) = T K_V(s) = T I/s K_{LQG/LTR}(s)$.

The resulting output responses to the step commands

- $r_1 = [0 \ 1 \ 0]^T$ vertical translation of 1 deg in γ ,
- $r_2 = [0 \ 0 \ 1]^T$ pitch pointing of 1 deg in θ
- $r_3 = [0 \ 1 \ 1]^T$ direct lift of 1 deg in γ and θ ,
- $r_4 = [0.5 \ 0 \ 0]^T$ horizontal acceleration of 4 ft/sec in V_T ,

are shown in figures 4.15, 4.16, 4.17, 4.18 respectively.

Table 4.3
Scaled Rate Limits for Operating Point 1

control	scaled rate limits
symmetric thrust vectoring δ_{TVS}	$2 \times 60(\text{deg/sec})(1/50) \text{ deg}^{-1} = 3.2 \text{ sec}^{-1}$
symmetric aileron δ_{AS}	$2 \times 100(\text{deg/sec})(1/50) \text{ deg}^{-1} = 4 \text{ sec}^{-1}$
symmetric stabilator δ_{SS}	$2 \times 60(\text{deg/sec})(1/34) \text{ deg}^{-1} = 3.5 \text{ sec}^{-1}$
symmetric leading edge flap δ_{LES}	$2 \times 20(\text{deg/sec})(1/2) \text{ deg}^{-1} = 20 \text{ sec}^{-1}$
symmetric trailing edge flap δ_{TES}	$2 \times 60(\text{deg/sec})(1/60) \text{ deg}^{-1} = 2 \text{ sec}^{-1}$
throttle δ_T	$2 \times 30(\text{deg/sec})(1/27) \text{ deg}^{-1} = 2.2 \text{ sec}^{-1}$

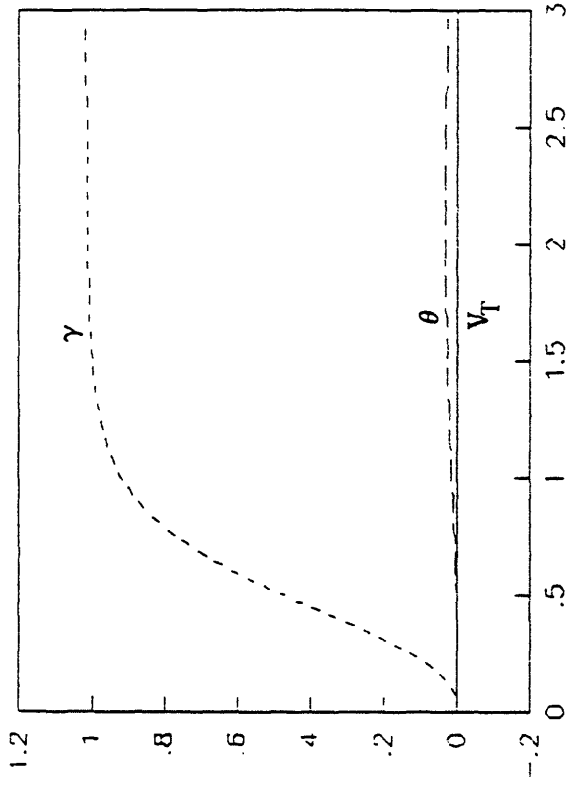


Figure 4.15 : Output response to r1

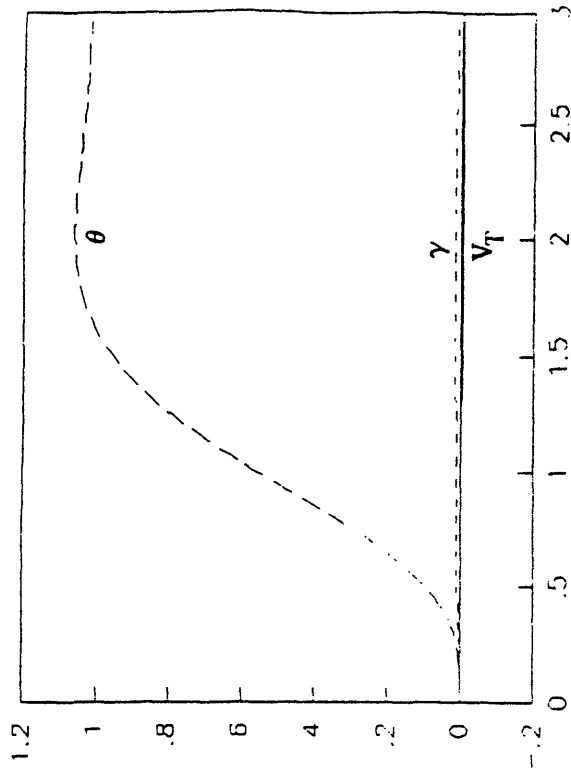


Figure 4.16 : Output response to r2

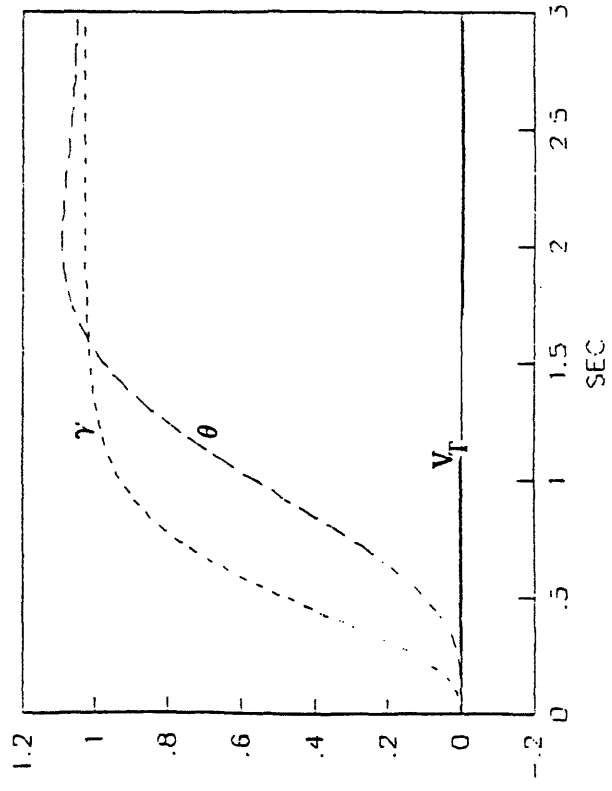


Figure 4.17 : Output response to r3

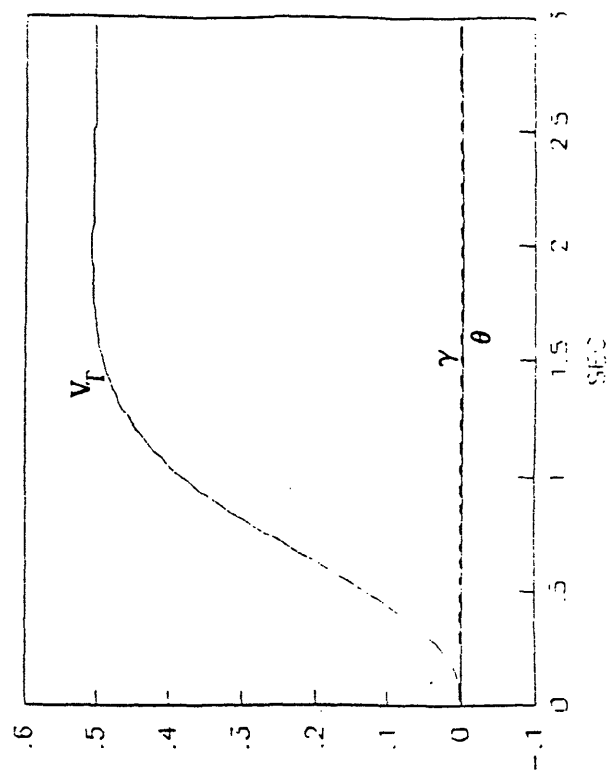


Figure 4.18 : Output response to r4

In figures 4.19, 4.20, 4.21, 4.22 the required pseudoinputs are shown while figures 4.23, 4.24, 4.25, 4.26 illustrate what the actual inputs should be.

Referring to the figures illustrating the actual controls, the following notational convention was adopted throughout the remainder of the thesis:

- 1 refers to the symmetric thrust vectoring vane deflection in scaled units
- 2 refers to the symmetric aileron in scaled units
- 3 refers to the symmetric stabilator in scaled units
- 4 refers to the symmetric leading edge flap in scaled units
- 5 refers to the symmetric trailing edge flap in scaled units
- 6 refers to the throttle deflection in scaled units

As it can be verified, the output tracks the reference input with zero steady state error, negligible overshoots and with settling time in the range from 1.5 to 3 sec. Both saturation magnitude and rate limits are respected in every case.

During the vertical translation maneuver (figure 4.23) the aileron (2), stabilator (3), trailing edge flap (5), and the throttle (6) produce extra amount of lift that will force the aircraft to a climbing flight. Also, at the same time the thrust vectoring vane (1) is deflected upwards so that the speed V_T is prevented from decreasing and the pitch angle θ is maintained constant.

For this particular operating condition the speed of the aircraft is low and therefore extra lift is hard to be generated. This is the reason for the relatively large deflections of the aileron and of the trailing edge flap that mainly produce this extra lift.

The pitch pointing maneuver is essentially an effortless one as illustrated in Figure

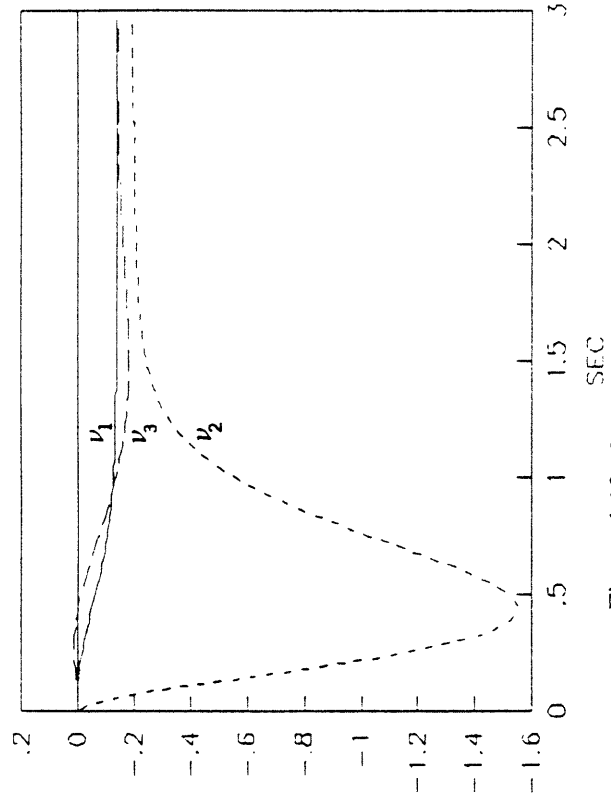


Figure 4.19 : Pseudocontrol response to r_1

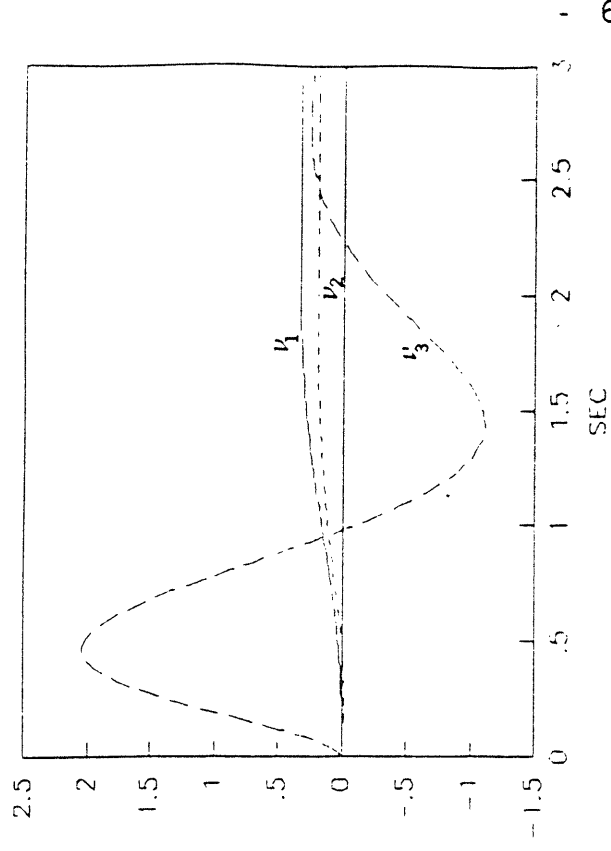


Figure 4.20 : Pseudocontrol response to r_2

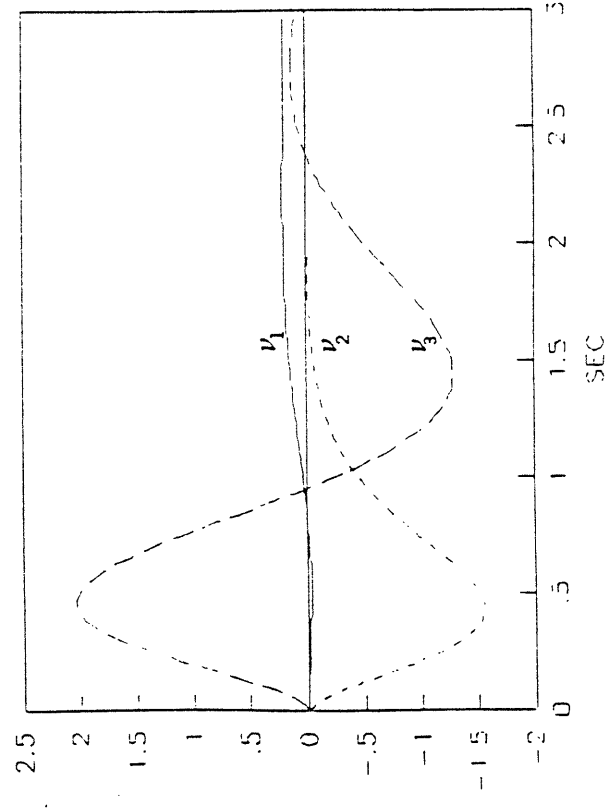


Figure 4.21 : Pseudocontrol response to r_3

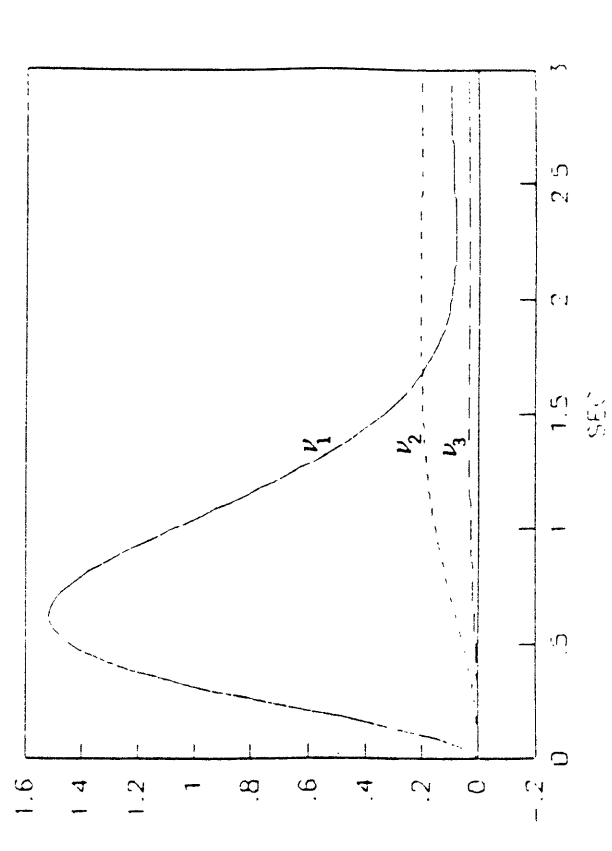


Figure 4.22 : Pseudocontrol response to r_4

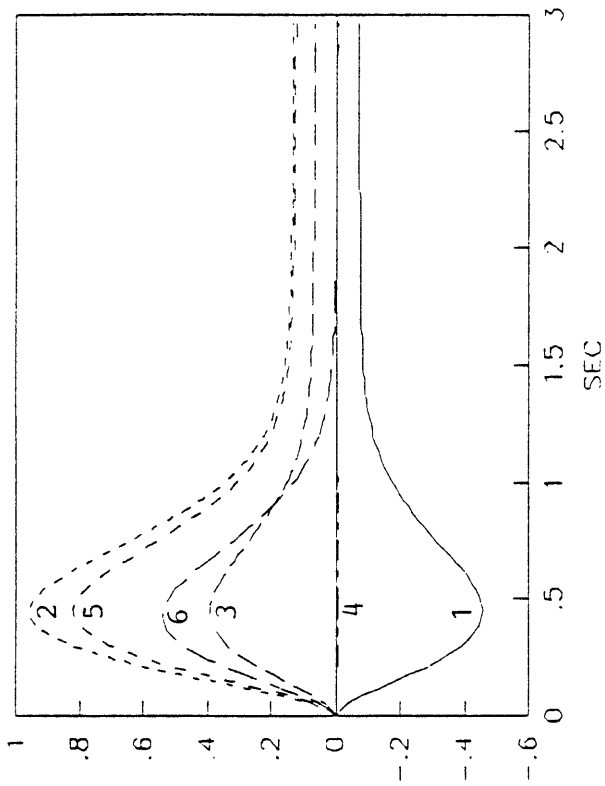


Figure 4.23.: Control response to r1

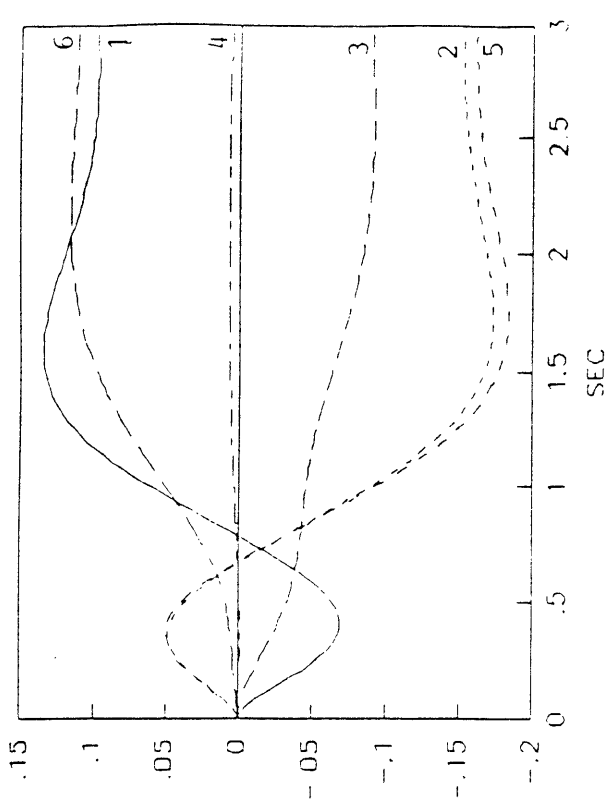


Figure 4.24 : Control response to r2

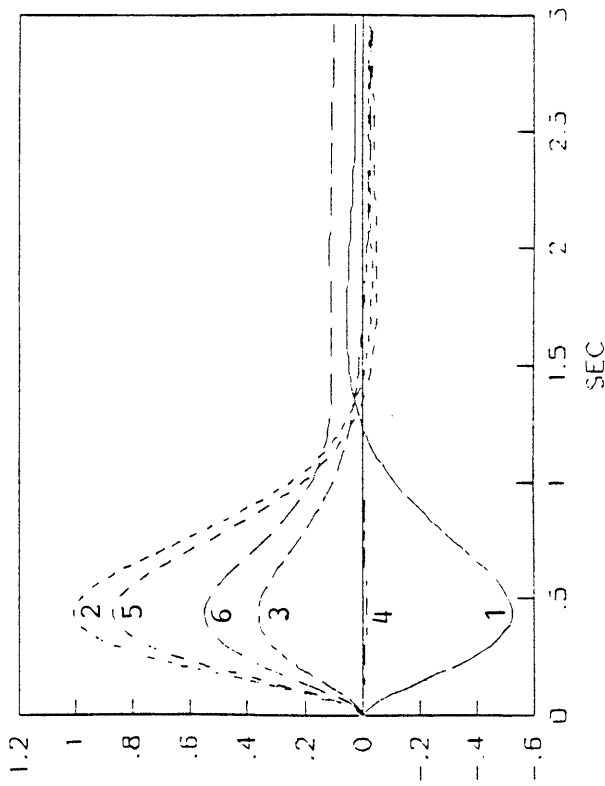


Figure 4.25 : Control response to r3

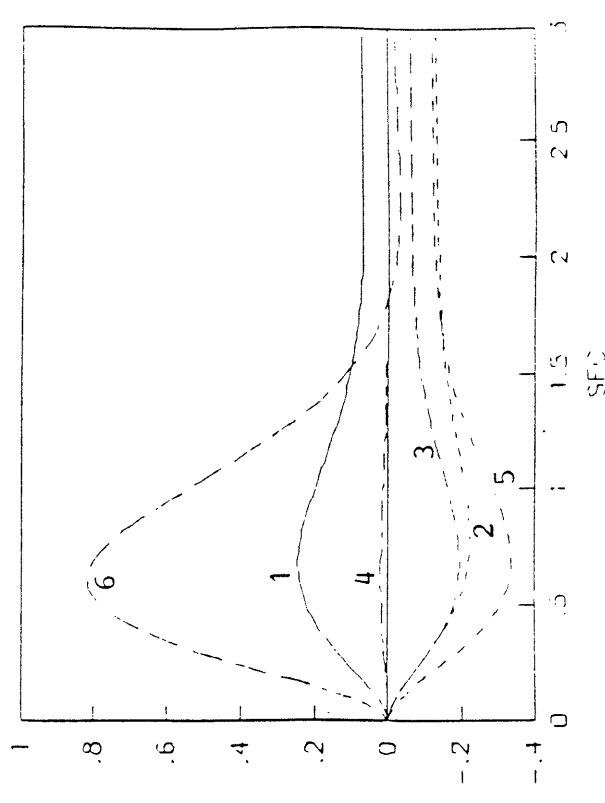


Figure 4.26 : Control response to r4

4.24. The stabilator as well as the thrust vectoring vane are deflected upwards to produce an increasing θ pitching moment. This is initially balanced by a decreasing θ pitching moment produced by downward deflections of the aileron and the trailing edge flap. As time goes on, decreasing θ pitching moments are produced by the downwards deflections of the thrust vectoring vane which are counterbalanced by upward deflections of aileron and trailing edge flap.

The direct lift maneuver is the sum of the previously discussed maneuvers. Initially, the controls act essentially as in the vertical translation mode and later on after (1.2 sec) as in the pitch pointing mode.

Finally, during the horizontal acceleration, the throttle is mainly used to produce extra thrust that will accelerate the vehicle. At the same time, the thrust vectoring vane is deflected downwards and in coordination with the upwards deflection of the stabilator maintain constant θ , while the aileron and the trailing edge flap deflect upwards to produce less lift so that γ is kept constant.

For larger step commands the controls, depending on the direction of the reference input, may saturate. Saturation can cause instability. A partial solution to the problem is achieved by pre-smoothing the reference inputs, r (something that is always done) by passing them through smoothing filters before entering the feedback loop (figure 4.27). Doing so removes unwanted frequencies from the reference commands. Obviously, this "extra baggage" does not alter the stability and performance characteristics of the feedback loop design since the filter is out of the feedback loop. This solution is partial because one can not introduce shaping filters to pre-smooth disturbances from nature.

However, a recently developed methodology [10] provides a very intelligent way to handle saturating nonlinearities which guarantees stability and degrades the performance

minimally. Therefore, saturation seems not to be a problem any more as long as the system one is dealing with is linear.

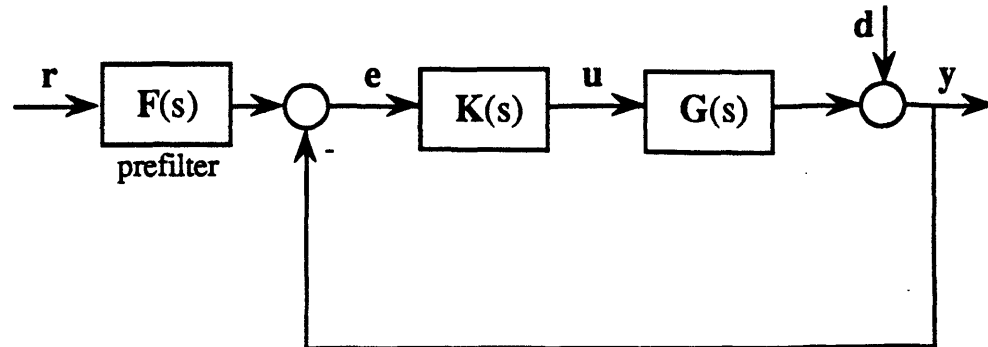


Figure 4.27: Control system with prefilter in the reference command channel

4.3.3.4 Design Tradeoffs

In the previous LQG/LTR design the target loop was recovered to such a degree that all specifications were met. The parameter ρ was not further decreased, and therefore recovery was not perfect. Had this been done, the resulting controls would have been severely saturating, both in magnitude and rate, even for the relatively small commands considered in the previous section. This resulted in phase and gain margins which met the specifications, but which fell short of those guaranteed by the target loop. If the specifications on the phase and gain margins were more demanding, then one would have to redesign the target loop asking for a slower bandwidth that would presumably limit the control action within the saturation levels, and recover more until the stability margin

requirement is met. If we were to do this, however, the resulting design would be very slow thus defeating the main purpose of the fighter aircraft.

It should be noted that the basic limitations for "fully" recovering and thus "achieving" the stability margins of the target loop, are the rate limits on the controls. If one abandons the constraints on the rate limits, the design can achieve better stability margins with a slight degradation in performance (the response being somewhat more sluggish).

The above comments were verified by performing a second design. In particular, the target loop design had a crossover at 1.8 rad/sec. (figure 4.28). The recovery was almost full up to approximately a decade beyond the loop crossover (figure 4.29). The value of ρ used was $\rho=10^{-6}$

The resulting sensitivity singular value plot is shown in figure 4.30. As it can be noticed, $\|S(s)\|_{\infty} \approx 2$ db which results in the following stability margins:

$$\uparrow GM \geq 14 \text{ db}$$

$$\downarrow GM \leq -5 \text{ db}$$

$$|PM| \geq 47 \text{ deg}$$

Clearly, the design meets the specifications in the frequency domain. The compensator singular values $\sigma_i[K_{LQG}/LTR(j\omega)]$ are shown in figure 4.31 and the singular values of the transfer function from r to v $\sigma_i[(I+K_{LQG}/LTR(j\omega)G_a(j\omega))^{-1}K_{LQG}/LTR(j\omega)]$ are shown in figure 4.39.

The response to a 1 degree in γ vertical translation command is shown in figure 4.33 and the control action needed to accommodate this maneuver is shown in figure 4.34. As it can be immediately observed, the control action, although acceptable, in magnitude is very impulsive.

Compared to the previous design, this design has better stability margins at the expense of much faster control action. This can also be seen by comparing the corresponding compensator, as well as, the r to v transfer functions. The second design exhibits more lead. The roll off is started at higher frequencies due to the fact that the fast poles are pushed more to the left. It is this lead that gives good stability margins and in order to push the margins more, one needs more of it. It is this lead also that results in very fast control action. In fact, if ρ is pushed more and more towards zero, the transfer functions $K_{LQG/LTR}(s)$ and $(I+K_{LQG/LTR}(s)G_a(s))^{-1}K_{LQG/LTR}(s)$ tend to become improper. Moreover their high frequency slopes corresponding to the maximum singular values are 40 db/dec and 20 db/dec respectively. This implies that the response of the controls to step commands tends to become more impulsive.

The response of the output is more damped and therefore more sluggish. (compare the 1.5 sec required for γ to achieve 95% of the command in the second design to the 1.1 sec in the first design).

Clearly, there is a tradeoff between stability margins versus rate (and to a lesser degree magnitude) saturation limits and speed of response. If fast response as well as stringent stability margins are required, then the actuators should be able to produce high rates.

In this thesis the compensator designs employed were such that the magnitude as well as the rate saturation limits are respected when applying the relatively small size commands discussed previously. Although, as pointed in 4.3.3.3, saturation does not seem to be a problem in the linear time invariant world, our intention was to avoid exaggerations since the system we are dealing with is a simplified linear model of a nonlinear system. Furthermore, the stability margins obtained using this line of thought are still respectable and meet the specifications.

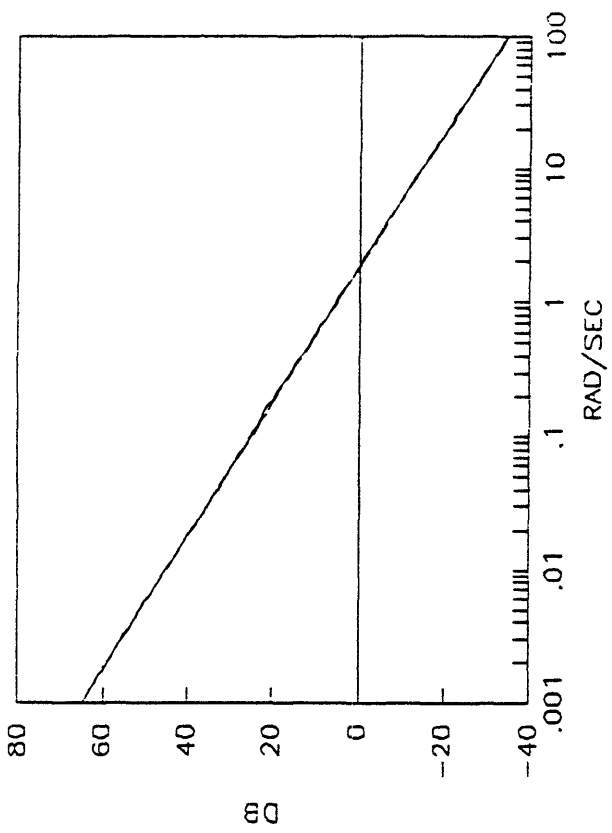


Figure 4.28 : Singular values of the target loop tfm

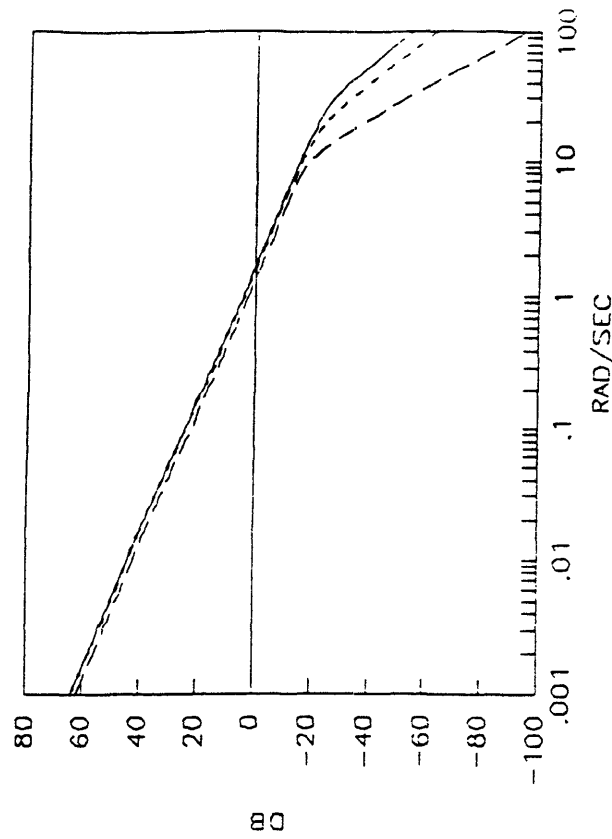


Figure 4.29 : Singular values of the loop tfm

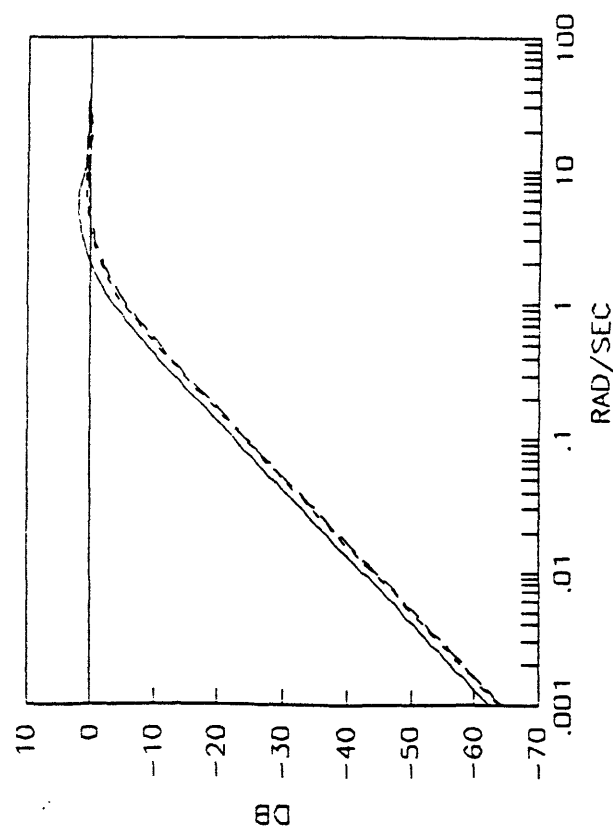


Figure 4.30 : Singular values of the sensitivity tfm

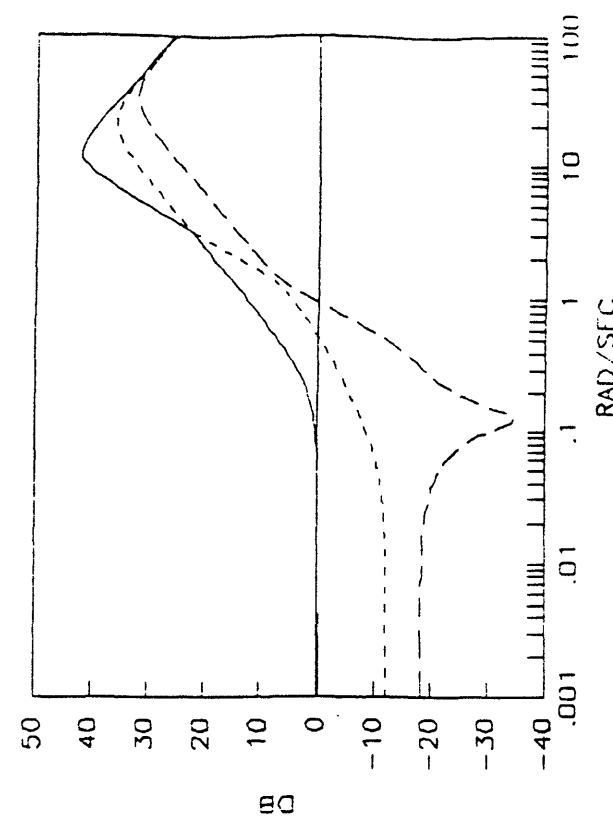


Figure 4.31 : Singular values of the LQG/LTR compensator

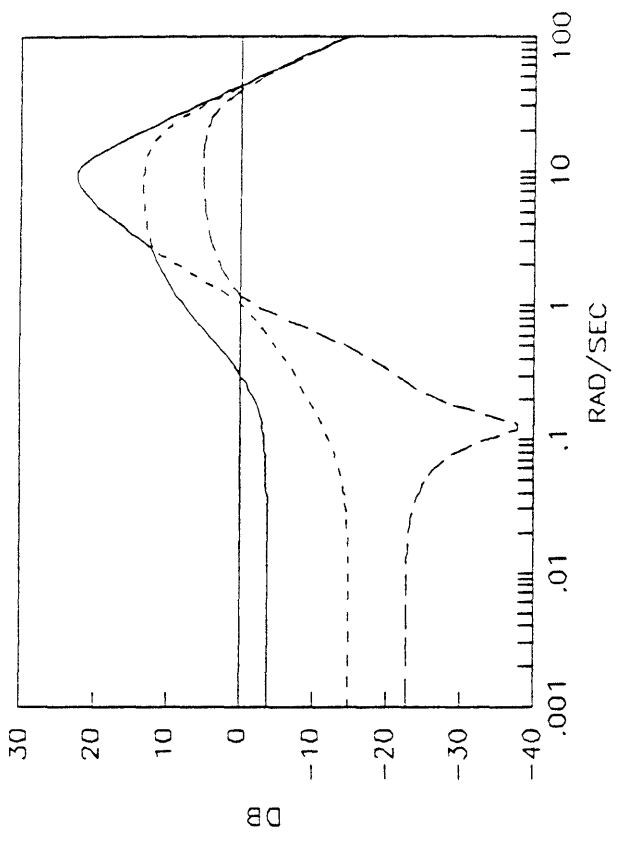


Figure 4.32 : Singular values of the r to v tfm

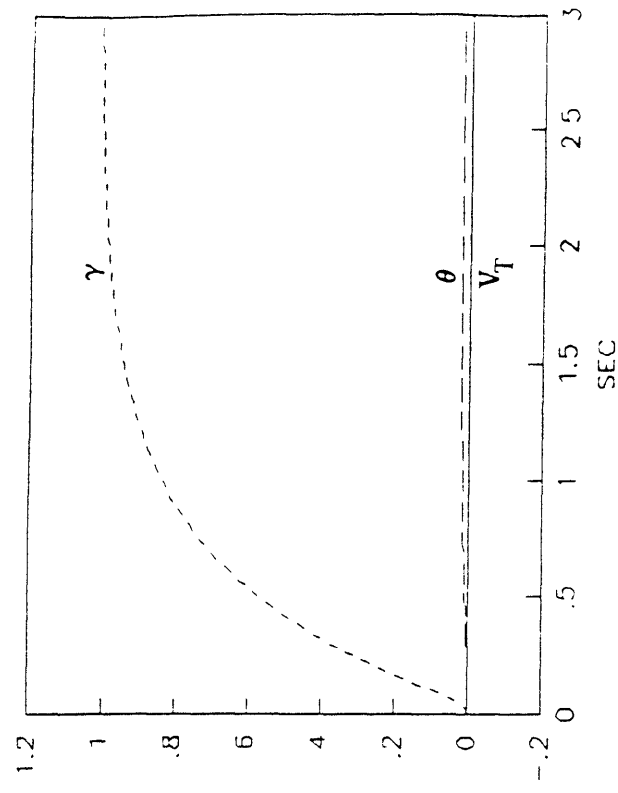


Figure 4.33 : Outputs response to r_1

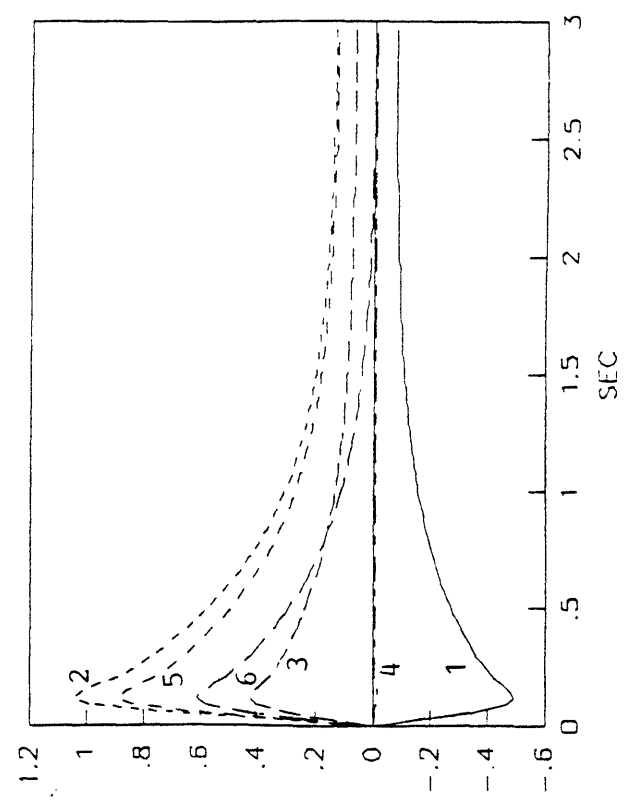


Figure 4.34 : Control response to r_1

4.3.3.5 Operating Points 2 and 3

The LQG/LTR compensator design procedure for operating points 2, 3 follows the same steps as the design sequel for operating point 1.

The resulting loop shapes are shown in Figures 4.35, 4.36 and 4.37, 4.38 respectively.

The frequency domain specifications are met as it can be verified from the plots. Higher bandwidth than operating point 1 can be afforded. In particular, the crossover frequency is approximately 2.2 rad/sec and 3 rad/sec for point 2 and 3 respectively.

The time simulations for

$$r_1 = [0 \ 1 \ 0]^T \text{ vertical translation 1 deg in } \gamma$$

$$r_2 = [0 \ 0 \ 1]^T \text{ pitch pointing 1 deg in } \theta$$

are shown in figures 4.39 through 4.46.

Clearly, the response of the outputs is faster than in operating point 1. Saturation limits are respected. As it can be noticed from figures 4.40, 4.42, 4.44, 4.46, the role of thrust vectoring is not important. The numerical values of the gains are given in Appendix (A2).

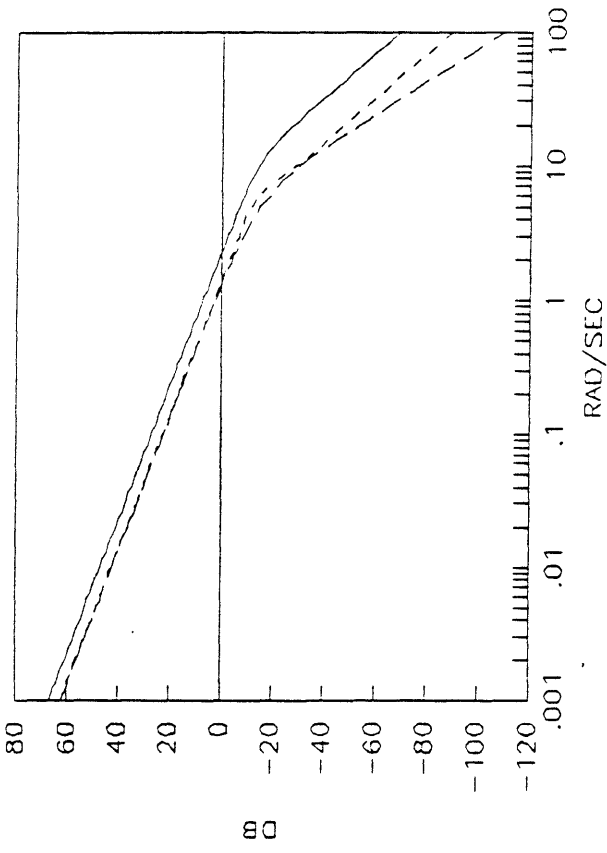


Figure 4.35 : Singular values of the loop tfm at point 2

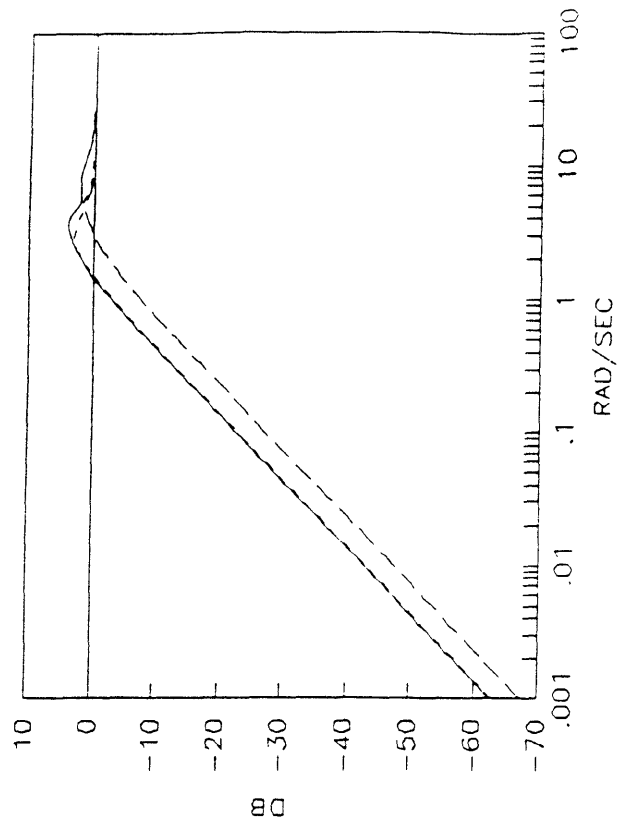


Figure 4.36 : Singular values of the sensitivity tfm at point 2

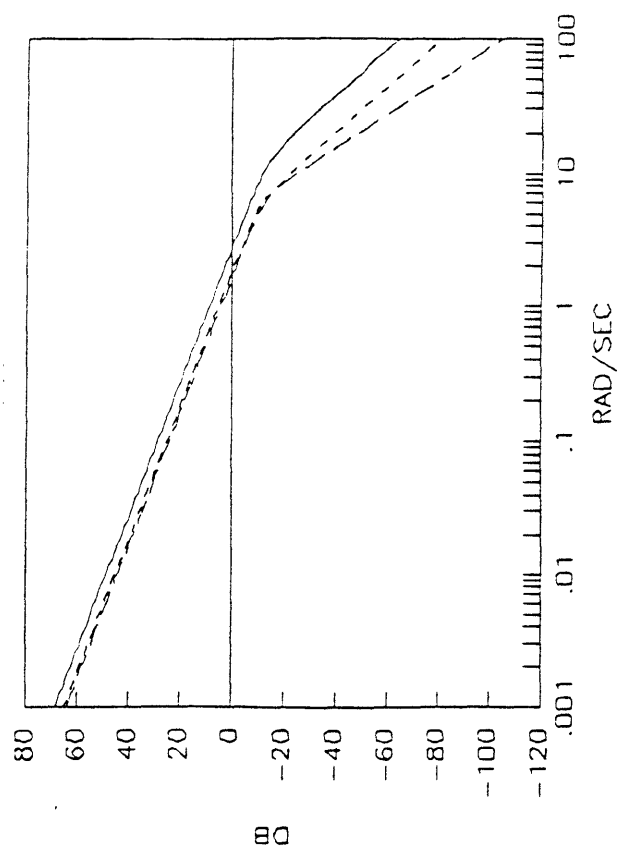


Figure 4.37 : Singular values of the loop tfm at point 3

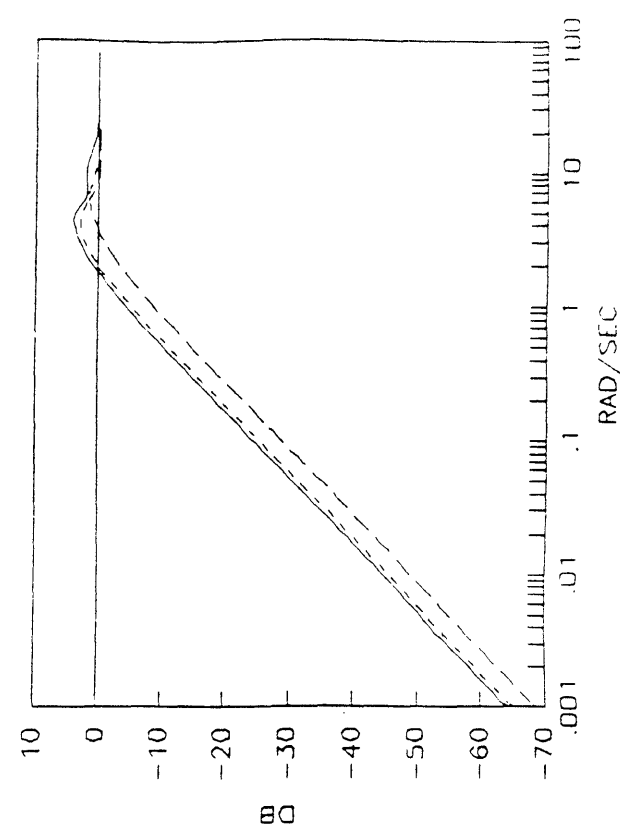


Figure 4.38 : Singular values of the sensitivity tfm at point 3

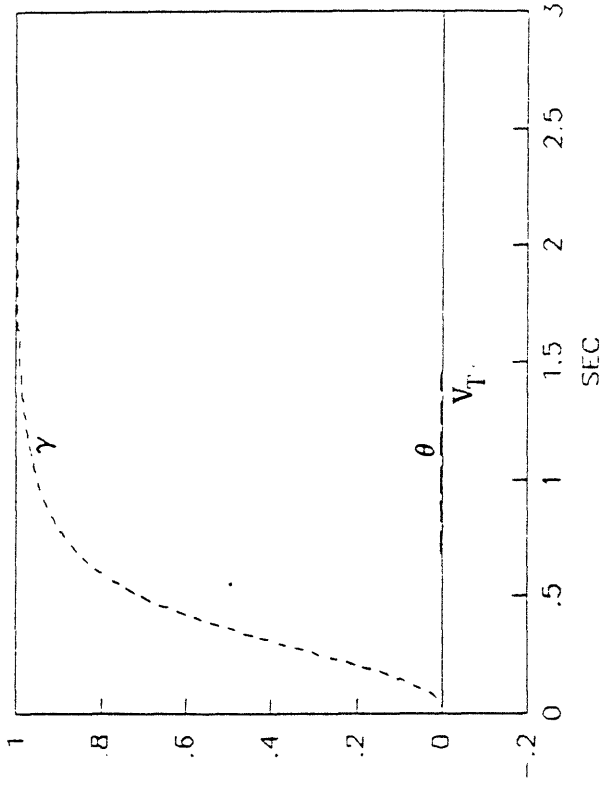


Figure 4.39 : Output response to r_1 at point 2

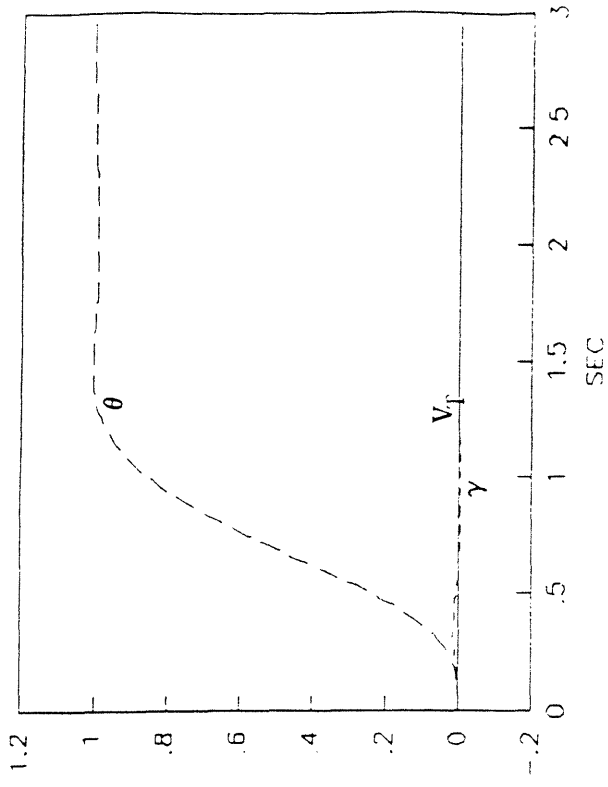


Figure 4.41 : Output response to r_2 at point 2

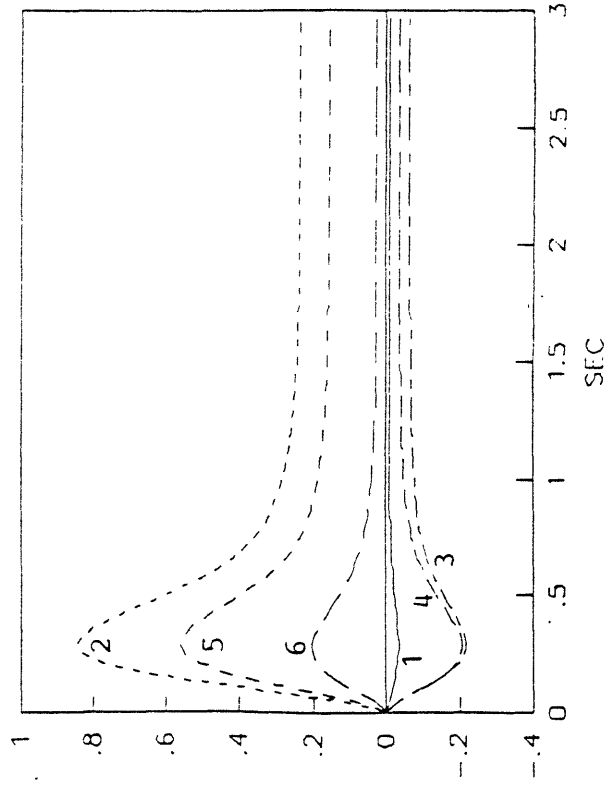


Figure 4.40 : Control response to r_1 at point 2

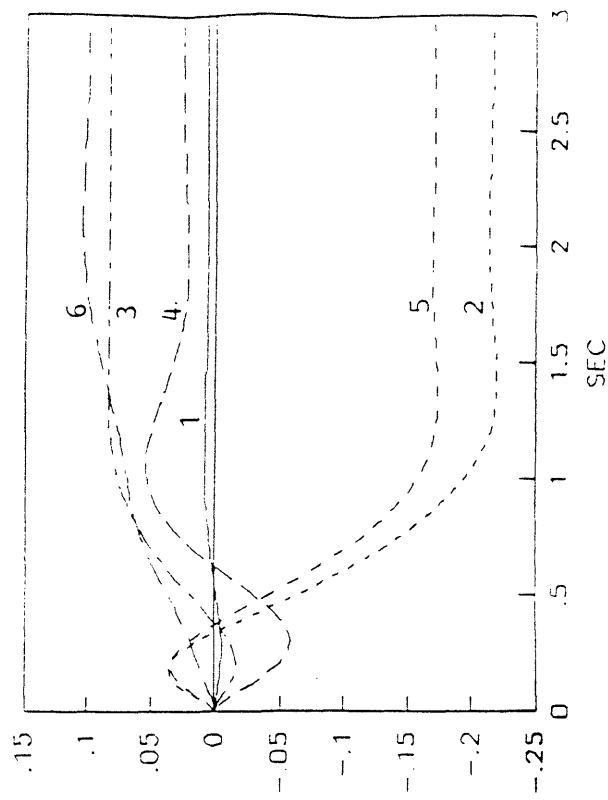


Figure 4.42 : Control response to r_2 at point 2

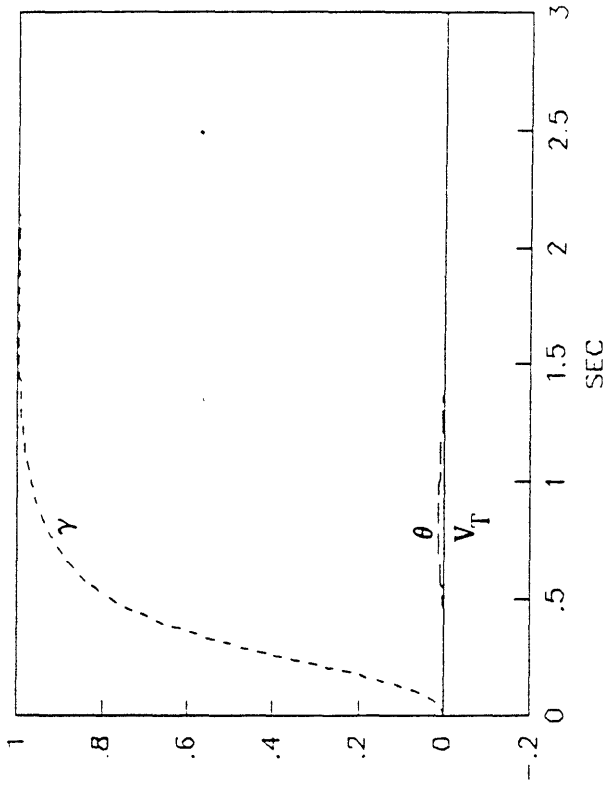


Figure 4.43 : Output response to r_1 at point 3

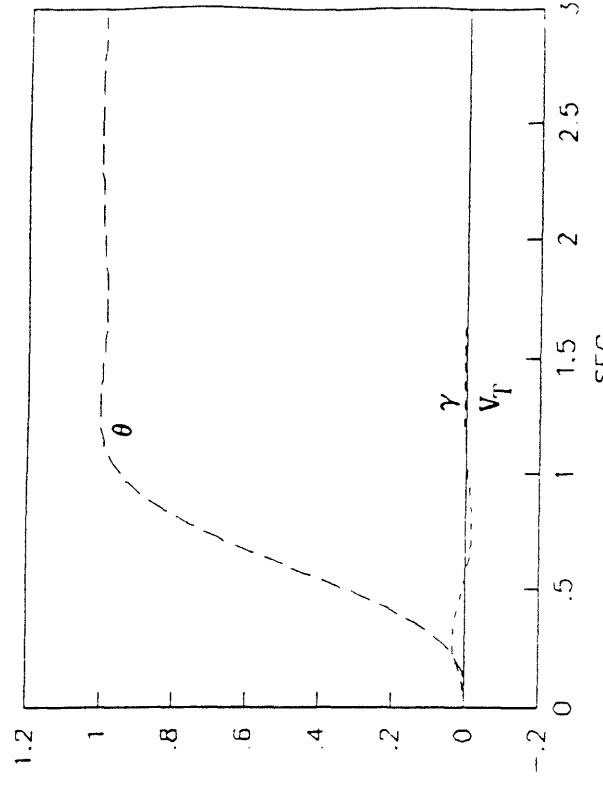


Figure 4.45 : Output response to r_2 at point 3

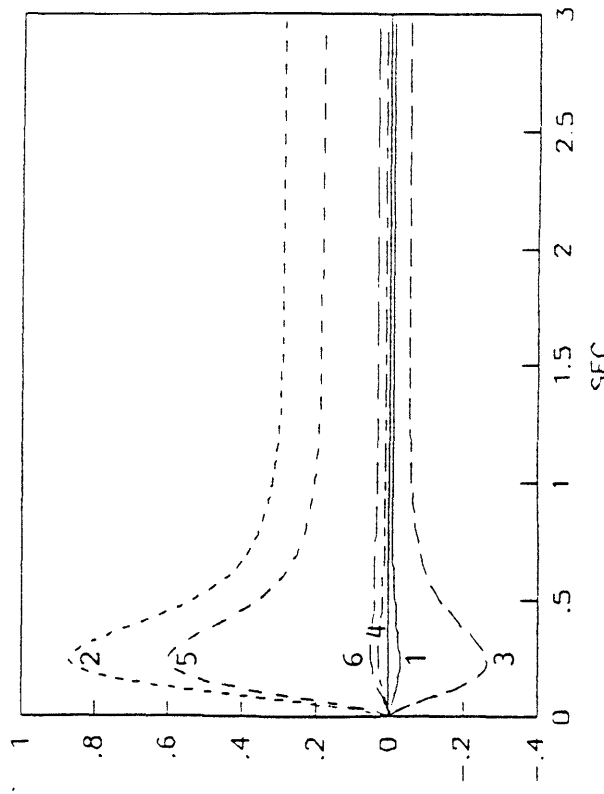


Figure 4.44 : Control response to r_1 at point 3

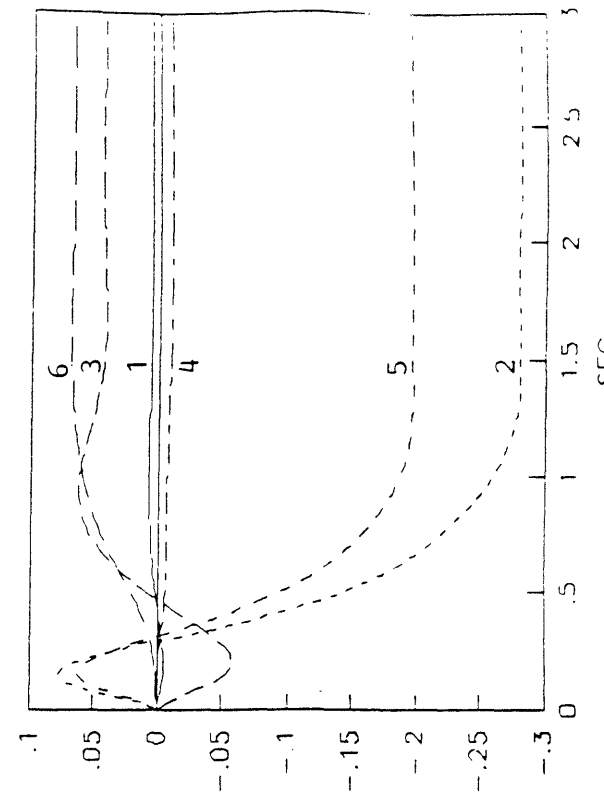


Figure 4.46 : Output response to r_2 at point 3

4.4 Design of the H_∞ Compensator

4.4.1 Introduction

The H_∞ design methodology, is highlighted in the following subsection. For readers unfamiliar with the subject, referene [4] provides the essentials.

4.4.2 Highlights of the H_∞ Methodology

The general interconnection structure of a feedback system can be represented as in figure 4.47 where

- M(s)** : finite dimensional LTI system
 - K(s)** : compensator
 - w** : exogenous input vector (commands, disturbances, sensor noise, etc.)
 - z** : output (any signal of interest: weighted errors, controls, etc.)
 - y** : measurement vector
 - u** : control input vector
-

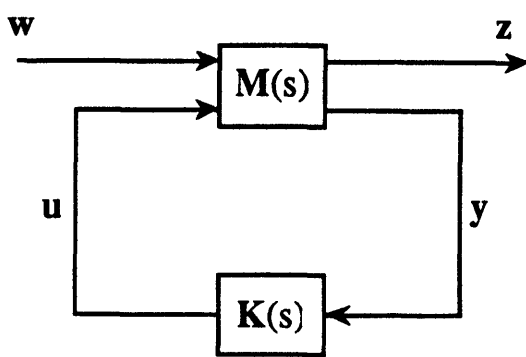


Figure 4.47: General framework

The objective in the H_∞ methodology is to find a stabilizing $K(s)$ such that the infinity norm of the transfer function $H_{zw}(s)$ from w to z is minimized i.e.

$$\min_{\text{stabilizing } K(s)} \|H_{zw}(s)\|_\infty = \min_{\text{stabilizing } K(s)} \left(\sup_{\omega} \sigma_{\max}[H_{zw}(j\omega)] \right)$$

This can be interpreted in the time domain as minimizing the worst case energy of the output z ($\|z\|_{L_2}$) when the energy of the input w ($\|w\|_{L_2}$) is bounded. Viewing it in the frequency domain, this minimization implies that the worst case steady state amplitude of the output z ($\|z\|_2$) is minimized when the input w is a bounded amplitude sinusoid.

The specifications can be used to condition the outputs (and/or inputs) with (stable) weights that are absorbed in the general system $M(s)$. Figure 4.48 shows the standard feedback loop transformed to the general framework.

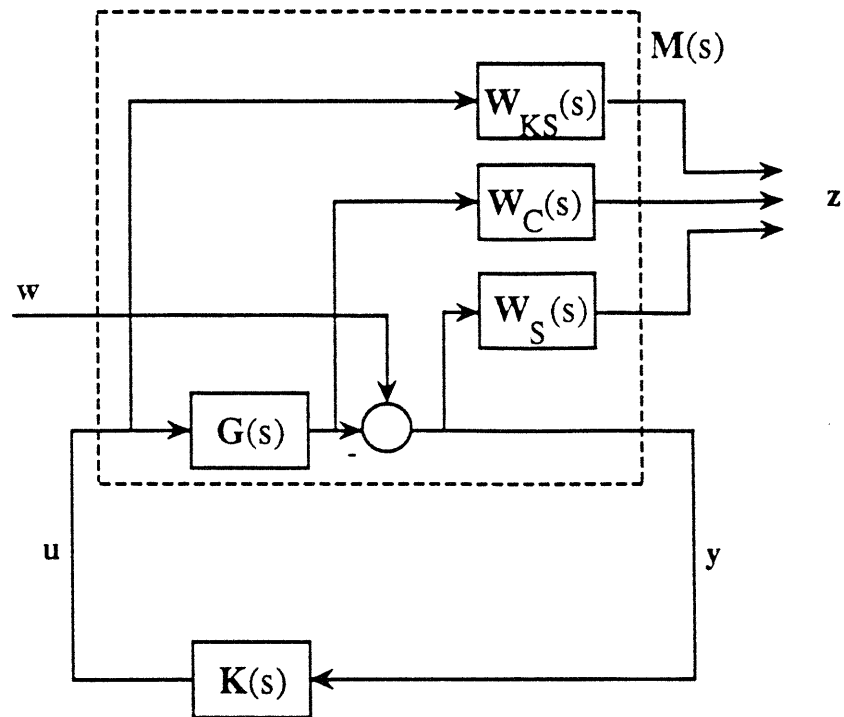


Figure 4.48 : Standard feedback loop transformed to the general framework

In general, the solution of the H_∞ problem cannot be computed directly. However, an iterative scheme, the so called γ -iteration, can be used to find solutions arbitrarily close to the optimal. In particular, this iterative approach consists of finding stabilizing compensators that guarantee

$$\|H_{zw}(s)\|_\infty < \gamma \quad (4.4.1)$$

with

$$\gamma > \gamma_{\text{opt}} = \min_{\text{stabilizing } K(s)} (||H_{zw}(s)||_{\infty})$$

Recent results in the area of H_{∞} synthesis by Doyle and Glover [12] provide a convenient method to solve the problem above by essentially solving two Riccati equations. This method is demonstrated below.

Let $M(s)$ be partitioned as:

$$M(s) = \begin{bmatrix} M_{11}(s) & M_{12}(s) \\ M_{21}(s) & M_{22}(s) \end{bmatrix}$$

with each element having the state space representation

$$M_{ij}(s) = [A, B_j, C_i, D_{ij}]; \quad i,j=1,2$$

The transfer functions $M_{11}(s)$, $M_{22}(s)$ must be strictly proper i.e. D_{11} , D_{22} should be zero. If this is not the case, then one has to add high frequency poles. Also, $M_{12}(s)$, $M_{21}(s)$ should be proper but not strictly proper.

Step 1: Guess a level of achievable performance γ

Step 2: Scale w and/or z so that the upper bound in (4.4.1) is 1 i.e.

$$||\tilde{H}_{zw}(s)||_{\infty} \leq 1 \text{ where } \tilde{H}_{zw}(s) \text{ is appropriately scaled.}$$

Step 3: Scale u and y so that

$$\mathbf{D}_{12}^T \mathbf{D}_{21} = \mathbf{I} \quad (4.4.2a)$$

$$\mathbf{D}_{21} \mathbf{D}_{21}^T = \mathbf{I} \quad (4.4.2b)$$

Step 4: The stabilizing compensator that achieves $\|\tilde{\mathbf{H}}_{zw}(s)\|_{\infty} \leq 1$ and, consequently, $\|\mathbf{H}_{zw}(s)\|_{\infty} \leq \gamma$ is given in Figure 4.49

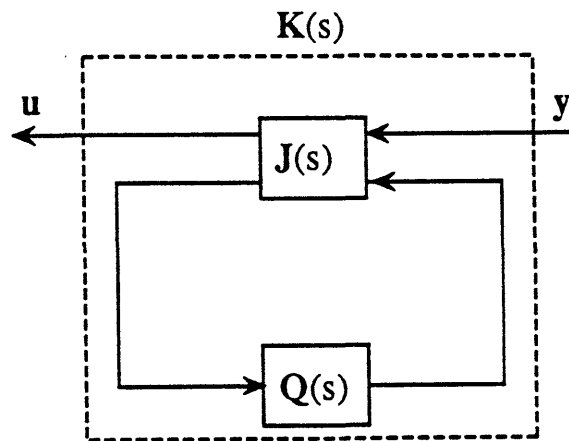


Figure 4.49: The H_{∞} compensator structure

where

$\mathbf{Q}(s)$ any stable system with

$$\|\mathbf{Q}(s)\|_{\infty} < 1$$

and $\mathbf{J}(s)$ is given by the state space description

$$\mathbf{J}(s) = [\mathbf{A}_J, \mathbf{B}_J, \mathbf{C}_J, \mathbf{D}_J] \quad (4.4.3)$$

with

$$\mathbf{A}_J = \mathbf{A} - \mathbf{K}_F \mathbf{C}_2 - \mathbf{B}_2 \mathbf{K}_C + \mathbf{Y}_{\infty} \mathbf{C}_1^T (\mathbf{C}_1 - \mathbf{D}_{12} \mathbf{K}_C)$$

$$\mathbf{B}_J = [\mathbf{K}_F \mathbf{K}_{F1}]$$

$$\mathbf{C}_J = \begin{bmatrix} -\mathbf{K}_c \\ \mathbf{K}_{c1} \end{bmatrix}$$

$$\mathbf{D}_J = \begin{bmatrix} \mathbf{0} & -\mathbf{I} \\ \mathbf{I} & \mathbf{0} \end{bmatrix}$$

$$\mathbf{K}_c = (\mathbf{B}^T \mathbf{X}_\infty + \mathbf{D}_{12}^T \mathbf{C}_1)(\mathbf{I} - \mathbf{Y}_\infty \mathbf{X}_\infty)^{-1}$$

$$\mathbf{K}_{c1} = (\mathbf{D}_{12} \mathbf{B}_1^T - \mathbf{C}_2)(\mathbf{I} - \mathbf{Y}_\infty \mathbf{X}_\infty)^{-1}$$

where \mathbf{X}_∞ is the unique, real, symmetric solution of the Algebraic Riccati equation

$$(\mathbf{A} - \mathbf{B}_2 \mathbf{D}_{12}^T \mathbf{C}_1)^T \mathbf{X}_\infty + \mathbf{X}_\infty (\mathbf{A} - \mathbf{B}_2 \mathbf{D}_{12}^T \mathbf{C}_1) - \mathbf{X}_\infty (\mathbf{B}_2 \mathbf{B}_2^T - \mathbf{B}_1 \mathbf{B}_1^T) \mathbf{X}_\infty + \mathbf{C}_1^T \mathbf{C}_1 = \mathbf{0}$$

with

$$\begin{aligned}C_1 &= (\mathbf{I} - \mathbf{D}_{12} \mathbf{D}_{12}^T) C_1 \\ \mathbf{K}_F &= (\mathbf{Y}_\infty \mathbf{C}_2^T + \mathbf{B}_1 \mathbf{D}_{21}^T) \\ \mathbf{K}_{F1} &= (\mathbf{Y}_\infty \mathbf{C}_1^T \mathbf{D}_{12} + \mathbf{B}_2)\end{aligned}$$

and \mathbf{Y}_∞ is the unique real symmetric solution of the Algebraic Riccati equation

$$(\mathbf{A} - \mathbf{B}_1 \mathbf{D}_{21}^T \mathbf{C}_2) \mathbf{Y}_\infty + \mathbf{Y}_\infty (\mathbf{A} - \mathbf{B}_1 \mathbf{D}_{21}^T \mathbf{C}_2)^T - \mathbf{Y}_\infty (\mathbf{C}_2^T \mathbf{C}_2 - \mathbf{C}_1^T \mathbf{C}_1) \mathbf{Y}_\infty + \mathbf{B}_1 \mathbf{B}_1^T = 0$$

with

$$\mathbf{B}_1 = \mathbf{B}_1 (\mathbf{I} - \mathbf{D}_{21}^T \mathbf{D}_{21})$$

Initial γ is achievable if

$$\begin{aligned}X_\infty &\geq 0 \\ Y_\infty &\geq 0 \\ \lambda_{\max}(X_\infty Y_\infty) &\leq 1\end{aligned}$$

Step 5: Scale back \mathbf{u} and \mathbf{y} to their initial (before step 3) scales.

A legitimate choice of $\mathbf{Q}(s)$ is $\mathbf{Q}(s) = 0$. This choice of $\mathbf{Q}(s)$ will be used in the design of the following section.

4.4.3 Application of the H_∞ Design Methodology to the F18/HARV

A design of an H_∞ compensator for operating point 1 is presented in this section. Similar steps can be used to design compensators for points 2 and 3. However, since the resulting designs do not really differ from the LQG/LTR ones, designs for points 2 and 3 will not be presented.

4.4.3.1 Selection of Weights

The selection of weights is one of the most important steps in the H_∞ methodology. They are used to emphasize one frequency range over another. It must be kept in mind that the selection of the weights reflects engineering judgement and, thus, a poor selection of these weights may result in poor designs. For example, posing a heavy penalty on the sensitivity, via $W_S(s)$, (figure 4.48) and on the complementary sensitivity, via, $W_C(s)$ in the same frequency region, does not make a lot of sense since

$$C(s) + S(s) = I$$

It should also be noted that the complexity of the compensator, namely its order, is equal to the sum of the orders of the plant, the weights, and of the parameter $Q(s)$. Therefore high order weights will result in a high order compensator.

In this design the output z was considered as the weighted error signal e and the weighted pseudocontrol v (figure 4.50). By minimizing $\|H_{ZW}(s)\|_\infty$, we minimize

$$\|W_S(s)e(s)\|_{L_2}^2 + \|W_{KS}(s)v(s)\|_{L_2}^2$$

which represents a tradeoff between bandwidth and control action.

Since the specifications ask for zero steady state error to constant commands and disturbances, the weight $W_S(s)$ should be large at low frequencies. (In fact, $W_S(s) \rightarrow \infty$ as $s \rightarrow 0$). The robustness and noise attenuation specifications require that $\sigma_{\max}[S(j\omega)] \approx 1$ for large ω so that $\sigma_{\max}[C(j\omega)]$ rolls off.

If the (pseudo) control v is not weighted enough then the resulting loop tends to have high bandwidth and, thus, the resulting control action is excessive.

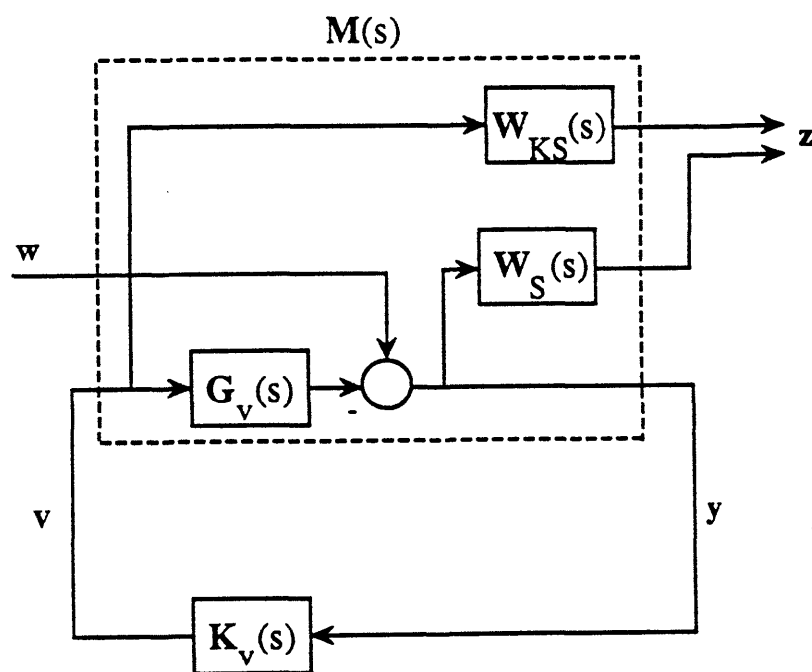


Figure 4.50: Framework for the H_∞ compensator design for the pseudosystem

Consequently, sufficient penalties should be posed on the control signal v . In particular, the weighting should be heavier as frequency increases so that $\mathbf{K}_v(s)\mathbf{S}(s)$ would be forced to roll off; thus extremely fast control action (rate limits) would be prevented. If $\mathbf{K}_v(s)\mathbf{S}(s)$ is not forced to roll off then the control action would be more impulsive.

Having these in mind the following (diagonal) weights were selected:

$$\mathbf{W}_S(s) = \frac{s+3}{(s+.0001)(s/1000+1)} \mathbf{I}_{3 \times 3}$$

$$\mathbf{W}_{KS}(s) = \frac{1}{7} \frac{(s/4+1)}{(s/1000+1)} \mathbf{I}_{3 \times 3}$$

Figures 4.51, 4.52 show the singular values $\sigma_i[\mathbf{W}_S(j\omega)]$, $\sigma_i[\mathbf{W}_{KS}(j\omega)]$.

Due to the requirements of the Glover/Doyle method, the high frequency pole of $\mathbf{W}_S(s)$ at $s=-1000$ was selected so that $\mathbf{D}_{11}=0$ ($\mathbf{D}_{22}=0$ since $\mathbf{G}_v(s)$ is strictly proper). The zero at $s=-3$ indicates the desired bandwidth whereas the pole at $s=-.0001$ represents a sufficiently good approximation of a pole at the origin so that the zero steady state requirement is met.

The weighting on the control $\mathbf{W}_{KS}(s)$ was adjusted so that the saturation levels were preserved for the commands considered in section 4.2. The fast pole at $s=-1000$ was inserted to make $\mathbf{W}_{KS}(s)$ proper.

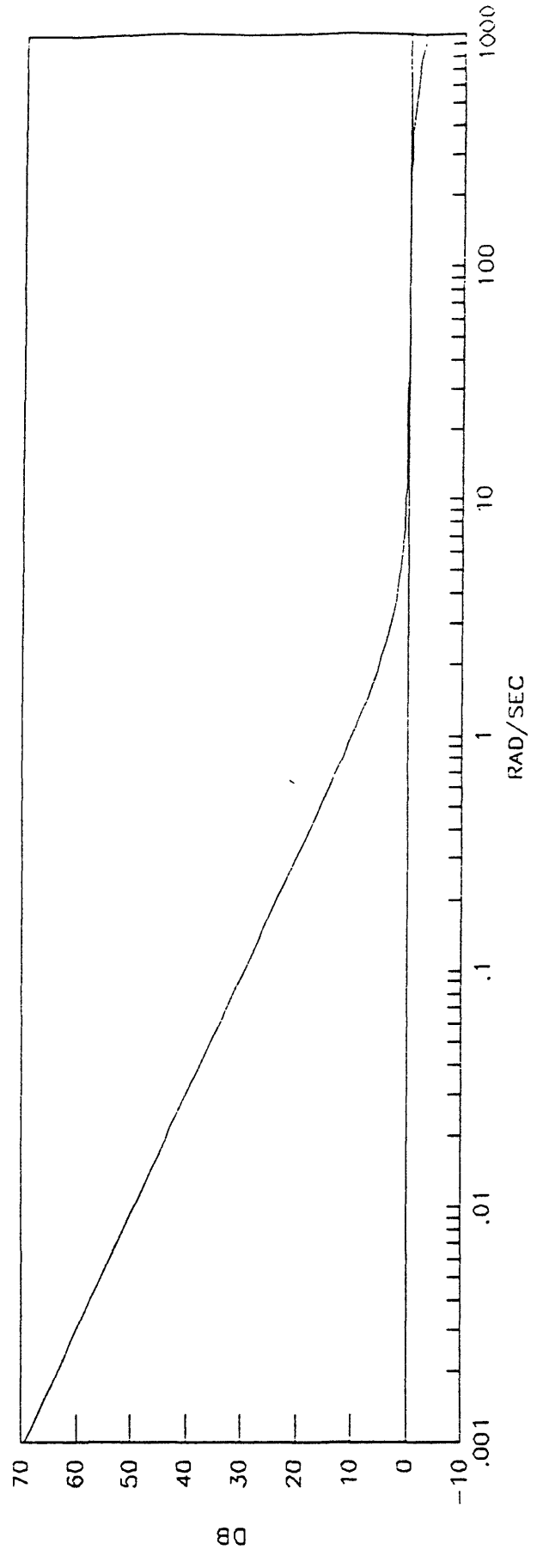


Figure 4.51 : Singular values of the weighting $W_S(s)$

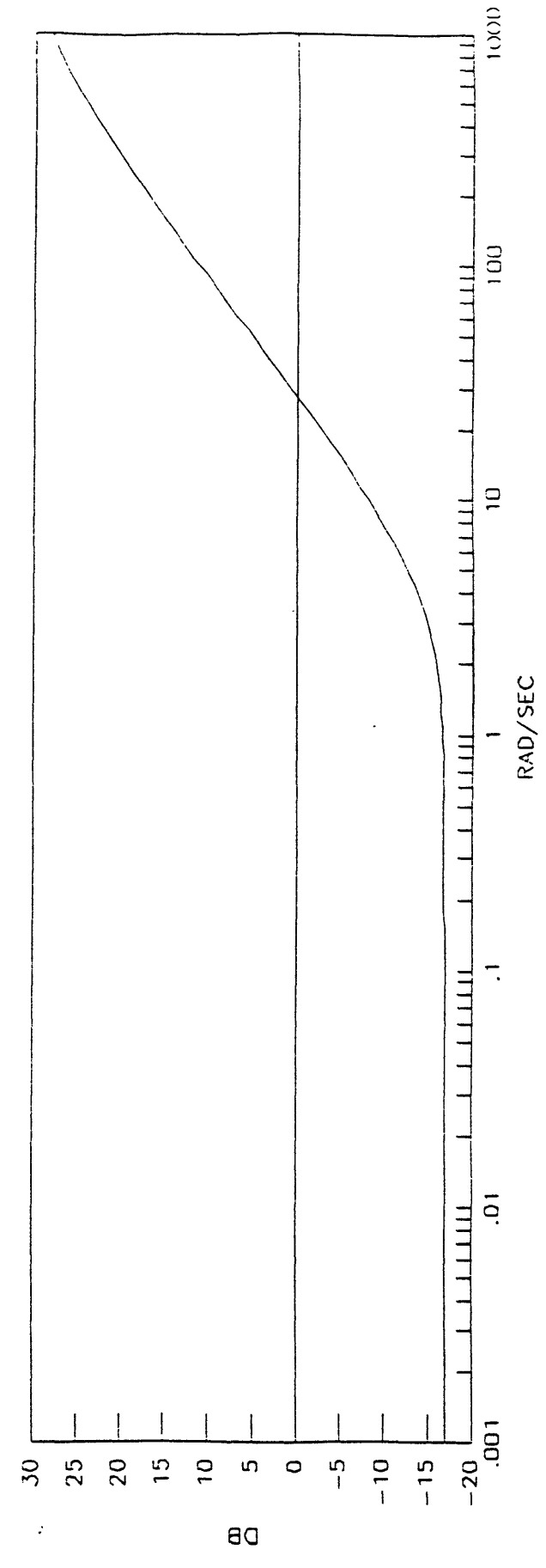


Figure 4.52 : Singular values of the weighting $W_{KS}(s)$

4.4.3.2 Resulting Feedback Loop Design

Performing the steps of subsection 4.4.2, the minimum value γ_{opt} of $\|H_{zw}(s)\|_{\infty}$ over all stabilizing controllers $K_v(s)$ was found to be in the interval (2.520, 2.525]. For $\gamma=2.525$ the resulting compensator $K_v(s)$ that stabilizes the system and guarantees $\|H_{zw}(s)\|_{\infty} \leq 2.525$ was obtained via the Glover/Doyle algorithm.

The singular values $\sigma_i[G_v(j\omega)K_v(j\omega)]$ and $\sigma_i[(I+G_v(j\omega)K_v(j\omega))^{-1}]$ of the loop and sensitivity transfer functions are shown in figures 4.53 and 4.54 respectively. As it can be verified from these plots, the frequency domain specifications are met. The loop crossover is approximately at 2 rad/sec and 1.2 rad/sec for the maximum and minimum singular value respectively, which implies that the settling time should range from approximately 1.5 sec up to 2.5 sec. The stability margins can be evaluated from the sensitivity singular value plot. In particular, $\|S(s)\|_{\infty} \approx 3.7$ which implies:

$$\uparrow \text{GM} \geq 9. \text{ db}$$

$$\downarrow \text{GM} \leq -8 \text{ db}$$

$$|\text{PM}| \geq 38 \text{ deg}$$

An interesting point to note is that the loop (as well as the sensitivity) singular values are almost matched at the low frequency region $\omega < 10$ rad/sec. There is no guarantee, however, that this is going to be true for different weightings. Figures 4.55, 4.56, show the singular values $\sigma_i[K_v(j\omega)]$ and $\sigma_i[K_v(j\omega)(I+G_v(j\omega)K_v(j\omega))^{-1}]$ of the compensator and the r to v transfer functions. The poles and zeros of the compensator $K_v(s)$ and closed loop system $C(s) = (I+G(s)K_v(s))^{-1}G(s)K_v(s)$ are shown in Table 4.4.

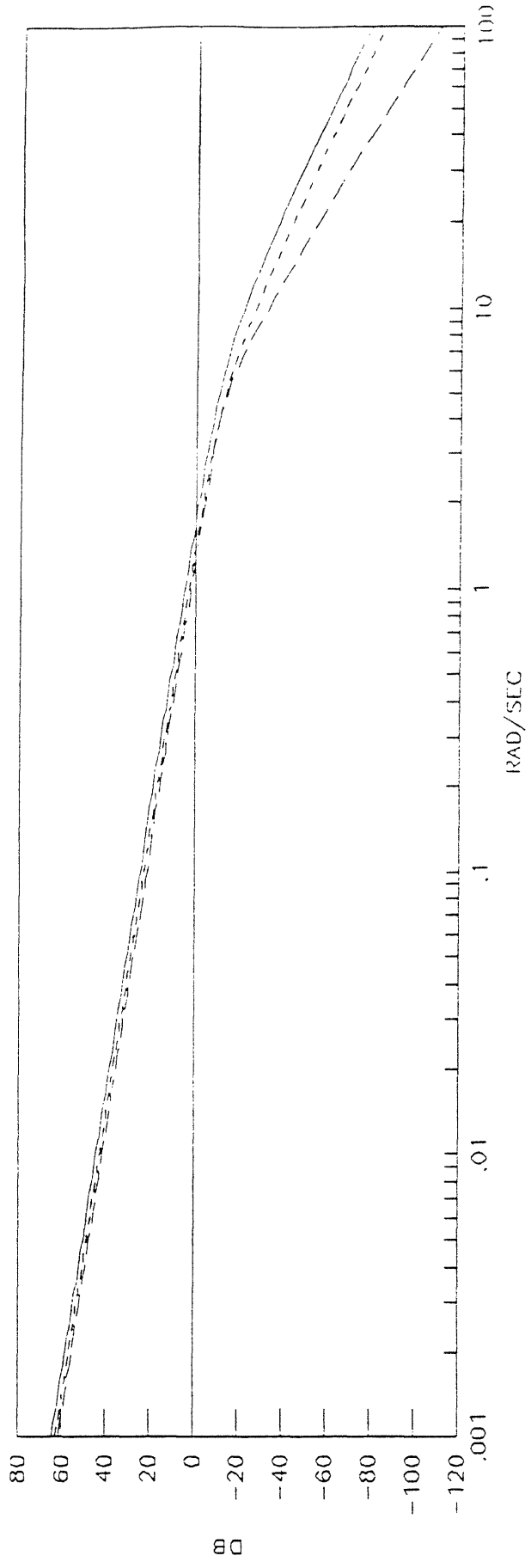


Figure 4.53 : Singular values of the loop $G_V(s)K_V(s)$

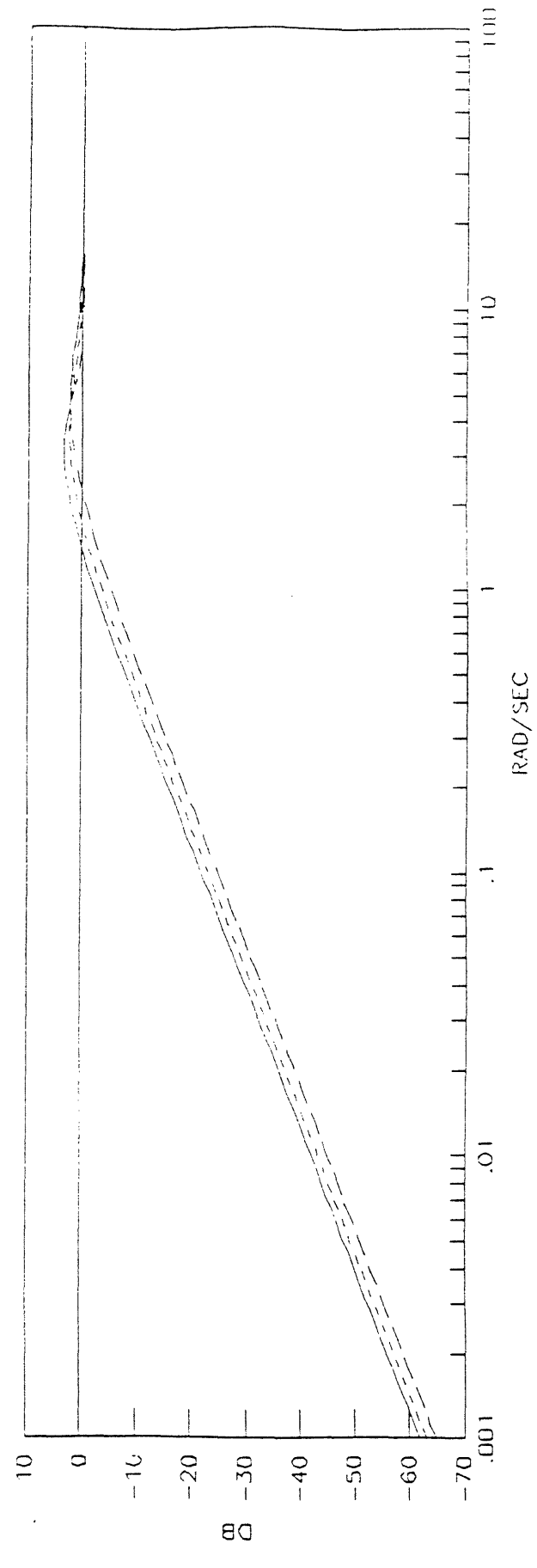


Figure 4.54 : Singular values of the sensitivity $(I+G_V(s)K_V(s))^{-1}$

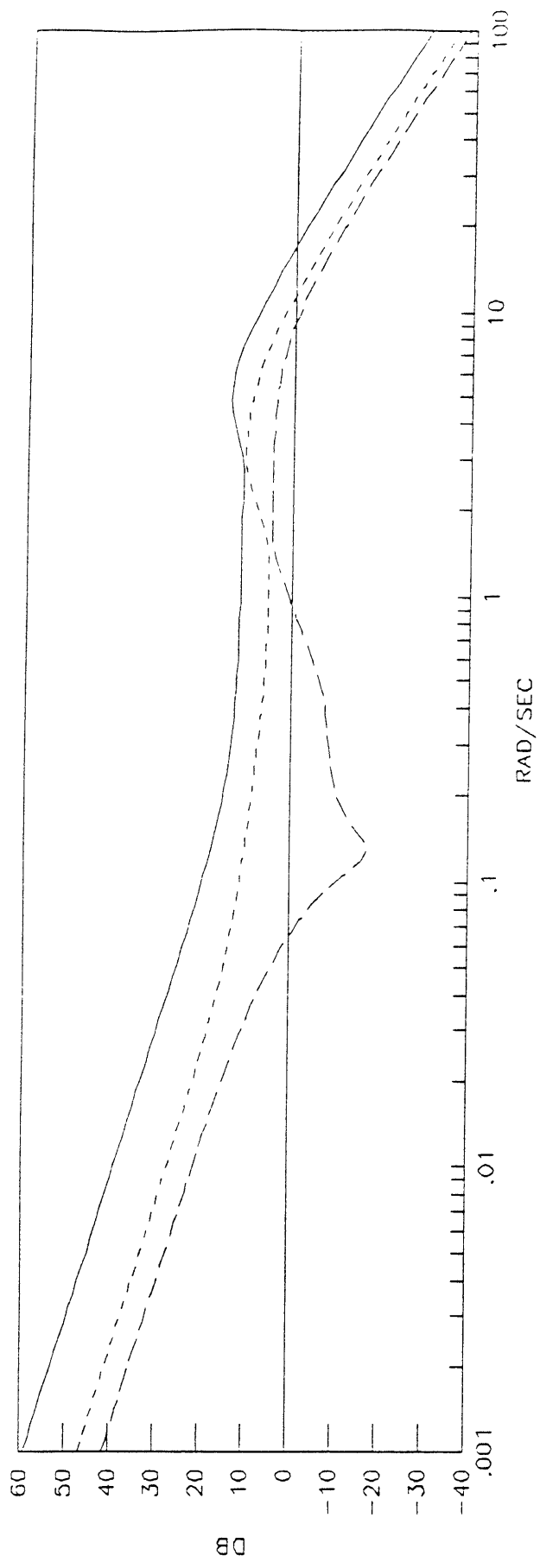


Figure 4.55 : Singular values of the compensator $K_V(s)$

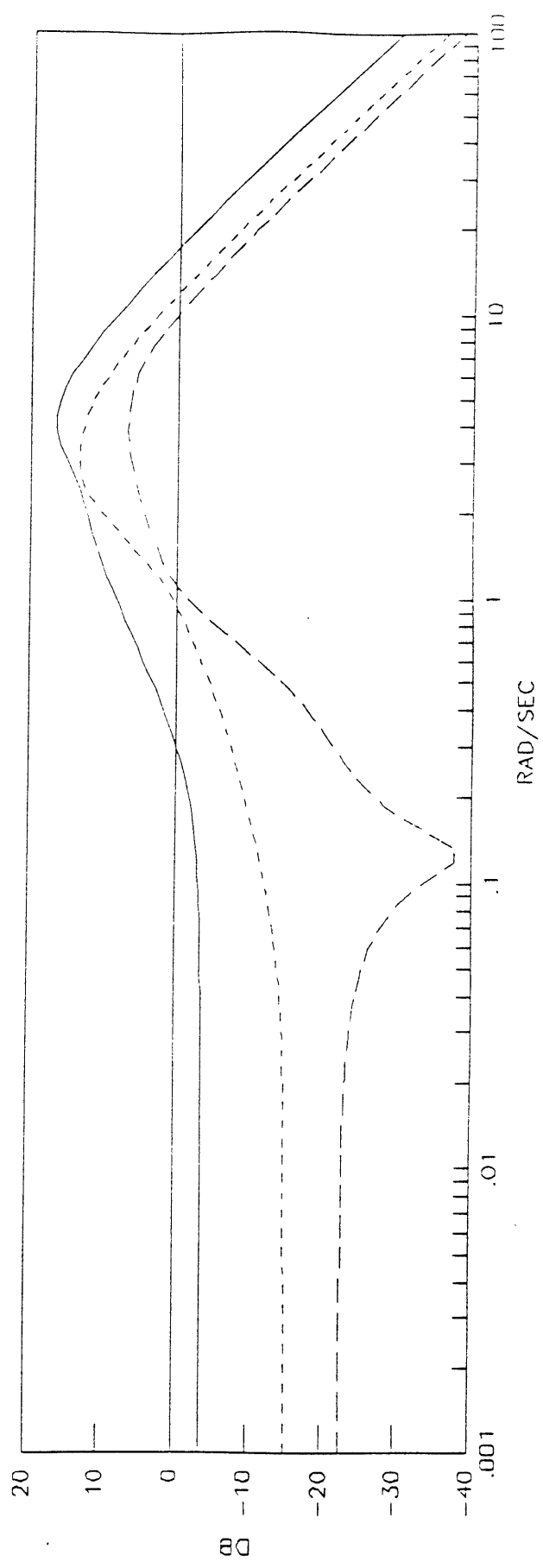


Figure 4.56 : Singular values of the $K_V(s)(I+G_V(s)K_V(s))^{-1}$

Table 4.4

Poles and zeros of the compensator $K_V(s)$ and closed loop system $C(s)$

$K_V(s)$		$C(s)$	
Poles	Zeros	Poles	Zeros
$-3.19 \pm 4.59j$	- 918.2	- 1000	- 911.7
$-5.04 \pm 3.81j$	- 911.7	- 1000	- 918.2
$-6.17 \pm 5.31j$	- 916.3	- 1000	- 916.3
- 7.75	$-.0180 \pm .1248j$	$-4.63 \pm 4.05j$	$-.0180 \pm .1248j$
- 1000	$-.2481 \pm .3585j$	$-2.51 \pm 3.15j$	$-.2481 \pm .3585j$
- 1000	- 1000	- 6.01	- 1000
- 1000	- 1000	- 3.09	- 1000
0	- 1000	- 3.05	- 1000
0		$-.2481 \pm .3585j$	
0		$-.0187 \pm .1280j$	

4.4.3.3 Time Domain Simulations and Design Tradeoffs

The resulting time domain simulation for the step commands

$$r_1 = [0 \ 0 \ 1]^T \text{ vertical translation of 1 deg in } \gamma$$

$$r_2 = [0 \ 1 \ 0]^T \text{ pitch pointing of 1 deg in } \theta$$

$$r_3 = [0 \ 1 \ 1]^T \text{ direct lift of L deg in } \theta \text{ and } \gamma$$

$$r_4 = [1/2 \ 0 \ 0]^T \text{ horizontal acceleration of 4ft/sec in } V_T$$

are shown in figures 4.57, 4.58, 4.59 and 4.60 respectively.

Using the same distribution matrix for the pseudocontrol as in the LQG/LTR design the required control action is shown in Figures 4.61, 4.62, 4.63 and 4.64. The same comments as in the LQG/LTR design, regarding the discussion of the transients, hold. The same tradeoffs as in the LQG/LTR design also hold. In particular, a second design considerably relaxing the rolloff of

$K_v(s) S(s)$ by moving the zero of $W_{KS}(s)$ from -4 to -100 was performed. The resulting loop and sensitivity shapes are shown in figures 4.65, 4.66. Obviously, the bandwidth is almost the same but the phase and gain margins are improved:

$$\|S(s)\|_{\infty} \approx 2 \text{ db which implies}$$

$$\uparrow \text{GM} \geq 14 \text{ db}$$

$$\downarrow \text{GM} \leq -5 \text{ db}$$

$$|\text{PM}| \geq 47 \text{ deg}$$

However, the improvement of stability margins is done at the expense of faster control action. Figures 4.67 and 4.68 depict the output response and the required control action when a 1 deg in γ vertical translation maneuver is commanded. Clearly as shown in figure 4.66 the rate limits are not respected.

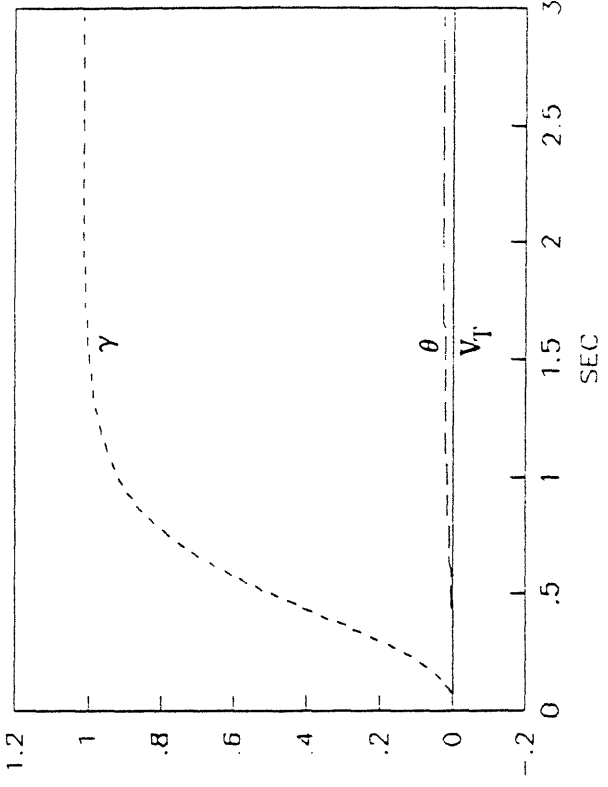


Figure 4.57 : Output response to r1

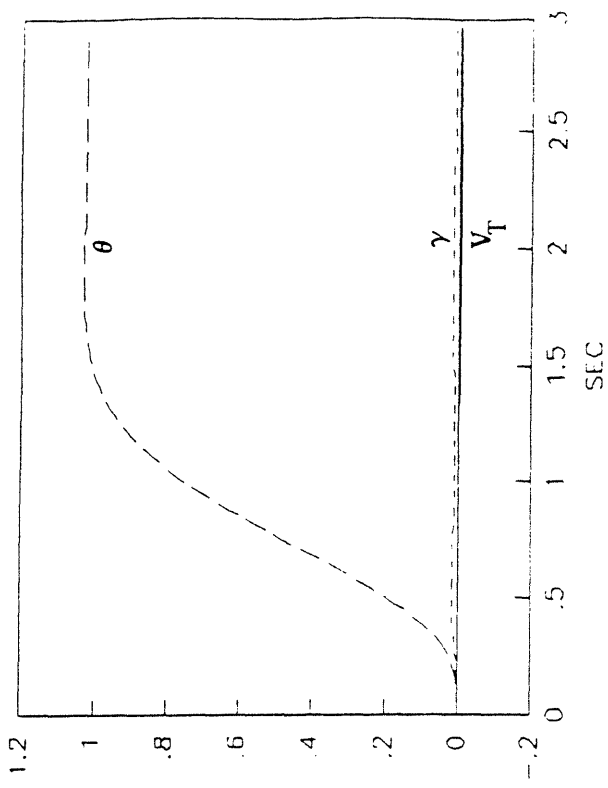


Figure 4.58 : Output response to r2

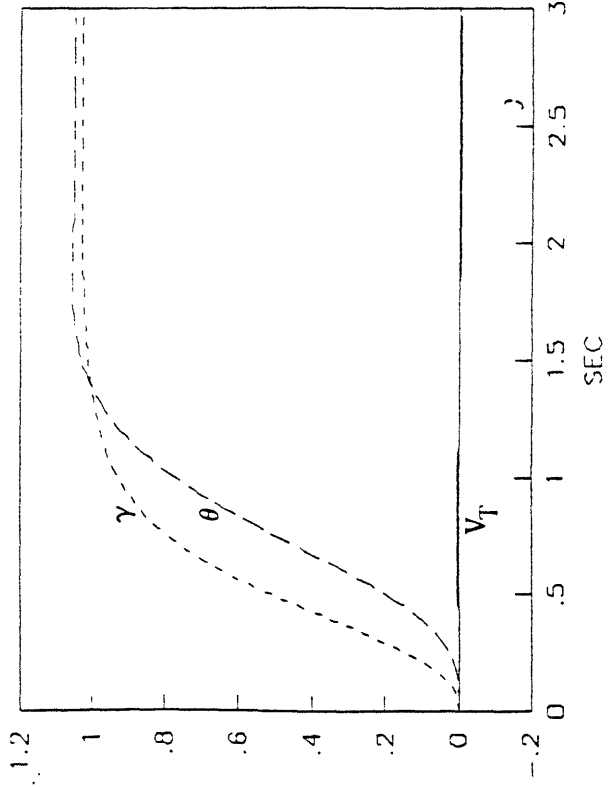


Figure 4.59 : Output response to r3

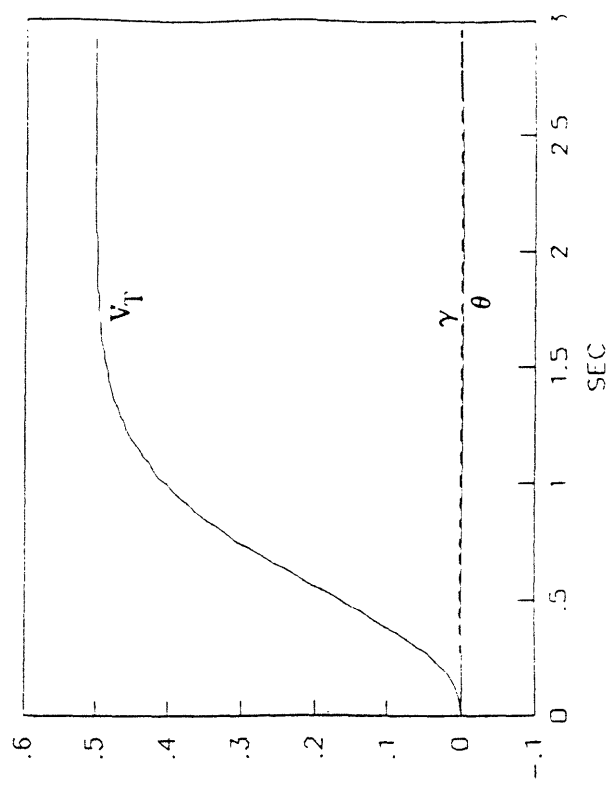


Figure 4.60 : Output response to r4

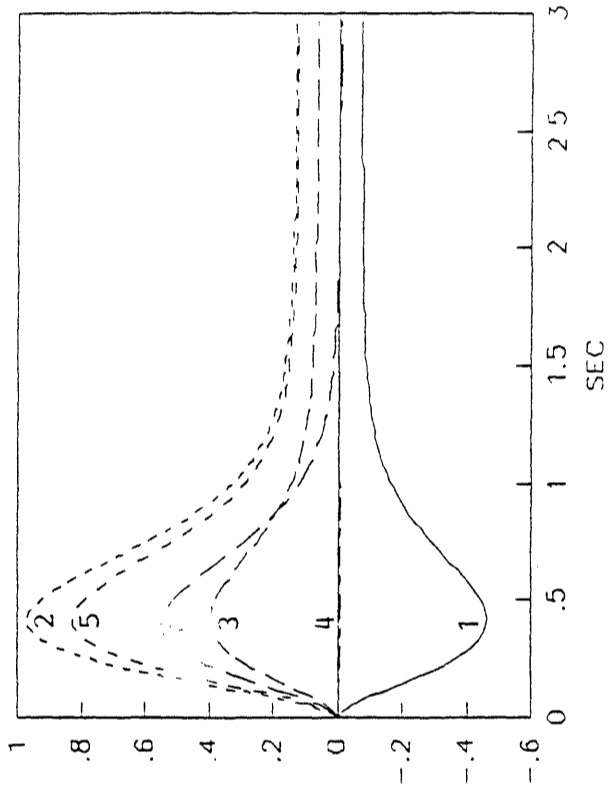


Figure 4.61 : Control response to r_1

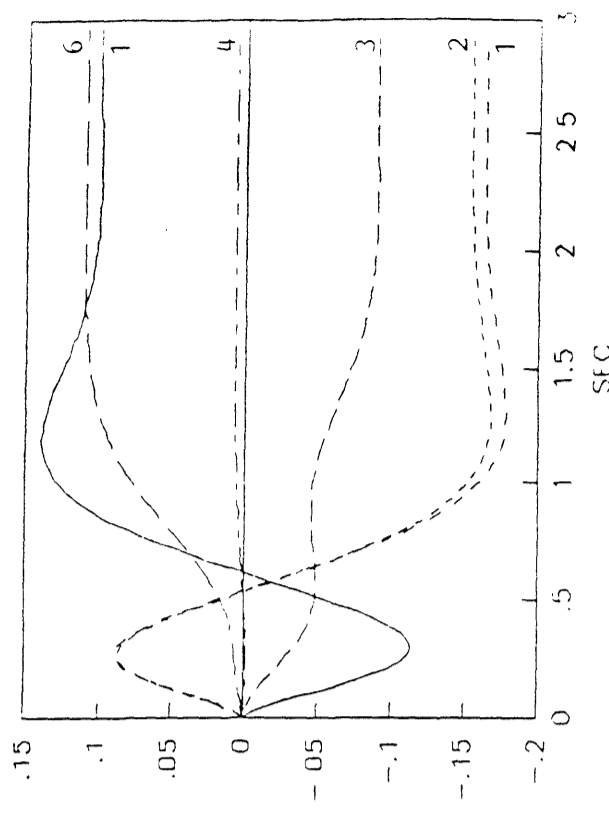


Figure 4.62 : Control response to r_2

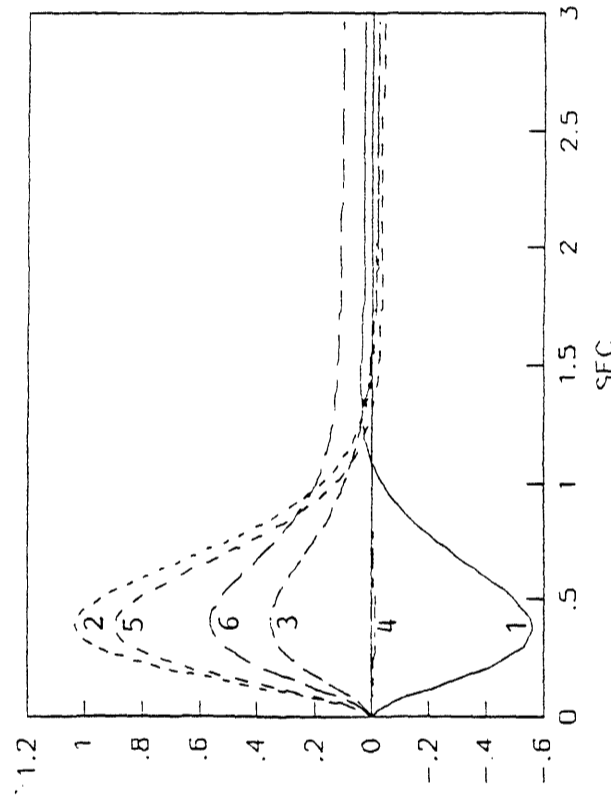


Figure 4.63 : Control response to r_3

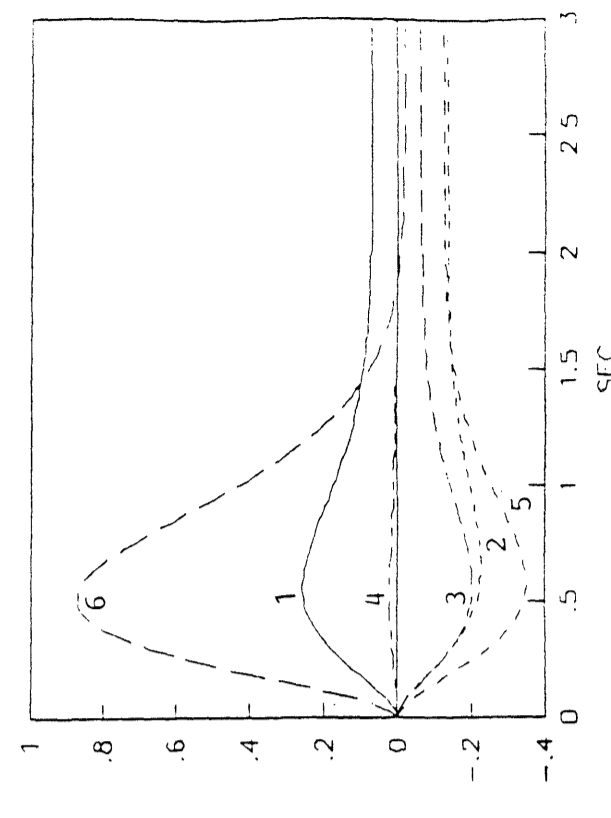


Figure 4.64 : Control response to r_4

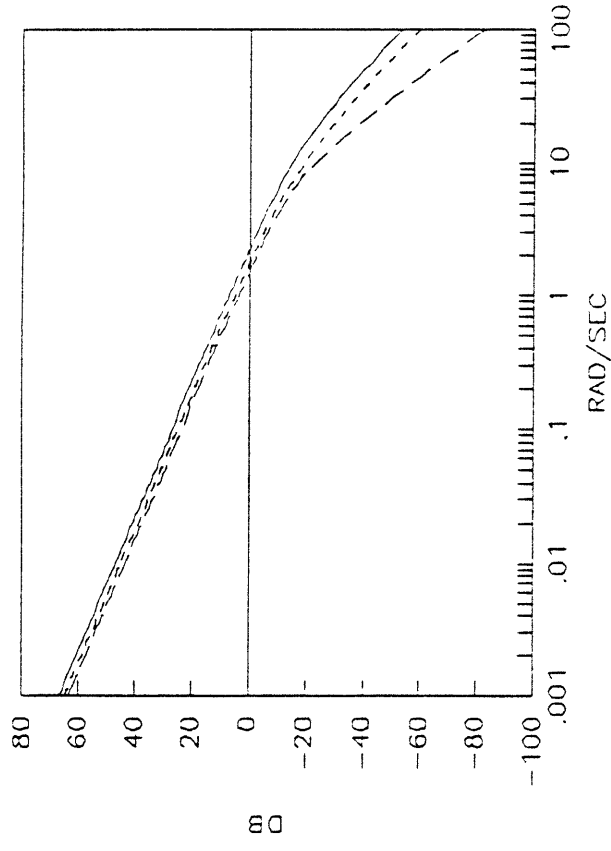


Figure 4.65 : Singular values of the loop tfm

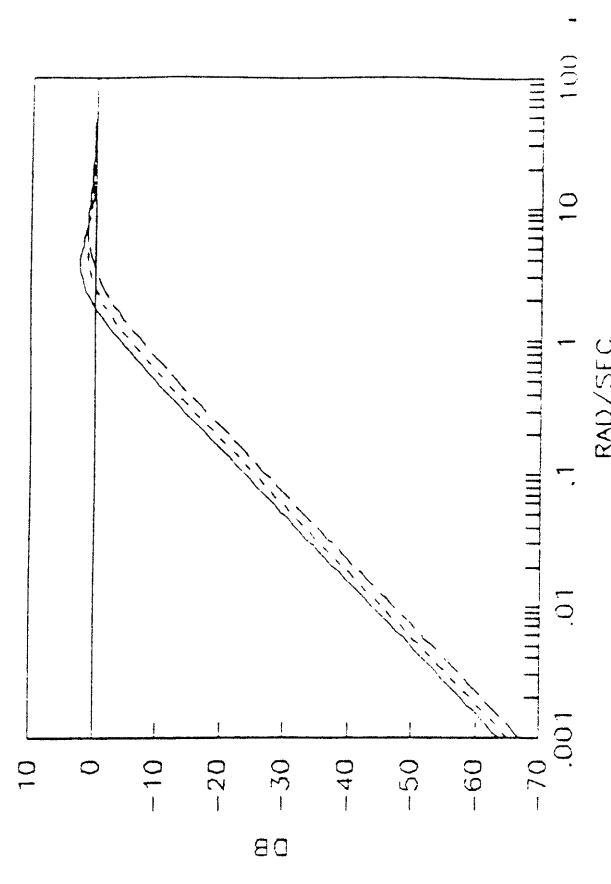


Figure 4.66 : Singular values of the sensitivity tfm

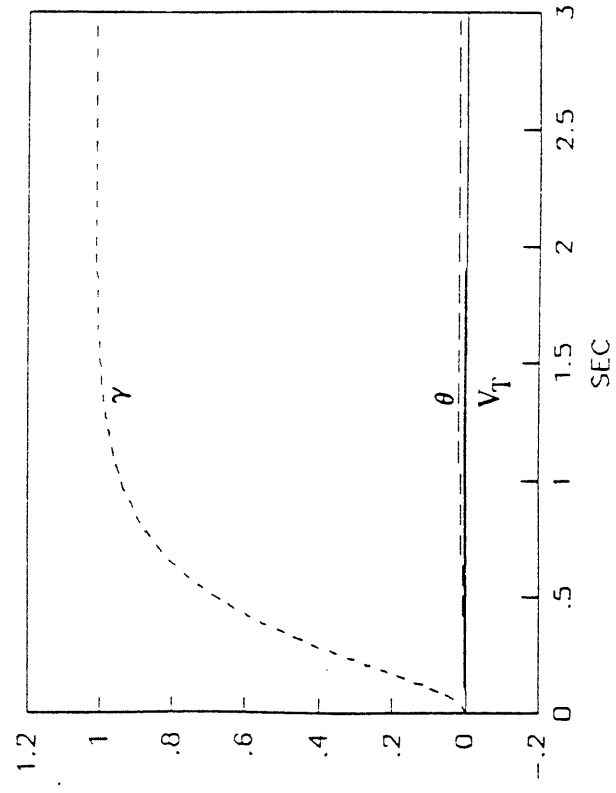


Figure 4.67 : Output response to r1

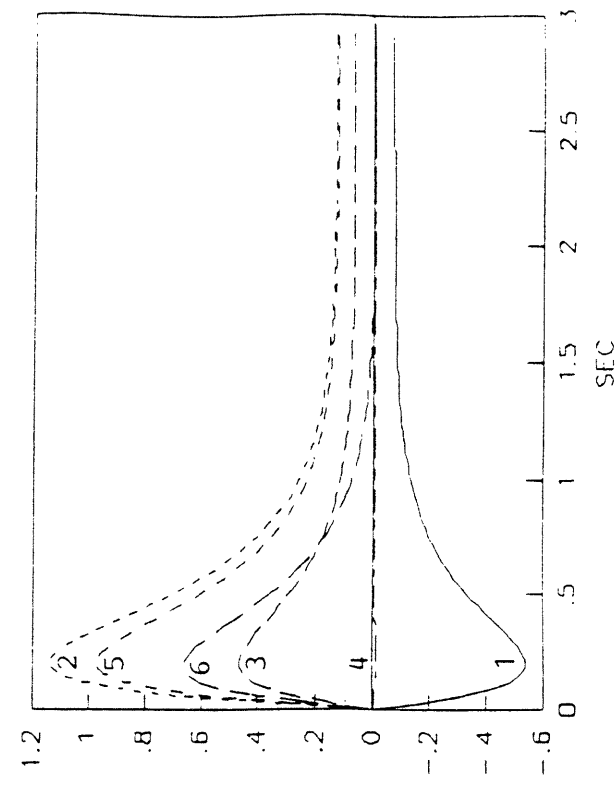


Figure 4.68 : Control response to r1

4.6 Comparison of the LQG/LTR and H_∞ Compensator Designs

In this section, the discussion is limited to operating point 1 since similar conclusions hold for the other two operating points.

From the previous sections 4.4, 4.5, one can conclude that there do not exist any major differences between the two designs. For all practical purposes, the loop shapes are the same as are the time responses. Also, the same tradeoffs appear.

More specifically, the H_∞ compensator resulted in slightly better phase and gain margins without any increase in magnitude and speed of the control action. Also, the H_∞ loop shapes were slightly better matched and the resulting sensitivity transfer function was slightly superior in the low frequency region. The high frequency rolloff of the loop in the H_∞ design started at slightly higher frequencies than in the LQG/LTR which resulted in slightly better stability margins. The point to make though, is that these are not significant differences. Moreover, if one takes into consideration that the 13th order H_∞ compensator has 3 more states than the 10th order LQG/LTR compensator, then it becomes very hard to tell which is better. Furthermore, after the recent developments by Doyle et.al, it is no more difficult to design an H_∞ compensator than it is to design an LQG/LTR one. However, in the H_∞ framework, the outputs to be controlled are not required to be measured, as they are in the LQG/LTR framework. This fact seems to give an edge of the H_∞ over the LQG/LTR methodology.

4.6 Summary

In this chapter the LQG/LTR and H_∞ design methodologies were applied to the 3 scaled linear models of the F18/HARV. The resulting designs meet prescribed nominal performance and robustness specifications. The saturation limits impose fundamental constraints on the speed of response and on the stability margins of the system. More specifically, low rate saturation limits conflict with highly demanding phase and gain margins specifications.

In this chapter, we also illustrated that the LQG/LTR and H_∞ designs were virtually identical. Although we saw that the H_∞ design obtained is slightly superior, this is counterbalanced by a more complex H_∞ compensator. As with the formal loop shaping LQG/LTR design methodology, the H_∞ procedure possesses sufficient degrees of freedom to also address loop shaping (albeit more complicated). However, one advantage of the H_∞ methodology is the fact that variables we wish to control need not be measurable.

CHAPTER 5 HANDLING OF FAILURES

5.1 Introduction

In the previous chapter, LQG/LTR and H_∞ designs were obtained. For each design the final control signals were generated from pseudocontrol signals, via a distribution matrix. This was done under the assumption that all actuators were operational. However, this may not be the case. For example, if there is an actuator failure then the associated control signal cannot be used. In such a situation, if the original distribution algorithm is used, the closed loop system may go unstable. Instead of redesigning the controller, what we will do is redesign the distribution algorithm. By doing so we not only guarantee nominal stability, but performance remains unaltered. This chapter addresses the application of the above distribution redesign philosophy.

5.2 Pseudocontrol Distribution in the Presence of Failures

As stated in chapter 3 the pseudocontrol input, v , is distributed to the actual control, u , via the distribution matrix, T , in such a way so that

$$u^T W u \text{ is minimized subject to the constraint } B_1 u = v \quad B_1 \in R^{3 \times 6}, \quad (5.2.1)$$

where $\mathbf{W} = \mathbf{W}^T > 0$, $\mathbf{W} \in \mathbb{R}^{6 \times 6}$. The resulting \mathbf{T} was shown to be:

$$\mathbf{T} = \mathbf{W}^{-1} \mathbf{B}_1^T (\mathbf{B}_1 \mathbf{W}^{-1} \mathbf{B}_1^T)^{-1} \quad (5.2.2)$$

where, in general, \mathbf{W} can have off diagonal terms. In this thesis only diagonal structures of \mathbf{W} are considered; i.e. $\mathbf{W} = \text{diag}(w_1, w_2, w_3, w_4, w_5, w_6)$ with $w_i > 0$, $i = 1, 2, \dots, 6$.

If the i^{th} control is in fact not usable then one can simply select $w_i = \infty$ and keep the other weights the same. After performing the minimization in (5.2.1) with the new weight, call it \mathbf{W}_i , a new distribution matrix, \mathbf{T}_i , is obtained.

Obviously when this distribution matrix is used, the nominal stability, stability robustness, and performance characteristics of the closed loop system do not change. This is evident from the fact that the compensator design was based on the pseudosystem, $\mathbf{G}_v(s)$. More specifically, it can easily be shown that the new distribution matrix, \mathbf{T}_i , will be given by:

$$\mathbf{T}_i = \lim_{w_i \rightarrow \infty} \mathbf{W}^{-1} \mathbf{B}_1^T (\mathbf{B}_1 \mathbf{W}^{-1} \mathbf{B}_1^T)^{-1} = \tilde{\mathbf{W}}^{-1} \tilde{\mathbf{B}}_1^T (\tilde{\mathbf{B}}_1 \tilde{\mathbf{W}}^{-1} \tilde{\mathbf{B}}_1^T)^{-1}$$

where $\tilde{\mathbf{W}}$ is simply what is left of \mathbf{W} if one removes the i^{th} row and column. Analogously, $\tilde{\mathbf{B}}_1$ is what is left of \mathbf{B}_1 if one were to remove its i^{th} column.

Clearly, the above procedure can be generalized if more than one control fails. As expected, this is done by setting the appropriately corresponding weights equal to infinity

and performing a similar minimization to that in (5.2.1).

One should note that the number of controls which fail should not exceed three in order for our distribution redesign philosophy to be applicable. This is because, in such a situation, $\mathbf{B}_1\mathbf{u}$, where at least four of the elements of \mathbf{u} are required to be zero, cannot generate all \mathbf{v} 's in \mathbb{R}^3 . Hence the constraint $\mathbf{B}_1\mathbf{u} = \mathbf{v}$ cannot, in general, be satisfied when this is the case. Under such extreme conditions we are forced to redesign the entire control system.

5.3 Time Simulations

To illustrate the flexibility of the design based on the pseudosystem $\mathbf{G}_v(s)$ the following cases were considered:

- i) failures of thrust vectoring vane and leading edge flaps
- ii) failure of aileron and leading edge flap
- iii) failure of stabilator and leading edge flap
- iv) failure of thrust vectoring vane, aileron and leading edge flap
- v) failure of thrust vectoring vane, stabilator and leading edge flap.

In each of these cases the following command scenarios were studied:

$$\mathbf{r}_1 = [0 \ 1 \ 0]^T \text{ vertical acceleration 1 deg in } \gamma$$

$$\mathbf{r}_2 = [0 \ 0 \ 1]^T \text{ pitch pointing 1 deg in } \theta$$

Since operating point 1 is unstable and requires more control action it will be selected to demonstrate our distribution redesign technique. Furthermore, since the LQG/LTR and H_∞ designs for this operating point were shown to be virtually identical, we arbitrarily selected the LQG/LTR design to illustrate our algorithm.

The resulting control action in the five cases (i) - (v) for the r_1 command are shown in figures 5.1, 5.2, 5.3, 5.4, 5.5. For the r_2 command the corresponding control action is shown in figures 5.6, 5.7, 5.8, 5.9, 5.10. The corresponding output responses for these reference commands are identical to those in figures 4.15, 4.16 and are therefore not presented.

As it can be noticed, the controls do not saturate either in magnitude or in rate. However, the figures also show that the controls which are operational exhibit larger peak values than when all controls were operational. This agrees with our physical intuition which tells us that when fewer controls are operational, then in order to maintain the same performance as in the unfailed case, these fewer controls should work harder.

The physics of the situation are as explained in chapter 4. The first command scenario requires extra lift which is produced by the trailing edge flap, aileron and throttle. The second is a much more effortless maneuver.

A point to make is that in cases (iv) and (v) there is not any freedom left for different assignment of the controls since the $\tilde{\mathbf{B}}_1$ matrix is invertible and therefore $\mathbf{T} = \tilde{\mathbf{B}}_1^{-1}$; i.e. the weighting \mathbf{W} does not play any role.

From the demonstration above the flexibility of the distribution redesign technique is apparent. Failures can be handled effectively by taking full advantage of the control redundancy without any need for compensator redesign.

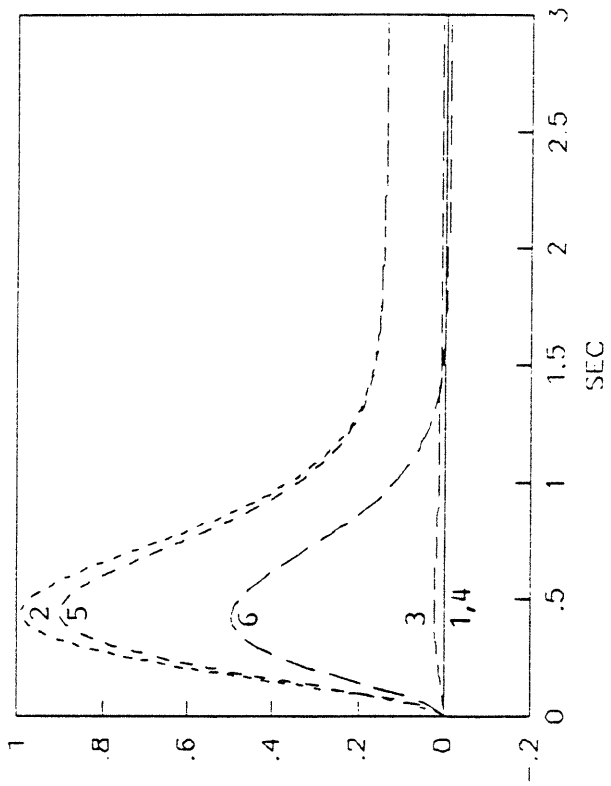


Figure 5.1 : Control response to r_1 in case (i)

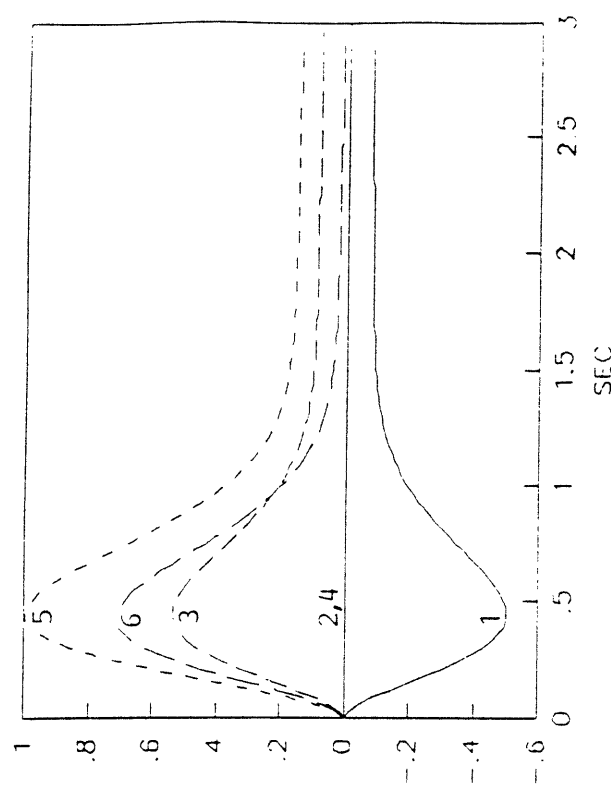


Figure 5.2 : Control response to r_1 in case (ii)

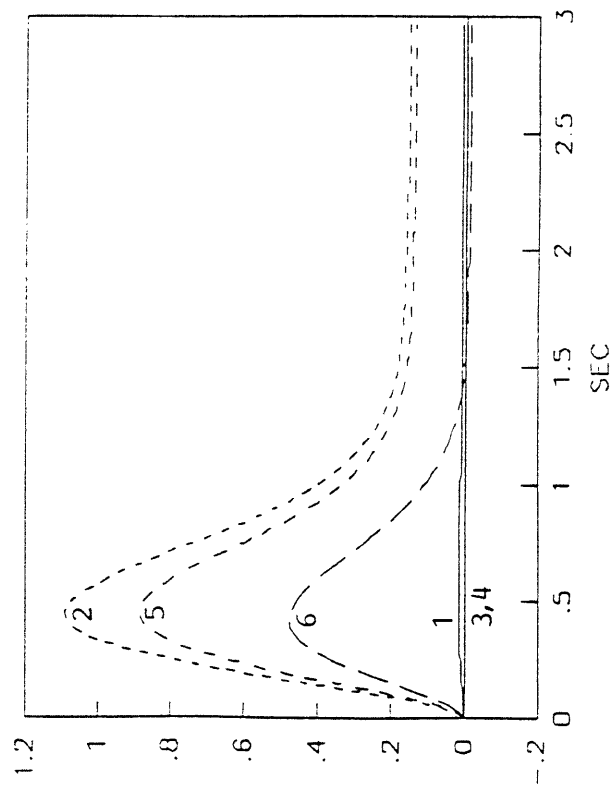


Figure 5.3 : Control response to r_1 in case (iii)

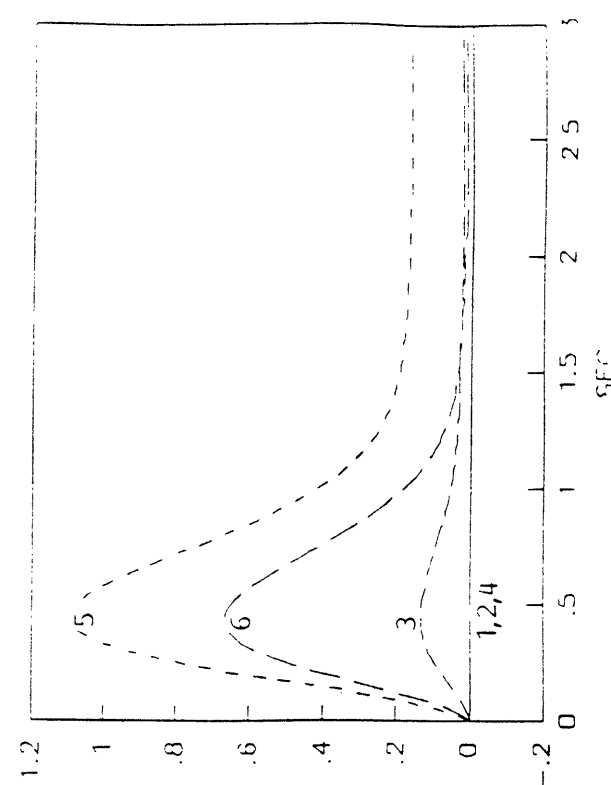


Figure 5.4 : Control response to r_1 in case (iv)

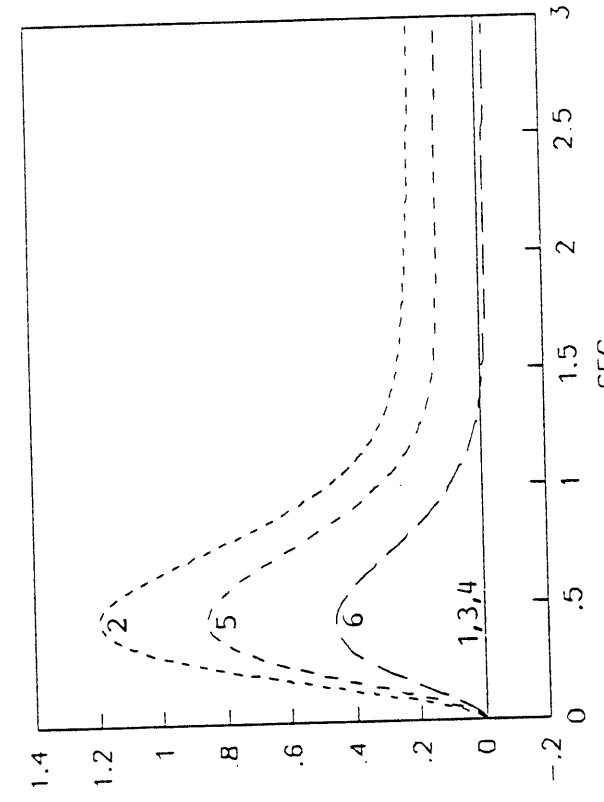


Figure 5.5 : Control response to r_1 in case (v)

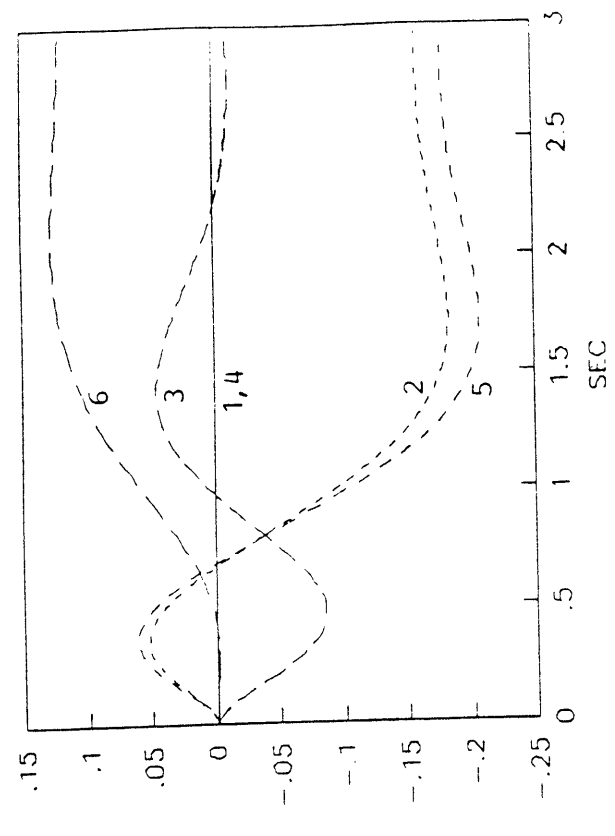


Figure 5.6 : Control response to r_2 in case (i)

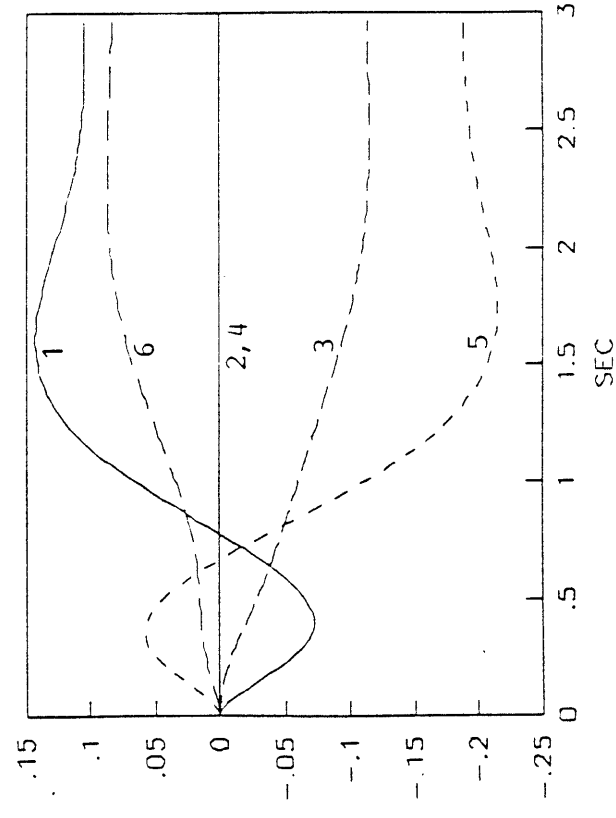


Figure 5.7 : Control response to r_2 in case (ii)

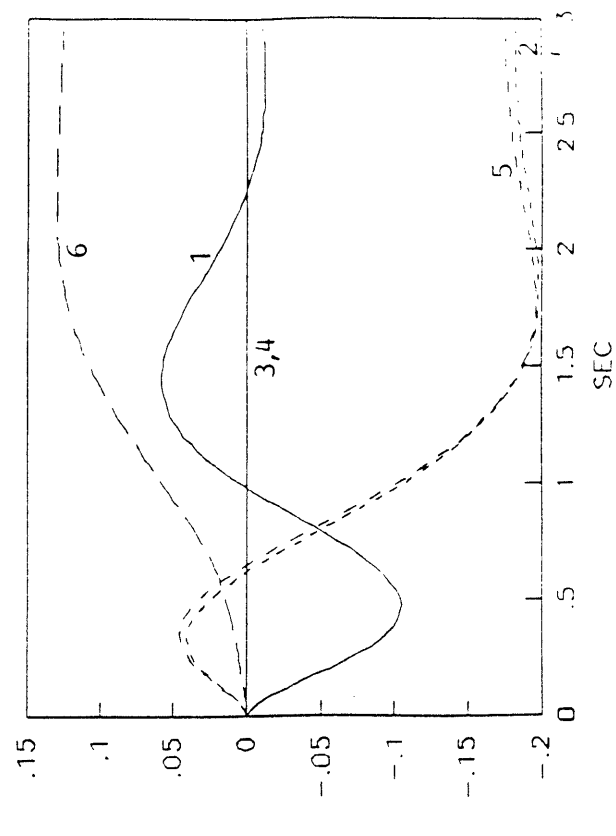


Figure 5.8 : Control response to r_2 in case (iii)

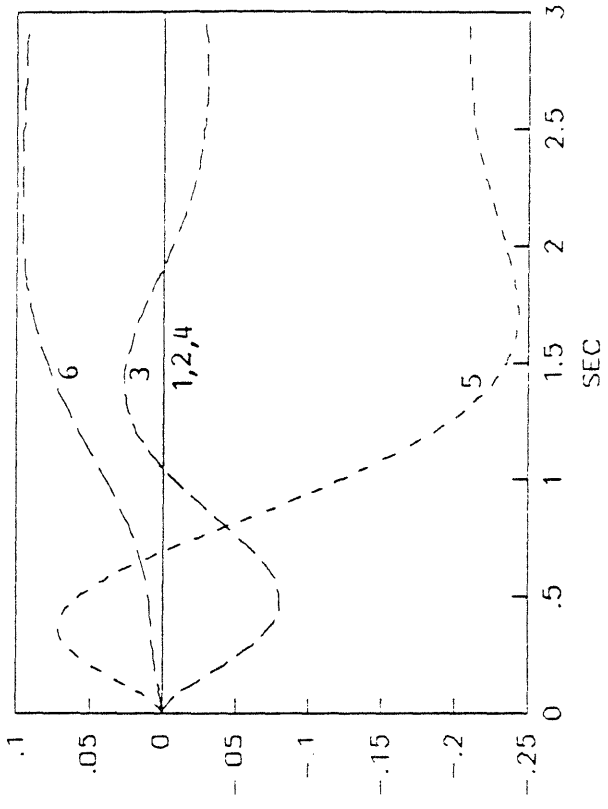


Figure 5.9 : Control response to r_2 in case (iv)

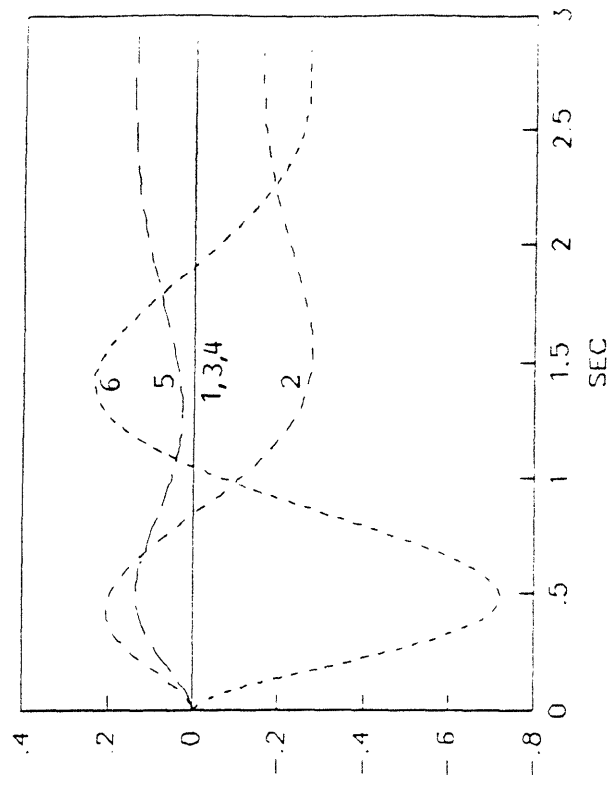


Figure 5.10 : Control response to r_2 in case (v)

5.4 Summary

In this chapter we presented a procedure for handling multiple actuator failures for the F18/HARV. The method presented does not require a compensator redesign. It simply requires the computation of a distribution matrix to generate new control signals from the (fixed) pseudocontrol signals. It was shown that this distribution matrix could be obtained by appropriately adjusting weights and solving a simple constrained quadratic optimization problem whose solution is known a priori.

Finally, by merely redesigning the distribution matrix, we not only guarantee nominal stability, and stability robustness, but performance remains unaltered; i.e. all properties of the pseudosystem are preserved.

CHAPTER 6

SUMMARY AND DIRECTIONS FOR FUTURE RESEARCH

6.1 Summary

In this thesis we presented high performance control system designs with prescribed robustness margins for the supermaneuverable F18/HARV. Designs were obtained at three selected operating conditions. Special emphasis was placed on a high angle of attack ($\alpha=25$ deg) flight condition where the aircraft is open loop unstable.

The technique of pseudocontrol formulation followed in this research offers a great amount of flexibility. This flexibility is especially useful in cases where certain controls cannot operate since it utilizes fully the control redundancy.

The LQG/LTR and H_∞ designs performed in this thesis are not very different. Both designs resulted in similar loop shapes and similar compensator strategies. In both designs also the same tradeoffs appear: magnitude saturation limits primarily constrain the bandwidth of the loop, whereas rate saturation limits constrain the stability margins of the system.

The H_∞ methodology however provides a somewhat more general framework since the need for measuring the outputs to be controlled does not exist.

6.2 Directions for Further Research

In this thesis only the longitudinal control problem was addressed. The next logical step for one to take is to look at the lateral control problem. This should be done with the intention of unifying the longitudinal and lateral design processes in an effort to obtain a complete (local) flight control system.

This, of course, should be done at several different flight conditions, after which a global controller can be obtained using gain scheduling ideas.

Another area which should be considered concerns the choice of distribution criteria, for generating controls from pseudocontrols, other than the quadratic criterion employed in chapter 3. For example, the criterion mentioned in chapter 3 of minimizing control magnitudes, rather than control energy, looks particularly attractive for many applications. A situation where one might employ such a distribution criterion is when saturating actuators are present.

Because control saturation is especially dangerous for flight conditions in which the F18/HARV is open loop unstable (finite downward gain margin), one should consider applying the recently developed methodology of Kanasouris [10]. In this work, the author presents a very practical and simple procedure for addressing this complex problem

Finally, since the H_∞ design methodology does not require that the quantities being controlled be measurable, it would be interesting for one to investigate how designs will change when quantities other than those which we wish to control are measured.

APPENDIX A1

Matching singular values at all frequencies when the plant is unstable

With the selection of the design parameter matrix L as described in Chapter 4 (eqns. 4.3.10, 4.3.11, 4.3.12) the shaping transfer function $C_a \Phi_a(s) L$ becomes an integrator

$$C_a \Phi_a(s) L = \frac{I}{s} \quad (A1.1)$$

The poles of $\Phi_a(s)$ consist of the plant and the integrator poles. Let us assume that $[A, C]$ is a detectable pair (i.e. the plant is detectable) then it immediately follows that $[A_a, C_a]$ is detectable. Equation (A1.1) implies that the plant poles are wiped out with this specific selection of L .

The only way that this can happen is by pole-zero cancellations. If the plant is unstable, then the unstable poles of the plant are cancelled, which implies that $[A_a, L]$ is not stabilizable since $[A_a, C_a]$ is by assumption detectable. Therefore, if one tries to solve the optimal filtering problem for the following system

$$\begin{aligned} \dot{x}_a &= A_a x_a + L \xi \\ y_a &= C_a x_a + \theta \end{aligned}$$

with ξ and θ Gaussian zero mean, uncorrelated, white noise with intensity equal to I and

$\mu I, \mu > 0$ respectively, then the optimal steady state gain H results in an unstable Kalman Filter loop [3]. In other words, among the symmetric and nonnegative solution Σ of the FARE (equation 4.3.6) the one that yields the optimal steady state solution to the filtering problem is such that

$$\operatorname{Re}[\lambda_i(A_a - H C_a)] < 0 \text{ for some } i$$

where

$$H = \frac{1}{\gamma} \Sigma C_a^T$$

Therefore, with the particular choice of L , if H is selected as the optimal filter gain, then the target feedback loop (TFL) is going to be unstable.

However, the following theorem given [11] allows us to view FARE as a pure mathematical equation which produces stabilizable solutions without any connection to the Kalman filter problem. In particular, the theorem guarantees that there is a unique stabilizing solution of FARE even if $[A, L]$ is not stabilizable.

Theorem:

Consider the Algebraic Riccati equation (ARE)

$$AX + XA^T - XWX + Q = 0$$

where

$$\mathbf{A}, \mathbf{W}, \mathbf{Q} \in \mathbb{R}^{n \times n}, \mathbf{W} = \mathbf{W}^T \geq \mathbf{0}, \mathbf{Q} = \mathbf{Q}^T \geq \mathbf{0}$$

with the associated Hamiltonian matrix

$$\mathbf{A}_H = \begin{bmatrix} \mathbf{A}^T & -\mathbf{W} \\ -\mathbf{Q} & -\mathbf{A} \end{bmatrix}$$

Also without loss of generality assume $\mathbf{W} = (1/\sqrt{\mu} \mathbf{C}^T) (1/\sqrt{\mu} \mathbf{C})$. Then the stabilizability of $[\mathbf{A}^T, 1/\sqrt{\mu} \mathbf{C}^T]$ and $\text{Re}[\lambda_i(\mathbf{A}_H)] \neq 0$ for every $i=1,2,\dots,2n$ is necessary as well as sufficient for the existence of a unique stabilizing solution \mathbf{X} of ARE. Also $\mathbf{X}^T = \mathbf{X} \geq \mathbf{0}$.

Stabilizing solution means that

$$\text{Re}[\lambda_i(\mathbf{A}^T - \mathbf{W}\mathbf{X})] < 0 \quad \forall i=1,\dots,n \quad \text{or}$$

$$\text{Re} \left[\lambda_i \left(\mathbf{A} - \frac{1}{\mu} \mathbf{X} \mathbf{C}^T \mathbf{C} \right) \right] < 0 \quad \forall i=1,\dots,n \quad \text{or}$$

$$\text{Re}[\lambda_i(\mathbf{A} - \mathbf{H} \mathbf{C})] < 0 \quad \forall i=1,\dots,n$$

with

$$\mathbf{H} = \frac{1}{\mu} \mathbf{X} \mathbf{C}^T$$

Clearly, $[\mathbf{A}^T, 1/\sqrt{\mu} \mathbf{C}^T]$ stabilizable implies $[\mathbf{A}, \mathbf{C}]$ detectable and vice versa.

Therefore, even if the plant is unstable, the specific \mathbf{L} that makes $\mathbf{C}_a \Phi_a(s) \mathbf{L} = \mathbf{I}/s$ can be used in the Riccati equation 4.3.6 (FARE) and yield a unique \mathbf{H} that makes the target feedback loop stable, provided that $[\mathbf{A}_a, \mathbf{C}_a]$ is detectable (or equivalently $[\mathbf{A}, \mathbf{C}]$ detectable) and $\text{Re}[\lambda_i(\mathbf{A}_a \mathbf{H})] \neq 0$ for every i where

$$\mathbf{A}_{aH} = \begin{bmatrix} \mathbf{A}_a^T & \frac{1}{\mu} \mathbf{C}_a^T \mathbf{C}_a \\ -\mathbf{L} \mathbf{L}^T & -\mathbf{A}_a^T \end{bmatrix}$$

Clearly, the Kalman Frequency Domain Equality holds since the solution \mathbf{X} satisfies the Riccati equation. Therefore, for sufficiently small values of μ the target loop singular values will be matched at all frequencies. Furthermore, all the guarantees for the stability margins of the Kalman filter loop hold. This is because all that is required [5] for these guarantees to hold is a stabilizing solution to FARE.

A final point to make, is that when (\mathbf{A}, \mathbf{L}) is stabilizable then the unique stabilizing solution \mathbf{X} of the previous theorem is identical with the solution Σ to the optimal steady state filtering problem (i.e. the gain $\mathbf{H} = 1/\mu \Sigma \mathbf{C}^T$ stabilizes the target feedback loop in addition to solving the optimal filtering problem).

APPENDIX A2

I) Linearized Model for Longitudinal Dynamics of the F18/HARV

The unscaled linearized models for longitudinal dynamics for the three selected conditions are given in the sequel.

$$\dot{\mathbf{x}}(t) = \mathbf{A}\mathbf{x}(t) + \mathbf{B}\mathbf{u}(t) \quad \mathbf{A} \in \mathbb{R}^{4 \times 4} \quad \mathbf{B} \in \mathbb{R}^{4 \times 6}$$

$$\mathbf{x}(t) = [V_T \text{ (ft/sec)} \quad \alpha \text{ (rad)} \quad q \text{ (rad/sec)} \quad \theta \text{ (rad)}]^T$$

$$\mathbf{u}(t) = [\delta_{TVS} \text{ (deg)} \quad \delta_{AS} \text{ (deg)} \quad \delta_{SS} \text{ (deg)} \quad \delta_{LES} \text{ (deg)} \quad \delta_{TES} \text{ (deg)} \quad \delta_T \text{ (deg)}]^T$$

Operating point 1

$$\mathbf{A} = \begin{bmatrix} -0.0750 & -24.0500 & 0. & -32.1600 \\ -0.0009 & -0.1959 & 0.9896 & 0. \\ -0.0002 & -0.1454 & -0.1877 & 0. \\ 0. & 0. & 1.0000 & 0. \end{bmatrix}$$

$$\mathbf{B} = \begin{bmatrix} -0.0230 & 0. & -0.0729 & 0.0393 & -0.0411 & 0.1600 \\ -0.0002 & -0.0001 & -0.0004 & -0.0000 & -0.0003 & -0.0003 \\ -0.0067 & -0.0007 & -0.0120 & -0.0006 & 0.0007 & 0.0005 \\ 0. & 0. & 0. & 0. & 0. & 0. \end{bmatrix}$$

Operating point 2

A=	-0.0143	-9.4396	0.0060	-32.1635
	-0.0003	-0.6745	0.9879	0.
	-0.0004	-1.8497	-0.4115	0.
	0.	0.	1.0000	0.

B=	-0.0016	0.0003	-0.0520	0.0326	-0.0587	0.2515
	-0.0000	-0.0006	-0.0011	0.0001	-0.0012	-0.0000
	-0.0018	-0.0091	-0.0548	-0.0058	0.0053	0.0008
	0.	0.	0.	0.	0.	0.

Operating point 3

A=	-0.0116	4.6005	0.0988	-32.1635
	-0.0002	-0.9309	0.9870	0.
	-0.0002	-5.2838	-0.5634	0.
	0.	0.	1.0000	0.

B=	-0.0015	0.0054	-0.0504	0.0090	-0.0523	0.2406
	-0.0000	-0.0007	-0.0014	-0.0002	-0.0016	-0.0000
	-0.0023	-0.0157	-0.0927	-0.0097	0.0096	0.0008
	0.	0.	0.	0.	0.	0.

II) Model of the Scaled System and Pseudosystem

Scaled system state space description:

$$\dot{\mathbf{x}}(t) = \mathbf{A}\mathbf{x}(t) + \mathbf{B}\mathbf{u}(t)$$

$$\mathbf{y}(t) = \mathbf{C}\mathbf{x}(t)$$

Pseudosystem state space description:

$$\dot{\mathbf{x}}(t) = \mathbf{A}\mathbf{x}(t) + \mathbf{B}_v\mathbf{v}(t)$$

$$\mathbf{y}(t) = \mathbf{C}\mathbf{x}(t)$$

The matrix \mathbf{B}_v is given by:

$$\mathbf{B}_v = \begin{bmatrix} 1.0000 & 0. & 0. \\ 0. & 1.0000 & 0. \\ 0. & 0. & 1.0000 \\ 0. & 0. & 0. \end{bmatrix}$$

Operating point 1

$$\mathbf{A} = \begin{bmatrix} -0.0750 & -0.1399 & 0. & -0.1871 \\ -0.1517 & -0.1959 & 0.9896 & 0. \\ -0.0258 & -0.1454 & -0.1877 & 0. \\ 0. & 0. & 1.0000 & 0. \end{bmatrix}$$

$$\mathbf{B} = \begin{bmatrix} -0.3830 & 0. & -0.8258 & 0.0262 & -0.4114 & 1.4400 \\ -0.5157 & -0.3724 & -0.8377 & -0.0054 & -0.5157 & -0.4641 \\ -19.1941 & -2.0054 & -23.3767 & -0.0653 & 1.2032 & 0.7271 \\ 0. & 0. & 0. & 0. & 0. & 0. \end{bmatrix}$$

C= 0.3750 0. 0. 0.
0. -1.0000 0. 1.0000
0. 0. 0. 1.0000

Operating point 2

A= -0.0143 -0.0549 0.0000 -0.1871
-0.0516 -0.6745 0.9879 0.
-0.0602 -1.8497 -0.4115 0.
0. 0. 1.0000 0.

B= -0.0269 0.0043 -0.3813 0.2173 -0.5870 1.3413
-0.0859 -1.6788 -1.4458 0.1490 -1.9853 -0.0367
-5.1566 -25.9550 -69.0758 -6.6429 3.1272 0.6967
0. 0. 0. 0. 0. 0.

C= 0.1000 0. 0. 0.
0. -1.0000 0. 1.0000
0. 0. 0. 1.0000

Operating point 3

A= -0.0116 0.0268 0.0006 -0.1871
-0.0309 -0.9309 0.9870 0.
-0.0292 -5.2838 -0.5634 0.
0. 0. 1.0000 0.

B= -0.0242 0.0905 -0.3528 0.0421 -0.4182 1.7646
-0.0859 -2.0340 -1.7326 -0.1845 -2.2277 -0.0252
-6.6177 -45.0918 -111.5618 -7.7808 13.2009 0.9706
0. 0. 0. 0. 0. 0.

C= 0.1500 0. 0. 0.
0. -1.0000 0. 1.0000
0. 0. 0. 1.0000

III) LQG/LTR Compensator Gains for the Model of the Scaled System

The compensator $K_O(s)$ for the scaled system is given by:

$$K_O(s) = TK_v(s) \quad \text{with}$$

$K_v(s)$ compensator for the pseudosystem

$$T = W^{-1} B_1^T (B_1 W^{-1} B_1^T)^{-1} \quad \text{distribution matrix from pseudo-to-actual controls}$$

W weighting on the actual controls

Operating point 1

$$W = \text{diag}(1, 1, 1, 1, 5.2, 1)$$

$$T = \begin{bmatrix} 0.1477 & 0.2895 & -0.0345 \\ -0.1088 & -0.6165 & 0.0207 \\ -0.1144 & -0.2502 & -0.0140 \\ 0.0140 & 0.0060 & -0.0007 \\ -0.1926 & -0.5239 & 0.0230 \\ 0.5578 & -0.3659 & -0.0041 \end{bmatrix}$$

$$G = \begin{bmatrix} 4.7980 & -0.1453 & -0.0464 & 11.5219 & -0.6691 & -0.3413 & -0.8354 \\ -0.1453 & 7.7613 & -0.0741 & -1.1518 & 30.1319 & -0.4708 & -31.9103 \\ -0.0464 & -0.0741 & 6.1099 & -0.1537 & -0.5510 & 18.6694 & 31.3135 \end{bmatrix}$$

H=

0.6749	-0.3907	0.9437
1.2022	-0.6827	0.5013
0.2101	-0.4111	0.4582
8.0250	0.0097	-0.0125
-0.0083	-3.0028	3.0045
-0.0119	0.0903	0.1020
-0.0047	0.0291	3.0337

Operating point 2

W=

1.	0.	0.	0.	0.	0.
0.	1.	0.	0.	0.	0.
0.	0.	1.	0.	0.	0.
0.	0.	0.	1.	0.	0.
0.	0.	0.	0.	3.	0.
0.	0.	0.	0.	0.	1.

T=

-0.0047	0.0149	-0.0013
0.1190	-0.3743	0.0040
-0.0562	0.0964	-0.0146
0.1073	0.0967	-0.0041
-0.0640	-0.2490	0.0070
0.6837	-0.0957	-0.0005

G=

4.4586	-0.0472	-0.0619	9.9425	-0.1565	-0.3026	-0.8514
-0.0472	13.5219	-0.5220	-0.6600	91.5581	-3.6110	-107.3047
-0.0619	-0.5220	8.5886	-0.4810	-7.9276	37.0203	92.1192

H=

0.3104	0.1071	0.6414
0.8251	-3.7238	3.7238
0.7792	-21.1352	21.1352
26.6667	0.0000	-0.0000
-0.0000	-4.0000	4.0000
-0.0000	-0.0000	-0.0000
-0.0000	-0.0000	4.0000

Operating point 3

W=

1.	0.	0.	0.	0.	0.
0.	1.	0.	0.	0.	0.
0.	0.	1.	0.	0.	0.
0.	0.	0.	1.	0.	0.
0.	0.	0.	0.	3.	0.
0.	0.	0.	0.	0.	1.

T=

-0.0027	0.0110	-0.0007
0.0641	-0.3294	0.0030
-0.0276	0.1059	-0.0096
0.0189	-0.0105	-0.0004
-0.0447	-0.2298	0.0048
0.5468	-0.0160	-0.0009

G=

6.5020	-0.0185	-0.0273	21.1388	0.0365
-0.0185	16.1209	-1.2157	-0.4208	130.6805
-0.0273	-1.2157	9.0358	-0.2075	-22.0121

H=

0.4998	-0.1922	0.8471
1.8048	-2.3607	2.3608
2.1056	-6.4738	6.4738
35.0000	-0.0000	-0.0000
-0.0000	-3.5000	3.5000
-0.0000	0.0000	-0.0000
-0.0000	0.0000	3.5000

REFERENCES

- [1] M. Athans, "6.233-6.234 Class Notes", M.I.T., Fall 1987-Spring 1988, Cambridge, MA.
 - [2] G. Stein and M. Athans, "the LQG/LTR Procedure for Multivariable Feedback Control Design", IEEE Transactions on Automatic Control, Vol. AC-32, No. 2, February 1987, pp. 105-114.
 - [3] H. Kwakernaak and Sivan, *Linear Optimal Control Systems*, New York, Wiley-Interscience, 1972.
 - [4] B.A. Francis, *A Course in H_∞ Control Theory*, Lecture Notes in Control and Information Sciences, Springer-Verlag, Berlin, 1987.
 - [5] N.A. Lehtomaki, N.R. Sandell, and M. Athans, "Robustness Results in LQG/LTR Based Multivariable Control Designs", IEEE Trans. on Auto. Control, Vol.AC-26, No.1, pp.75-93, February 1981.
 - [6] N.A.Lehtomaki, Practical Robustness Measures in Multivariable Control System Analysis, Ph.D. Thesis, MIT LIDS-TH-1093, May 1981.
 - [7] J.C. Doyle, and G. Stein, "Multivariable Feedback Design: Concepts for a Classical/Modern Synthesis", IEEE Trans on Auto. Control, Vol. AC-26, No. 1, pp.4-15, February 1981
 - [8] M.G. Safonov, and M. Athans, "Gain and Phase Margin for Multi-Loop LQG Regulators", IEEE Trans. on Auto. Control", Vol AC-22, No. 2, pp.173-179, 1977.
 - [9] J.S. Freudenberg and D.P. Looze, "Relations Between Properties of Multivariable Feedback Systems at Different Loop-Breaking Points: Part 1", 1985 CDC. ": Part 2", 1986 ACC.
-

- [10] P. Kapsouris, Design for Performance Enhancement in Feedback Control Systems with Multiple Saturating Nonlinearities, Ph.D. Thesis, MIT LIDS-TH-1757, March 1988.

- [11] J.C. Doyle, Lectures Notes, 1984 ONR/Honeywell Workshop on Advances in Multivariable Control, Minn. MN, Oct. 1984

- [12] G. Stein, "Latest H_∞ Results", unpublished note, Oct. 1987.

- [13] B. Etkin, "*Dynamics of Flight - Stability and Control*", New York, Wiley, 1982

- [14] P. Kapsouris, Gain Scheduled Multivariable Control for the GE-21 Turbofan Engine Using the LQR and LQG/LTR Methodologies, M.S. Thesis, MIT, May 1984.

- [15] A.A. Rodriguez and M. Athans, "Multivariable Control of a Twin Lift Helicopter System Using the LQG/LTR Design Methodology", Proceedings of the American Control Conference, Seattle, WA, 1986, pp. 1325-1332

- [16] J.M. Abercrombie, F/A-18 Flying Qualities Development, Technical report, McDonnell Aircraft Company MCAIR NO 84-009.

- [17] F.J. Lallman, Preliminary Design Study of a Lateral-Directional Control System Using Thrust Vectoring, NASA Technical Memorandum 86425

- [18] P. Merkel and R. Whitmoger, "Development and Evaluation of Precision Control

**Modes for Fighter Aircraft", AIAA Guidance and Control Conference, San Diego,
CA, 1976.**
